Journal of Computational Physics 518 (2024) 113311

Contents lists available at ScienceDirect

Journal of Computational Physics

journal homepage: www.elsevier.com/locate/jcp

Low-dissipation central-upwind schemes for compressible multifluids

Shaoshuai Chu [a,b], Alexander Kurganov [c], Ruixiao Xin [d,*]

[a] Department of Mathematics, RWTH Aachen University, 52056 Aachen, Germany
[b] Department of Mathematics and Shenzhen International Center for Mathematics, Southern University of Science and Technology, Shenzhen, 518055, China
[c] Department of Mathematics, Shenzhen International Center for Mathematics, and Guangdong Provincial Key Laboratory of Computational Science and Material Design, Southern University of Science and Technology, Shenzhen, 518055, China
[d] Department of Mathematics, Southern University of Science and Technology, Shenzhen, 518055, China

ARTICLE INFO

MSC:
76M12
65M08
76M20
65M20
76N30

Keywords:
Low-dissipation central-upwind schemes
Path-conservative central-upwind schemes
Flux globalization
Affine-invariant WENO-Z interpolation
Compressible multifluids

ABSTRACT

We introduce second-order low-dissipation (LD) path-conservative central-upwind (PCCU) schemes for the one- (1-D) and two-dimensional (2-D) multifluid systems, whose components are assumed to be immiscible and separated by material interfaces. The proposed LD PCCU schemes are derived within the flux globalization based PCCU framework and they employ the LD central-upwind (LDCU) numerical fluxes. These fluxes have been proposed in [A. Kurganov and R. Xin, J. Sci. Comput., 96 (2023), Paper No. 56] for the single-fluid compressible Euler equations, recently modified in [S. Chu, A. Kurganov, and R. Xin, submitted], and in this paper, we rigorously develop their multifluid extensions. In order to achieve higher resolution near the material interfaces, we track their locations and use an overcompressive SBM limiter in their neighborhoods, while utilizing a dissipative generalized minmod limiter in the rest of the computational domain. We first develop a second-order finite-volume LD PCCU scheme and then extend it to the fifth order of accuracy via the finite-difference alternative weighted essentially non-oscillatory (A-WENO) framework. We apply the developed schemes to a number of 1-D and 2-D numerical examples to demonstrate the performance of the new schemes.

1. Introduction

In this paper, we focus on the development of highly accurate and conservative finite-volume methods for compressible multifluids, which are assumed to be immiscible. The studied two-dimensional (2-D) multifluid system reads as

$$\begin{aligned}
&\rho_t + (\rho u)_x + (\rho v)_y = 0,\\
&(\rho u)_t + (\rho u^2 + p)_x + (\rho uv)_y = 0,\\
&(\rho v)_t + (\rho uv)_x + (\rho v^2 + p)_y = 0,\\
&E_t + [u(E+p)]_x + [v(E+p)]_y = 0.
\end{aligned} \tag{1.1}$$

* Corresponding author.
E-mail addresses: chuss2019@mail.sustech.edu.cn (S. Chu), alexander@sustech.edu.cn (A. Kurganov), 12331009@mail.sustech.edu.cn (R. Xin).

https://doi.org/10.1016/j.jcp.2024.113311
Received 29 July 2023; Received in revised form 19 July 2024; Accepted 24 July 2024

Available online 31 July 2024

Here, x and y are spatial variables, t is the time, ρ is the density, u and v are the x- and y-velocities, p is the pressure, and E is the total energy. The system (1.1) is closed through the following equation of state (EOS) for each of the fluid components:

$$p=(\gamma-1)\left[E-\frac{\rho}{2}(u^2+v^2)\right]-\gamma\pi_\infty, \tag{1.2}$$

where the parameters γ and π_∞ represent the specific heat ratio and stiffness parameter, respectively. When $\pi_\infty\equiv 0$, the system (1.1)–(1.2) reduces to the ideal gas multicomponent case.

The fluid components can be identified by the variable ϕ, such as the specific heat ratio γ (or a certain function of γ), the mass fraction of the fluid component in the fluid mixture, or a level-set function designed to track the interfaces between the fluid components; see, e.g., [2,3,10,18,36,39,44,54,55] and references therein. The state variable ϕ propagates with the fluid velocity and thus satisfies the following advection equation:

$$\phi_t+u\phi_x+v\phi_y=0. \tag{1.3}$$

The system (1.1)–(1.3) is a nonlinear hyperbolic system of PDEs and thus its solutions may develop complicated wave structures including shocks, rarefactions, and contact discontinuities. In the single-fluid regime, that is, when $\gamma\equiv\text{Const}$ and $\pi_\infty\equiv\text{Const}$, the system (1.1)–(1.3) reduces to the Euler equations of gas dynamics, which can be numerically solved by finite-volume (FV) methods; see, e.g., the monographs [23,33,48] and references therein. However, a straightforward application of single-fluid FV methods to the multifluid system (1.1)–(1.3) may generate spurious pressure and velocity oscillations, which typically originate near the material interface and then spread all over the computational domain; see, e.g., the review paper [2] and references therein.

In recent years, a variety of FV methods capable of capturing material interfaces in a non-oscillatory manner have been proposed. A fully conservative approach was first developed in [45], where the pressure and velocity remained constant across the material interface. This approach is robust but may suffer obvious drawbacks when strong shocks pass through the fluid interface. The quasi-conservative approach was first introduced in [1], where pressure and velocity non-disturbing condition at an isolated material interface was introduced to analyze and derive the spatial discretization. The resulting schemes reduced the numerical oscillations effectively with the help of a quasi-conservative discretization. There are also many locally nonconservative approaches designed to prevent pressure/velocity oscillations by sacrificing the conservation property near material interfaces. The conservation errors in these approaches are typically small and decay after the mesh is refined. The pressure-based hybrid algorithms [9,27] are obtained by switching from the conservative energy equation to the nonconservative pressure one near the interfaces. The ghost-cell methods based on the single-fluid interpolations leading to two different single-fluid numerical fluxes at the material interfaces (placed at the cell interfaces at each time step) were introduced in [3,18]. The interface tracking method [10] is based on the interpolation between the single-fluid data from both sides of the interface and ignoring the "mixed" cell data. We note that both the ghost fluid and interface tracking approaches are very robust in the 1-D case, but their multidimensional extensions are rather cumbersome. For several high-order WENO schemes for compressible multifluids, we refer the reader to [16,22,25,41,42].

In this paper, our objective is to develop highly accurate and non-oscillatory numerical schemes for the so-called γ-based multifluid systems studied in [8,46], which in the 2-D case read as (1.1)–(1.2) together with the equations (1.3) for the state variables $\Gamma:=1/(\gamma-1)$ and $\Pi:=\gamma\pi_\infty/(\gamma-1)$, which we recast as follows:

$$\Gamma_t+(u\Gamma)_x+(v\Gamma)_y=\Gamma(u_x+v_y),\quad \Pi_t+(u\Pi)_x+(v\Pi)_y=\Pi(u_x+v_y). \tag{1.4}$$

The resulting system is nonconservative (in fact, it can be rewritten in the conservative form, but as it was shown in [46], a non-conservative form is preferable for designing an accurate numerical method) and the nonconservative terms on the right-hand side require a special treatment.

We numerically solve the system (1.1)–(1.2), (1.4) and its one-dimensional (1-D) version by the Riemann-problem-solver-free central-upwind (CU) schemes, which were originally introduced in [28,30,31] for general multidimensional hyperbolic systems of conservative laws, and then extended to nonconservative hyperbolic systems in [6], where path-conservative CU (PCCU) schemes were introduced. The PCCU schemes were extended to the flux globalization framework allowing to treat a wider variety of nonconservative systems in [4,5,7,29].

The aforementioned PCCU schemes are based on the CU numerical fluxes from [28,30], which have relatively large numerical dissipation preventing high resolution of contact waves/material interfaces. In the recent work [32], we have introduced a new way of reducing the numerical dissipation present in the CU schemes and introduced the low-dissipation CU (LDCU) schemes. In these schemes, the dissipation is reduced at the projection step, performed after the numerical solution is evolved to the new time level. The novel projection is based on a subcell resolution technique, which introduces several degrees of freedom that can be utilized to better approximate contact waves and material interfaces. In [32], we have designed the LDCU schemes for both the 1-D and 2-D single-fluid compressible Euler equations, which have then been recently improved in [14]. In this paper, we extend the LDCU schemes to the γ-based multifluid models. The extension is carried out in the flux globalization PCCU framework and results in new flux globalization based LD PCCU schemes.

We also extend the proposed LD PCCU schemes to the fifth order of accuracy using the framework of the finite-difference alternative WENO (A-WENO) schemes developed in [13,24,37,38,51–53]. Our new fifth-order schemes are based on the LD PCCU numerical fluxes, a new, more efficient way to approximate the high-order A-WENO correction terms (see [15]), and the recently proposed fifth-order affine-invariant WENO-Z (Ai-WENO-Z) interpolation [17,34,50] applied to the local characteristic variables with the help of the local characteristic decomposition (LCD).

This paper is organized as follows. §2 is devoted to the 1-D LD PCCU scheme. In §2.1, we give an overview of the flux globalization based PCCU schemes and develop such scheme for the γ-based multifluid model. The LD PCCU scheme is derived in §2.2, where we prove that the new scheme preserves constant velocity and pressure across isolated material interfaces (this ensures lack of pressure/velocity-based oscillations). In §2.3, the second-order LD PCCU scheme is extended to the fifth-order flux globalization based LD Ai-WENO PCCU scheme. In §3, we present the 2-D extensions of the new LD PCCU schemes. In §4, we test the proposed LD PCCU schemes together with their fifth-order versions on a number of 1-D and 2-D numerical examples. Finally, in §5, we give some concluding remarks and comments.

2. One-dimensional algorithms

In this section, we present the new 1-D flux globalization based LD PCCU schemes for the 1-D compressible multifluids.

2.1. Flux globalization based path-conservative central-upwind schemes

We begin with a brief overview of the flux globalization based PCCU scheme, which was introduced in [29] for the general nonconservative system

$$\boldsymbol{U}_t + \boldsymbol{F}(\boldsymbol{U})_x = B(\boldsymbol{U})\boldsymbol{U}_x,$$

which can be rewritten in the following quasi-conservative form:

$$\boldsymbol{U}_t + \boldsymbol{K}(\boldsymbol{U})_x = 0, \quad \boldsymbol{K}(\boldsymbol{U}) = \boldsymbol{F}(\boldsymbol{U}) - \boldsymbol{R}(\boldsymbol{U}), \tag{2.1}$$

where $\boldsymbol{U}(\boldsymbol{x},t) \in \mathbb{R}^d$ is the vector of unknowns, $\boldsymbol{F} : \mathbb{R}^d \to \mathbb{R}^d$ is a flux, $B \in \mathbb{R}^{d\times d}$,

$$\boldsymbol{R}(\boldsymbol{U}) := \int_{\hat{x}}^{x} B(\boldsymbol{U})\boldsymbol{U}_\xi(\xi,t)\,\mathrm{d}\xi,$$

and $\hat{x}$ is an arbitrary number.

We first introduce a uniform mesh consisting of the finite-volume cells $C_j := [x_{j-\frac{1}{2}}, x_{j+\frac{1}{2}}]$ of size $x_{j+\frac{1}{2}} - x_{j-\frac{1}{2}} \equiv \Delta x$ centered at $x_j = (x_{j-\frac{1}{2}} + x_{j+\frac{1}{2}})/2$, $j = 1,\ldots,N$ and set $\hat{x} = x_{\frac{1}{2}}$. We assume that at a certain level t, an approximate solution, realized in terms of the cell averages

$$\overline{\boldsymbol{U}}_j(t) :\approx \frac{1}{\Delta x}\int_{C_j} \boldsymbol{U}(x,t)\,\mathrm{d}x,$$

is available. The cell averages $\overline{\boldsymbol{U}}_j$ are then evolved in time by solving the following system of ODEs (see [29]):

$$\frac{\mathrm{d}}{\mathrm{d}t}\overline{\boldsymbol{U}}_j = -\frac{\boldsymbol{\mathcal{K}}_{j+\frac{1}{2}} - \boldsymbol{\mathcal{K}}_{j-\frac{1}{2}}}{\Delta x}, \tag{2.2}$$

where $\boldsymbol{\mathcal{K}}_{j+\frac{1}{2}}$ are the CU numerical fluxes

$$\boldsymbol{\mathcal{K}}_{j+\frac{1}{2}} = \frac{a^+_{j+\frac{1}{2}}\boldsymbol{K}^-_{j+\frac{1}{2}} - a^-_{j+\frac{1}{2}}\boldsymbol{K}^+_{j+\frac{1}{2}}}{a^+_{j+\frac{1}{2}} - a^-_{j+\frac{1}{2}}} + \frac{a^+_{j+\frac{1}{2}}a^-_{j+\frac{1}{2}}}{a^+_{j+\frac{1}{2}} - a^-_{j+\frac{1}{2}}}\left(\boldsymbol{U}^+_{j+\frac{1}{2}} - \boldsymbol{U}^-_{j+\frac{1}{2}}\right). \tag{2.3}$$

Notice that all of the indexed quantities in (2.2) and (2.3) as well as other indexed quantities introduced below depend on t, but from now on we will omit this dependence for the sake of brevity. In (2.3), $\boldsymbol{U}^\pm_{j+\frac{1}{2}}$ are the left/right-sided point values of $\boldsymbol{U}$ at the cell interfaces $x_{j+\frac{1}{2}}$, which are computed using a piecewise linear reconstruction, which will be discussed in §2.1.1, and $a^\pm_{j+\frac{1}{2}}$ are the one-sided local speeds of propagation, which can be estimated using the largest and smallest eigenvalues of the matrix $\frac{\partial \boldsymbol{F}}{\partial \boldsymbol{U}}(\boldsymbol{U}) - B(\boldsymbol{U})$. The global fluxes $\boldsymbol{K}^\pm_{j+\frac{1}{2}}$ are obtained using the relation in (2.1), namely, by

$$\boldsymbol{K}^\pm_{j+\frac{1}{2}} = \boldsymbol{F}^\pm_{j+\frac{1}{2}} - \boldsymbol{R}^\pm_{j+\frac{1}{2}}, \tag{2.4}$$

where $\boldsymbol{F}^\pm_{j+\frac{1}{2}} := \boldsymbol{F}(\boldsymbol{U}^\pm_{j+\frac{1}{2}})$ and the point values of the global variable $\boldsymbol{R}$ are computed as follows. First, we set $\boldsymbol{R}^-_{\frac{1}{2}} := \boldsymbol{0}$ and then evaluate

$$\boldsymbol{R}^+_{\frac{1}{2}} = \boldsymbol{B}_{\boldsymbol{\Psi},\frac{1}{2}}, \tag{2.5}$$

and recursively

$$\boldsymbol{R}^-_{j+\frac{1}{2}} = \boldsymbol{R}^+_{j-\frac{1}{2}} + \boldsymbol{B}_j, \quad \boldsymbol{R}^+_{j+\frac{1}{2}} = \boldsymbol{R}^-_{j+\frac{1}{2}} + \boldsymbol{B}_{\boldsymbol{\Psi},j+\frac{1}{2}}, \quad j = 1,\dots,N. \tag{2.6}$$

In (2.5) and (2.6), $\boldsymbol{B}_j$ and $\boldsymbol{B}_{\boldsymbol{\Psi},j+\frac{1}{2}}$ are obtained using a proper quadrature for the integrals in

$$\boldsymbol{B}_j \approx \int\limits_{C_j} B(\boldsymbol{U})\boldsymbol{U}_x\,\mathrm{d}x \quad \text{and} \quad \boldsymbol{B}_{\boldsymbol{\Psi},j+\frac{1}{2}} = \int\limits_0^1 B\big(\boldsymbol{\Psi}_{j+\frac{1}{2}}(s)\big)\boldsymbol{\Psi}'_{j+\frac{1}{2}}(s)\,\mathrm{d}s, \tag{2.7}$$

where, $\boldsymbol{\Psi}_{j+\frac{1}{2}}(s) := \boldsymbol{\Psi}\big(s;\boldsymbol{U}^-_{j+\frac{1}{2}},\boldsymbol{U}^+_{j+\frac{1}{2}}\big)$ is a sufficiently smooth path connecting the states $\boldsymbol{U}^-_{j+\frac{1}{2}}$ and $\boldsymbol{U}^+_{j+\frac{1}{2}}$, that is,

$$\boldsymbol{\Psi}:[0,1]\times\mathbb{R}^d\times\mathbb{R}^d\to\mathbb{R}^d, \quad \boldsymbol{\Psi}(0;\boldsymbol{U}^-_{j+\frac{1}{2}},\boldsymbol{U}^+_{j+\frac{1}{2}}) = \boldsymbol{U}^-_{j+\frac{1}{2}}, \quad \boldsymbol{\Psi}(1;\boldsymbol{U}^-_{j+\frac{1}{2}},\boldsymbol{U}^+_{j+\frac{1}{2}}) = \boldsymbol{U}^+_{j+\frac{1}{2}}.$$

2.1.1. Application to the compressible multifluid system

We apply the flux globalization based PCCU scheme to the 1-D γ-based multifluid system

$$\begin{aligned}
&\rho_t + (\rho u)_x = 0,\\
&(\rho u)_t + (\rho u^2 + p)_x = 0,\\
&E_t + [u(E+p)]_x = 0,\\
&\Gamma_t + (u\Gamma)_x = \Gamma u_x,\\
&\Pi_t + (u\Pi)_x = \Pi u_x,
\end{aligned} \tag{2.8}$$

completed with the following EOS:

$$p = (\gamma-1)\left[E - \frac{\rho}{2}u^2\right] - \gamma\pi_\infty. \tag{2.9}$$

The system (2.8) can be rewritten in the equivalent quasi-conservative form (2.1) with

$$\begin{aligned}
&\boldsymbol{U} := (\rho,\rho u,E,\Gamma,\Pi)^\top, \quad \boldsymbol{F}(\boldsymbol{U}) = (\rho u,\rho u^2+p,u(E+p),u\Gamma,u\Pi)^\top,\\
&\text{and} \quad \boldsymbol{R}(\boldsymbol{U}) = \left(0,0,0,\int\limits_{\hat{x}}^x \Gamma u_\xi\,\mathrm{d}\xi,\int\limits_{\hat{x}}^x \Pi u_\xi\,\mathrm{d}\xi\right)^\top.
\end{aligned} \tag{2.10}$$

We first discuss the reconstruction procedure for recovering the point values $\boldsymbol{U}^\pm_{j+\frac{1}{2}}$ out of the cell averages $\overline{\boldsymbol{U}}_j$. Since the variables u and p are continuous across material interfaces (contact waves), we reconstruct the primitive variables $\boldsymbol{V} := (\rho,u,p,\Gamma,\Pi)^\top$ instead of the conservative ones. To this end, we compute the cell centered values of u and p,

$$u_j = \frac{(\overline{\rho u})_j}{\overline{\rho}_j}, \quad p_j = \frac{1}{\overline{\Gamma}_j}\left[\overline{E}_j - \frac{((\overline{\rho u})_j)^2}{2\overline{\rho}_j} - \overline{\Pi}_j\right], \tag{2.11}$$

and then construct the linear pieces

$$\widetilde{\boldsymbol{V}}_j(x) = \boldsymbol{V}_j + (\boldsymbol{V}_x)_j(x-x_j), \quad x\in C_j, \tag{2.12}$$

where $\boldsymbol{V}_j := (\overline{\rho}_j,u_j,p_j,\overline{\Gamma}_j,\overline{\Pi}_j)^\top$ and the slopes $(\boldsymbol{V}_x)_j$ are supposed to be computed with the help of a nonlinear limiter to ensure a non-oscillatory nature of (2.12). In the numerical experiments reported in §4, we implement a simple adaptive limiting strategy and use different limiters near and away from the material interfaces. Our goal is to achieve very sharp resolution of linearly degenerate waves at material interfaces. To this end, we need to detect the location of the interfaces. In the two-fluid case, this can be done as follows. We first introduce $\widehat{\Gamma} := (\Gamma_{\mathrm{I}}+\Gamma_{\mathrm{II}})/2$, where Γ_{I} and Γ_{II} are the values of Γ for the first and second fluid, respectively. We then assume that the interface is located either in cell C_j or C_{j+1} if

$$(\overline{\Gamma}_j - \widehat{\Gamma})(\overline{\Gamma}_{j+1} - \widehat{\Gamma}) < 0. \tag{2.13}$$

In these two cells as well as in the neighboring cells C_{j-1} and C_{j+2}, we use the overcompressive SBM limiter [35]:

$$(\boldsymbol{V}_x)_j = \begin{cases} \phi^{\mathrm{SBM}}_{\theta,\tau}\left(\dfrac{\overline{\boldsymbol{V}}_{j+1}-\overline{\boldsymbol{V}}_j}{\overline{\boldsymbol{V}}_j-\overline{\boldsymbol{V}}_{j-1}}\right)\dfrac{\overline{\boldsymbol{V}}_j-\overline{\boldsymbol{V}}_{j-1}}{\Delta x}, & \text{if } |\overline{\boldsymbol{V}}_j-\overline{\boldsymbol{V}}_{j-1}|>\varepsilon_1,\\ 0, & \text{otherwise,}\end{cases} \tag{2.14}$$

where ε_1 is a small positive constant and in all of the numerical examples reported in §4, we have taken $\varepsilon_1 = 10^{-12}$. Here, the two-parameter function

$$\phi^{\rm SBM}_{\theta,\tau}(r) := \begin{cases} 0 & \text{if } r \le 0, \\ \min\{r\theta, 1+\tau(r-1)\} & \text{if } 0 < r \le 1, \\ r\phi^{\rm SBM}_{\theta,\tau}\left(\frac{1}{r}\right) & \text{otherwise}, \end{cases} \tag{2.15}$$

is applied in a componentwise manner with $\tau = -0.5$, which belongs to the overcompressive range of values of τ; see [35]. Away from the material interfaces, using the same overcompressive limiter is dangerous as it may lead to an artificial sharpening of smooth parts of the computed solution (see [35]) and thus we use a dissipative generalized minmod limiter, given by the same formulae (2.14)–(2.15), but with $\tau = 0.5$, there. In both areas, we use $\theta = 1.3$.

Remark 2.1. Notice that the generalized minmod limiter can be written in a simpler form [35,40,47] by

$$(\boldsymbol{V}_x)_j = \text{minmod}\left(\theta\,\frac{\overline{\boldsymbol{V}}_{j+1}-\overline{\boldsymbol{V}}_j}{\Delta x}, \frac{\overline{\boldsymbol{V}}_{j+1}-\overline{\boldsymbol{V}}_{j-1}}{2\Delta x}, \theta\,\frac{\overline{\boldsymbol{V}}_j-\overline{\boldsymbol{U}}_{j-1}}{\Delta x}\right),$$

with the minmod function defined by

$$\text{minmod}(c_1,c_2,\ldots) = \begin{cases} \min(c_1,c_2,\ldots) & \text{if } c_i>0,\ \forall i, \\ \max(c_1,c_2,\ldots) & \text{if } c_i<0,\ \forall i, \\ 0 & \text{otherwise.} \end{cases}$$

Remark 2.2. If the number of fluid components is more than two, detecting interface cells becomes a more complicated task. A reasonable extension of the strategy used in (2.13) should be developed for the problem at hand.

Equipped with $(\boldsymbol{V}_x)_j$, we then use (2.12) to obtain

$$\boldsymbol{V}^-_{j+\frac12} = \lim_{\substack{x\to x^-\\ j+\frac12}} \widetilde{\boldsymbol{V}}(x) = \overline{\boldsymbol{V}}_j + \frac{\Delta x}{2}(\boldsymbol{V}_x)_j, \quad \boldsymbol{V}^+_{j+\frac12} = \lim_{\substack{x\to x^+\\ j+\frac12}} \widetilde{\boldsymbol{V}}(x) = \overline{\boldsymbol{V}}_{j+1} - \frac{\Delta x}{2}(\boldsymbol{V}_x)_{j+1}, \tag{2.16}$$

and the corresponding point values of the conservative variables $\boldsymbol{U}$:

$$\boldsymbol{U}^\pm_{j+\frac12} = \left(\rho^\pm_{j+\frac12}, \rho^\pm_{j+\frac12}u^\pm_{j+\frac12}, E^\pm_{j+\frac12}, \Gamma^\pm_{j+\frac12}, \Pi^\pm_{j+\frac12}\right)^\top, \quad E^\pm_{j+\frac12} = \Gamma^\pm_{j+\frac12}p^\pm_{j+\frac12} + \frac{\rho^\pm_{j+\frac12}}{2}\left(u^\pm_{j+\frac12}\right)^2 + \Pi^\pm_{j+\frac12}. \tag{2.17}$$

We then compute the point values $\boldsymbol{K}^\pm_{j+\frac12}$ following (2.4)–(2.6). First, we use (2.10) and (2.17) to obtain

$$\boldsymbol{F}^\pm_{j+\frac12} = \left(\rho^\pm_{j+\frac12}u^\pm_{j+\frac12}, \rho^\pm_{j+\frac12}\left(u^\pm_{j+\frac12}\right)^2 + p^\pm_{j+\frac12}, u^\pm_{j+\frac12}\left(E^\pm_{j+\frac12}+p^\pm_{j+\frac12}\right), \Gamma^\pm_{j+\frac12}u^\pm_{j+\frac12}, \Pi^\pm_{j+\frac12}u^\pm_{j+\frac12}\right)^\top, \tag{2.18}$$

and then evaluate $\boldsymbol{B}_j$ in (2.7) by substituting there the piecewise linear reconstructions (2.12) of u, Γ, and Π, which results in

$$\boldsymbol{B}_j = \left(0,0,0, \frac{\Gamma^-_{j+\frac12}+\Gamma^+_{j-\frac12}}{2}\left(u^-_{j+\frac12}-u^+_{j-\frac12}\right), \frac{\Pi^-_{j+\frac12}+\Pi^+_{j-\frac12}}{2}\left(u^-_{j+\frac12}-u^+_{j-\frac12}\right)\right)^\top. \tag{2.19}$$

Next, in order to obtain $\boldsymbol{B}_{\boldsymbol{\Psi},j+\frac12}$ in (2.7), a proper path connecting the states $(u^-_{j+\frac12}, \Gamma^-_{j+\frac12}, \Pi^-_{j+\frac12})$ and $(u^+_{j+\frac12}, \Gamma^+_{j+\frac12}, \Pi^+_{j+\frac12})$ needs to be used, for instance, a simple linear path:

$$\begin{aligned} &\boldsymbol{\Psi}^u_{j+\frac12}(s) = u^-_{j+\frac12} + s\left(u^+_{j+\frac12}-u^-_{j+\frac12}\right), \quad \boldsymbol{\Psi}^\Gamma_{j+\frac12}(s) = \Gamma^-_{j+\frac12} + s\left(\Gamma^+_{j+\frac12}-\Gamma^-_{j+\frac12}\right), \\ &\boldsymbol{\Psi}^\Pi_{j+\frac12}(s) = \Pi^-_{j+\frac12} + s\left(\Pi^+_{j+\frac12}-\Pi^-_{j+\frac12}\right). \end{aligned} \tag{2.20}$$

Substituting (2.20) into (2.7) then results in

$$\boldsymbol{B}_{\boldsymbol{\Psi},j+\frac12} = \left(0,0,0, \frac{\Gamma^+_{j+\frac12}+\Gamma^-_{j+\frac12}}{2}\left(u^+_{j+\frac12}-u^-_{j+\frac12}\right), \frac{\Pi^+_{j+\frac12}+\Pi^-_{j+\frac12}}{2}\left(u^+_{j+\frac12}-u^-_{j+\frac12}\right)\right)^\top. \tag{2.21}$$

Finally, the one-sided local-speeds of propagation $a^{\pm}_{j+\frac{1}{2}}$ can be estimated by

$$a^{+}_{j+\frac{1}{2}}=\max\left\{u^{-}_{j+\frac{1}{2}}+c^{-}_{j+\frac{1}{2}},u^{+}_{j+\frac{1}{2}}+c^{+}_{j+\frac{1}{2}},0\right\},\quad a^{-}_{j+\frac{1}{2}}=\min\left\{u^{-}_{j+\frac{1}{2}}-c^{-}_{j+\frac{1}{2}},u^{+}_{j+\frac{1}{2}}-c^{+}_{j+\frac{1}{2}},0\right\},$$

where $c:=\sqrt{[(1+\Gamma)p+\Pi]/(\Gamma\rho)}$.

Remark 2.3. The numerical fluxes (2.3) are slightly different from those present in [29] as one of the goals in [29] was to make the resulting scheme well-balanced and thus different values of $\boldsymbol{U}^{\pm}_{j+\frac{1}{2}}$ were used in (2.3) and in the computation of $\boldsymbol{K}^{\pm}_{j+\frac{1}{2}}$.

2.2. Flux globalization based low-dissipation PCCU schemes

In this section, we derived a modified, LD version of the flux globalization based PCCU scheme presented in §2.1. We follow the idea used in [14,32], where the LDCU scheme for the single-fluid compressible Euler equations has been introduced. In order to extend the LDCU scheme to the multifluid case, we now go through all of the derivation steps and begin with the development of the fully discrete LD PCCU scheme.

2.2.1. Fully discrete scheme

We assume that the computed cell averages $\overline{\boldsymbol{U}}^{n}_{j}:\approx\frac{1}{\Delta x}\int_{C_j}\boldsymbol{U}(x,t^n)\,\mathrm{d}x$ are available at a certain time level $t=t^n$ and use them to reconstruct a second-order piecewise linear interpolant consisting of the linear pieces $\overline{\boldsymbol{U}}^{n}_{j}+(\boldsymbol{U}_x)^{n}_{j}(x-x_j)$, $x\in C_j$, where the slopes $(\boldsymbol{U}_x)^{n}_{j}$ are obtained using a certain nonlinear limiter. We then estimate the local speeds of propagation $a^{\pm}_{j+\frac{1}{2}}$, introduce the corresponding points $x^{n}_{j+\frac{1}{2},\ell}:=x_{j+\frac{1}{2}}+a^{-}_{j+\frac{1}{2}}\Delta t^n$ and $x^{n}_{j+\frac{1}{2},r}:=x_{j+\frac{1}{2}}+a^{+}_{j+\frac{1}{2}}\Delta t^n$, and integrate the system (2.1) over the space-time control volumes, which consist of the "smooth", $[x_{j-\frac{1}{2},r},x_{j+\frac{1}{2},\ell}]\times[t^n,t^{n+1}]$, and "nonsmooth", $[x_{j+\frac{1}{2},\ell},x_{j+\frac{1}{2},r}]\times[t^n,t^{n+1}]$, ones, where $t^{n+1}:=t^n+\Delta t^n$. This way the solution is evolved in time and upon the completion of the evolution step, we obtain the intermediate cell averages

$$\begin{aligned}\overline{\boldsymbol{U}}^{\,\mathrm{int}}_{j+\frac{1}{2}}=\frac{1}{a^{+}_{j+\frac{1}{2}}-a^{-}_{j+\frac{1}{2}}}\Big\{&\boldsymbol{U}^{n}_{j+\frac{1}{2},r}a^{+}_{j+\frac{1}{2}}-\frac{(\boldsymbol{U}_x)^{n}_{j+1}}{2}\big(a^{+}_{j+\frac{1}{2}}\big)^2\Delta t^n-\boldsymbol{U}^{n}_{j+\frac{1}{2},\ell}a^{-}_{j+\frac{1}{2}}+\frac{(\boldsymbol{U}_x)^{n}_{j}}{2}\big(a^{-}_{j+\frac{1}{2}}\big)^2\Delta t^n\\&-\left[\boldsymbol{K}\big(\boldsymbol{U}^{n+\frac{1}{2}}_{j+\frac{1}{2},r}\big)-\boldsymbol{K}\big(\boldsymbol{U}^{n+\frac{1}{2}}_{j+\frac{1}{2},\ell}\big)\right]\Big\},\end{aligned}\tag{2.22}$$

and

$$\begin{aligned}\overline{\boldsymbol{U}}^{\,\mathrm{int}}_{j}=&\overline{\boldsymbol{U}}^{n}_{j}+\frac{(\boldsymbol{U}_x)^{n}_{j}}{2}\big(a^{+}_{j-\frac{1}{2}}+a^{-}_{j+\frac{1}{2}}\big)\Delta t^n\\&-\frac{\Delta t^n}{\Delta x-\big(a^{+}_{j-\frac{1}{2}}-a^{-}_{j+\frac{1}{2}}\big)\Delta t^n}\left[\boldsymbol{K}\big(\boldsymbol{U}^{n+\frac{1}{2}}_{j+\frac{1}{2},\ell}\big)-\boldsymbol{K}\big(\boldsymbol{U}^{n+\frac{1}{2}}_{j-\frac{1}{2},r}\big)\right];\end{aligned}\tag{2.23}$$

see [32] for details. In (2.22)–(2.23), the point values of $\boldsymbol{U}$ at $\big(x^{n}_{j+\frac{1}{2},\ell},t^n\big)$ and $\big(x^{n}_{j+\frac{1}{2},r},t^n\big)$ are computed using the piecewise linear reconstruction of $\boldsymbol{U}$, namely,

$$\begin{aligned}\boldsymbol{U}^{n}_{j+\frac{1}{2},\ell}&:=\widetilde{\boldsymbol{U}}(x^{n}_{j+\frac{1}{2},\ell},t^n)=\overline{\boldsymbol{U}}^{n}_{j}+(\boldsymbol{U}_x)^{n}_{j}\Big(\frac{\Delta x}{2}+a^{-}_{j+\frac{1}{2}}\Delta t^n\Big),\\\boldsymbol{U}^{n}_{j+\frac{1}{2},r}&:=\widetilde{\boldsymbol{U}}(x^{n}_{j+\frac{1}{2},r},t^n)=\overline{\boldsymbol{U}}^{n}_{j+1}-(\boldsymbol{U}_x)^{n}_{j+1}\Big(\frac{\Delta x}{2}-a^{+}_{j+\frac{1}{2}}\Delta t^n\Big),\end{aligned}$$

and the point values of $\boldsymbol{U}$ at $\big(x^{n}_{j+\frac{1}{2},\ell},t^{n+\frac{1}{2}}\big)$ and $\big(x^{n}_{j+\frac{1}{2},r},t^{n+\frac{1}{2}}\big)$, are obtained using the Taylor expansions about $\big(x_{j+\frac{1}{2},r},t^n\big)$ and $\big(x_{j+\frac{1}{2},\ell},t^n\big)$, respectively, and the fact that $\boldsymbol{U}_t=-\boldsymbol{K}(\boldsymbol{U})_x$:

$$\boldsymbol{U}^{n+\frac{1}{2}}_{j+\frac{1}{2},\ell}=\boldsymbol{U}^{n}_{j+\frac{1}{2},\ell}-\frac{\Delta t^n}{2}\boldsymbol{K}\big(\boldsymbol{U}^{n}_{j+\frac{1}{2},\ell}\big)_x,\quad\boldsymbol{U}^{n+\frac{1}{2}}_{j+\frac{1}{2},r}=\boldsymbol{U}^{n}_{j+\frac{1}{2},r}-\frac{\Delta t^n}{2}\boldsymbol{K}\big(\boldsymbol{U}^{n}_{j+\frac{1}{2},r}\big)_x.\tag{2.24}$$

Here, the slopes $\boldsymbol{K}\big(\boldsymbol{U}^{n}_{j+\frac{1}{2},\ell}\big)_x$ and $\boldsymbol{K}\big(\boldsymbol{U}^{n}_{j+\frac{1}{2},r}\big)_x$ can be computed with the help of a certain nonlinear limiter; see [28] for details.

Next, the intermediate solution, realized in terms of $\{\overline{\boldsymbol{U}}^{\,\mathrm{int}}_{j}\}$ and $\{\overline{\boldsymbol{U}}^{\,\mathrm{int}}_{j+\frac{1}{2}}\}$, is projected onto the original grid. To this end, we need to construct the interpolant

$$\widetilde{\boldsymbol{U}}^{\,\mathrm{int}}(x)=\sum_j\left\{\widetilde{\boldsymbol{U}}^{\,\mathrm{int}}_{j+\frac12}(x)\mathcal{X}_{[x_{j+\frac12,\ell},x_{j+\frac12,r}]}+\overline{\boldsymbol{U}}^{\,\mathrm{int}}_j\mathcal{X}_{[x_{j-\frac12,r},x_{j+\frac12,\ell}]}\right\},\tag{2.25}$$

where $\mathcal{X}$ denotes the characteristic function of the corresponding intervals. We follow [14] and set

$$\widetilde{\boldsymbol{U}}^{\,\mathrm{int}}_{j+\frac12}(x)=\begin{cases}\overline{\boldsymbol{U}}^{\,\mathrm{int,L}}_{j+\frac12}, & x<\widetilde{x}_{j+\frac12},\\ \overline{\boldsymbol{U}}^{\,\mathrm{int,R}}_{j+\frac12}, & x>\widetilde{x}_{j+\frac12},\end{cases}\tag{2.26}$$

where $\widetilde{x}_{j+\frac12}=x_{j+\frac12}+u^{\mathrm{int}}_{j+\frac12}\Delta t^n$ and $u^{\mathrm{int}}_{j+\frac12}:=(\overline{\rho u})^{\mathrm{int}}_{j+\frac12}/\overline{\rho}^{\,\mathrm{int}}_{j+\frac12}$. The values $\overline{\boldsymbol{U}}^{\,\mathrm{int,L}}_{j+\frac12}$ and $\overline{\boldsymbol{U}}^{\,\mathrm{int,R}}_{j+\frac12}$ are determined in several steps. First, according to the local conservation requirement, the conditions

$$a^{\mathrm{int},+}_{j+\frac12}\overline{\boldsymbol{U}}^{\,\mathrm{int,R}}_{j+\frac12}-a^{\mathrm{int},-}_{j+\frac12}\overline{\boldsymbol{U}}^{\,\mathrm{int,L}}_{j+\frac12}=(a^+_{j+\frac12}-a^-_{j+\frac12})\overline{\boldsymbol{U}}^{\,\mathrm{int}}_{j+\frac12},\tag{2.27}$$

where $a^{\mathrm{int},\pm}_{j+\frac12}:=a^{\pm}_{j+\frac12}-u^{\mathrm{int}}_{j+\frac12}$, have to be satisfied, and the rest of the relations on $\overline{\boldsymbol{U}}^{\,\mathrm{int,L}}_{j+\frac12}$ and $\overline{\boldsymbol{U}}^{\,\mathrm{int,R}}_{j+\frac12}$ are to be established for the problem at hand. In fact, the conservation of Γ and Π components of $\boldsymbol{U}$ is not physically essential, but the relation (2.27) for Γ and Π are crucial for proving physically relevant properties of the resulting flux globalization based LD PCCU scheme; see §2.2.3.

For the γ-based multifluid model (2.8)–(2.9), we follow the single-fluid approach from [14,32] and make the projection step sharp and accurate for the contact waves, which are linearly degenerate and thus affected by the excessive numerical dissipation much more than nonlinear shock waves. In order to design such projection step, we consider an isolated contact wave consisting of the jump discontinuities in ρ, Γ, and Π propagating in the region with constant u and p, and make both u and p to be constant across the cell interface, namely, we set

$$\begin{aligned}&\frac{(\overline{\rho u})^{\mathrm{int,L}}_{j+\frac12}}{\overline{\rho}^{\,\mathrm{int,L}}_{j+\frac12}}=\frac{(\overline{\rho u})^{\mathrm{int,R}}_{j+\frac12}}{\overline{\rho}^{\,\mathrm{int,R}}_{j+\frac12}},\\ &\frac{1}{\overline{\Gamma}^{\mathrm{int,L}}_{j+\frac12}}\left(\overline{E}^{\mathrm{int,L}}_{j+\frac12}-\frac{\big((\overline{\rho u})^{\mathrm{int,L}}_{j+\frac12}\big)^2}{2\overline{\rho}^{\,\mathrm{int,L}}_{j+\frac12}}-\overline{\Pi}^{\mathrm{int,L}}_{j+\frac12}\right)=\frac{1}{\overline{\Gamma}^{\mathrm{int,R}}_{j+\frac12}}\left(\overline{E}^{\mathrm{int,R}}_{j+\frac12}-\frac{\big((\overline{\rho u})^{\mathrm{int,R}}_{j+\frac12}\big)^2}{2\overline{\rho}^{\,\mathrm{int,R}}_{j+\frac12}}-\overline{\Pi}^{\mathrm{int,R}}_{j+\frac12}\right),\end{aligned}\tag{2.28}$$

where we have used the EOS (2.9). Next, we solve (2.27) and (2.28) for $(\overline{\rho u})^{\mathrm{int,L}}_{j+\frac12}$, $(\overline{\rho u})^{\mathrm{int,R}}_{j+\frac12}$, $\overline{E}^{\mathrm{int,L}}_{j+\frac12}$, and $\overline{E}^{\mathrm{int,R}}_{j+\frac12}$, and express these quantities in terms of $\overline{\rho}^{\,\mathrm{int,L}}_{j+\frac12}$, $\overline{\rho}^{\,\mathrm{int,R}}_{j+\frac12}$, $\overline{\Gamma}^{\mathrm{int,L}}_{j+\frac12}$, $\overline{\Gamma}^{\mathrm{int,R}}_{j+\frac12}$, $\overline{\Pi}^{\mathrm{int,L}}_{j+\frac12}$, and $\overline{\Pi}^{\mathrm{int,R}}_{j+\frac12}$:

$$\begin{aligned}(\overline{\rho u})^{\mathrm{int,L}}_{j+\frac12}&=\overline{\rho}^{\,\mathrm{int,L}}_{j+\frac12}u^{\mathrm{int}}_{j+\frac12},\quad \overline{E}^{\mathrm{int,L}}_{j+\frac12}=\frac{\overline{\Gamma}^{\mathrm{int,L}}_{j+\frac12}}{\overline{\Gamma}^{\mathrm{int}}_{j+\frac12}}\overline{E}^{\mathrm{int}}_{j+\frac12}\\ &+\frac{a^{\mathrm{int},+}_{j+\frac12}\big(\overline{\Gamma}^{\mathrm{int,R}}_{j+\frac12}\overline{\rho}^{\,\mathrm{int,L}}_{j+\frac12}-\overline{\Gamma}^{\mathrm{int,L}}_{j+\frac12}\overline{\rho}^{\,\mathrm{int,R}}_{j+\frac12}\big)}{2\big(a^+_{j+\frac12}-a^-_{j+\frac12}\big)\overline{\Gamma}^{\mathrm{int}}_{j+\frac12}}\big(u^{\mathrm{int}}_{j+\frac12}\big)^2+\frac{a^{\mathrm{int},+}_{j+\frac12}\big(\overline{\Gamma}^{\mathrm{int,R}}_{j+\frac12}\overline{\Pi}^{\mathrm{int,L}}_{j+\frac12}-\overline{\Gamma}^{\mathrm{int,L}}_{j+\frac12}\overline{\Pi}^{\mathrm{int,R}}_{j+\frac12}\big)}{\big(a^+_{j+\frac12}-a^-_{j+\frac12}\big)\overline{\Gamma}^{\mathrm{int}}_{j+\frac12}},\end{aligned}\tag{2.29}$$

$$\begin{aligned}(\overline{\rho u})^{\mathrm{int,R}}_{j+\frac12}&=\overline{\rho}^{\,\mathrm{int,R}}_{j+\frac12}u^{\mathrm{int}}_{j+\frac12},\quad \overline{E}^{\mathrm{int,R}}_{j+\frac12}=\frac{\overline{\Gamma}^{\mathrm{int,R}}_{j+\frac12}}{\overline{\Gamma}^{\mathrm{int}}_{j+\frac12}}\overline{E}^{\mathrm{int}}_{j+\frac12}\\ &+\frac{a^{\mathrm{int},-}_{j+\frac12}\big(\overline{\Gamma}^{\mathrm{int,R}}_{j+\frac12}\overline{\rho}^{\,\mathrm{int,L}}_{j+\frac12}-\overline{\Gamma}^{\mathrm{int,L}}_{j+\frac12}\overline{\rho}^{\,\mathrm{int,R}}_{j+\frac12}\big)}{2\big(a^+_{j+\frac12}-a^-_{j+\frac12}\big)\overline{\Gamma}^{\mathrm{int}}_{j+\frac12}}\big(u^{\mathrm{int}}_{j+\frac12}\big)^2+\frac{a^{\mathrm{int},-}_{j+\frac12}\big(\overline{\Gamma}^{\mathrm{int,R}}_{j+\frac12}\overline{\Pi}^{\mathrm{int,L}}_{j+\frac12}-\overline{\Gamma}^{\mathrm{int,L}}_{j+\frac12}\overline{\Pi}^{\mathrm{int,R}}_{j+\frac12}\big)}{\big(a^+_{j+\frac12}-a^-_{j+\frac12}\big)\overline{\Gamma}^{\mathrm{int}}_{j+\frac12}}.\end{aligned}\tag{2.30}$$

Notice that after enforcing (2.27) and (2.28), we are left with three degrees of freedom, which we use to make the profiles of ρ, Γ, and Π across the cell interface as sharp as possible and, at the same time, non-oscillatory. This is achieved in the same way as in [14,32], namely, by setting

$$\begin{aligned}
&\overline{\rho}^{\,\mathrm{int,L}}_{j+\frac12}=\overline{\rho}^{\,\mathrm{int}}_{j+\frac12}+\frac{\delta^{\rho}_{j+\frac12}}{a^{\mathrm{int},-}_{j+\frac12}},\quad \overline{\Gamma}^{\mathrm{int,L}}_{j+\frac12}=\overline{\Gamma}^{\mathrm{int}}_{j+\frac12}+\frac{\delta^{\Gamma}_{j+\frac12}}{a^{\mathrm{int},-}_{j+\frac12}},\quad \overline{\Pi}^{\mathrm{int,L}}_{j+\frac12}=\overline{\Pi}^{\mathrm{int}}_{j+\frac12}+\frac{\delta^{\Pi}_{j+\frac12}}{a^{\mathrm{int},-}_{j+\frac12}},\\
&\overline{\rho}^{\,\mathrm{int,R}}_{j+\frac12}=\overline{\rho}^{\,\mathrm{int}}_{j+\frac12}+\frac{\delta^{\rho}_{j+\frac12}}{a^{\mathrm{int},+}_{j+\frac12}},\quad \overline{\Gamma}^{\mathrm{int,R}}_{j+\frac12}=\overline{\Gamma}^{\mathrm{int}}_{j+\frac12}+\frac{\delta^{\Gamma}_{j+\frac12}}{a^{\mathrm{int},+}_{j+\frac12}},\quad \overline{\Pi}^{\mathrm{int,R}}_{j+\frac12}=\overline{\Pi}^{\mathrm{int}}_{j+\frac12}+\frac{\delta^{\Pi}_{j+\frac12}}{a^{\mathrm{int},+}_{j+\frac12}},
\end{aligned}\tag{2.31}$$

where

$$\begin{aligned}
\delta^{\rho}_{j+\frac12}&=\mathrm{minmod}\left(-a^{\mathrm{int},-}_{j+\frac12}\big(\overline{\rho}^{\,\mathrm{int}}_{j+\frac12}-\rho^{\mathrm{int}}_{j+\frac12,\ell}\big),a^{\mathrm{int},+}_{j+\frac12}\big(\rho^{\mathrm{int}}_{j+\frac12,r}-\overline{\rho}^{\,\mathrm{int}}_{j+\frac12}\big)\right),\\
\delta^{\Gamma}_{j+\frac12}&=\mathrm{minmod}\left(-a^{\mathrm{int},-}_{j+\frac12}\big(\overline{\Gamma}^{\mathrm{int}}_{j+\frac12}-\Gamma^{\mathrm{int}}_{j+\frac12,\ell}\big),a^{\mathrm{int},+}_{j+\frac12}\big(\Gamma^{\mathrm{int}}_{j+\frac12,r}-\overline{\Gamma}^{\mathrm{int}}_{j+\frac12}\big)\right),\\
\delta^{\Pi}_{j+\frac12}&=\mathrm{minmod}\left(-a^{\mathrm{int},-}_{j+\frac12}\big(\overline{\Pi}^{\mathrm{int}}_{j+\frac12}-\Pi^{\mathrm{int}}_{j+\frac12,\ell}\big),a^{\mathrm{int},+}_{j+\frac12}\big(\Pi^{\mathrm{int}}_{j+\frac12,r}-\overline{\Pi}^{\mathrm{int}}_{j+\frac12}\big)\right),
\end{aligned}\tag{2.32}$$

and $\boldsymbol{U}^{\,\mathrm{int}}_{j+\frac12,\ell}\approx\boldsymbol{U}(x_{j+\frac12,\ell},t^{n+1})$ and $\boldsymbol{U}^{\,\mathrm{int}}_{j+\frac12,r}\approx\boldsymbol{U}(x_{j+\frac12,r},t^{n+1})$ are evaluated similarly to (2.24):

$$\boldsymbol{U}^{\,\mathrm{int}}_{j+\frac12,\ell}=\boldsymbol{U}^{n}_{j+\frac12,\ell}-\Delta t^n\boldsymbol{K}\big(\boldsymbol{U}^{n}_{j+\frac12,\ell}\big)_x,\quad \boldsymbol{U}^{\,\mathrm{int}}_{j+\frac12,r}=\boldsymbol{U}^{n}_{j+\frac12,r}-\Delta t^n\boldsymbol{K}\big(\boldsymbol{U}^{n}_{j+\frac12,r}\big)_x.\tag{2.33}$$

We then complete the construction of $\overline{\boldsymbol{U}}^{\,\mathrm{int,L}}_{j+\frac12}$ and $\overline{\boldsymbol{U}}^{\,\mathrm{int,R}}_{j+\frac12}$ by substituting (2.31) into (2.29)–(2.30), which results in

$$\begin{aligned}
(\overline{\rho u})^{\mathrm{int,L}}_{j+\frac12}&=(\overline{\rho u})^{\mathrm{int}}_{j+\frac12}+\frac{\delta^{\rho}_{j+\frac12}}{a^{\mathrm{int},-}_{j+\frac12}}u^{\mathrm{int}}_{j+\frac12},\quad (\overline{\rho u})^{\mathrm{int,R}}_{j+\frac12}=(\overline{\rho u})^{\mathrm{int}}_{j+\frac12}+\frac{\delta^{\rho}_{j+\frac12}}{a^{\mathrm{int},+}_{j+\frac12}}u^{\mathrm{int}}_{j+\frac12},\\
\overline{E}^{\,\mathrm{int,L}}_{j+\frac12}&=\left(1+\frac{\delta^{\Gamma}_{j+\frac12}}{a^{\mathrm{int},-}_{j+\frac12}\overline{\Gamma}^{\mathrm{int}}_{j+\frac12}}\right)\overline{E}^{\mathrm{int}}_{j+\frac12}+\frac{\delta^{\rho}_{j+\frac12}\overline{\Gamma}^{\mathrm{int}}_{j+\frac12}-\delta^{\Gamma}_{j+\frac12}\overline{\rho}^{\mathrm{int}}_{j+\frac12}}{2a^{\mathrm{int},-}_{j+\frac12}\overline{\Gamma}^{\mathrm{int}}_{j+\frac12}}\big(u^{\mathrm{int}}_{j+\frac12}\big)^2+\frac{\delta^{\Pi}_{j+\frac12}\overline{\Gamma}^{\mathrm{int}}_{j+\frac12}-\delta^{\Gamma}_{j+\frac12}\overline{\Pi}^{\mathrm{int}}_{j+\frac12}}{a^{\mathrm{int},-}_{j+\frac12}\overline{\Gamma}^{\mathrm{int}}_{j+\frac12}},\\
\overline{E}^{\,\mathrm{int,R}}_{j+\frac12}&=\left(1+\frac{\delta^{\Gamma}_{j+\frac12}}{a^{\mathrm{int},+}_{j+\frac12}\overline{\Gamma}^{\mathrm{int}}_{j+\frac12}}\right)\overline{E}^{\mathrm{int}}_{j+\frac12}+\frac{\delta^{\rho}_{j+\frac12}\overline{\Gamma}^{\mathrm{int}}_{j+\frac12}-\delta^{\Gamma}_{j+\frac12}\overline{\rho}^{\mathrm{int}}_{j+\frac12}}{2a^{\mathrm{int},+}_{j+\frac12}\overline{\Gamma}^{\mathrm{int}}_{j+\frac12}}\big(u^{\mathrm{int}}_{j+\frac12}\big)^2+\frac{\delta^{\Pi}_{j+\frac12}\overline{\Gamma}^{\mathrm{int}}_{j+\frac12}-\delta^{\Gamma}_{j+\frac12}\overline{\Pi}^{\mathrm{int}}_{j+\frac12}}{a^{\mathrm{int},+}_{j+\frac12}\overline{\Gamma}^{\mathrm{int}}_{j+\frac12}}.
\end{aligned}\tag{2.34}$$

Equipped with (2.31)–(2.34), we finalize the projection step by integrating the piecewise constant interpolant (2.25)–(2.26) over the cell C_j. This leads to the following cell averages at the time level $t=t^{n+1}$:

$$\begin{aligned}
\overline{\rho}^{\,n+1}_{j}&=\frac{1}{\Delta x}\int\limits_{C_j}\widetilde{\rho}^{\mathrm{int}}(x)\,\mathrm{d}x=\overline{\rho}^{\,\mathrm{int}}_{j}+\frac{\Delta t^n}{\Delta x}\Big[a^{+}_{j-\frac12}\big(\overline{\rho}^{\,\mathrm{int,R}}_{j-\frac12}-\overline{\rho}^{\,\mathrm{int}}_{j}\big)-a^{-}_{j+\frac12}\big(\overline{\rho}^{\,\mathrm{int,L}}_{j+\frac12}-\overline{\rho}^{\,\mathrm{int}}_{j}\big)\\
&\qquad+\max(u^{\mathrm{int}}_{j-\frac12},0)\big(\overline{\rho}^{\,\mathrm{int,L}}_{j-\frac12}-\overline{\rho}^{\,\mathrm{int,R}}_{j-\frac12}\big)+\min(u^{\mathrm{int}}_{j+\frac12},0)\big(\overline{\rho}^{\,\mathrm{int,L}}_{j+\frac12}-\overline{\rho}^{\,\mathrm{int,R}}_{j+\frac12}\big)\Big]\\
&\overset{(2.34)}{=}\overline{\rho}^{\,\mathrm{int}}_{j}+\frac{\Delta t^n}{\Delta x}\Big[a^{+}_{j-\frac12}\big(\overline{\rho}^{\,\mathrm{int}}_{j-\frac12}-\overline{\rho}^{\,\mathrm{int}}_{j}\big)-a^{-}_{j+\frac12}\big(\overline{\rho}^{\,\mathrm{int}}_{j+\frac12}-\overline{\rho}^{\,\mathrm{int}}_{j}\big)+\alpha^{\mathrm{int}}_{j-\frac12}\delta^{\rho}_{j-\frac12}-\alpha^{\mathrm{int}}_{j+\frac12}\delta^{\rho}_{j+\frac12}\Big],
\end{aligned}\tag{2.35}$$

$$\begin{aligned}
(\overline{\rho u})^{n+1}_{j}&=\frac{1}{\Delta x}\int\limits_{C_j}(\widetilde{\rho u})^{\mathrm{int}}(x)\,\mathrm{d}x\\
&=(\overline{\rho u})^{\mathrm{int}}_{j}+\frac{\Delta t^n}{\Delta x}\Big[a^{+}_{j-\frac12}\big((\overline{\rho u})^{\mathrm{int,R}}_{j-\frac12}-(\overline{\rho u})^{\mathrm{int}}_{j}\big)-a^{-}_{j+\frac12}\big((\overline{\rho u})^{\mathrm{int,L}}_{j+\frac12}-(\overline{\rho u})^{\mathrm{int}}_{j}\big)\\
&\quad+\max(u^{\mathrm{int}}_{j-\frac12},0)\big((\overline{\rho u})^{\mathrm{int,L}}_{j-\frac12}-(\overline{\rho u})^{\mathrm{int,R}}_{j-\frac12}\big)+\min(u^{\mathrm{int}}_{j+\frac12},0)\big((\overline{\rho u})^{\mathrm{int,L}}_{j+\frac12}-(\overline{\rho u})^{\mathrm{int,R}}_{j+\frac12}\big)\Big]\\
&\overset{(2.34)}{=}(\overline{\rho u})^{\mathrm{int}}_{j}+\frac{\Delta t^n}{\Delta x}\Big[a^{+}_{j-\frac12}\big((\overline{\rho u})^{\mathrm{int}}_{j-\frac12}-(\overline{\rho u})^{\mathrm{int}}_{j}\big)-a^{-}_{j+\frac12}\big((\overline{\rho u})^{\mathrm{int}}_{j+\frac12}-(\overline{\rho u})^{\mathrm{int}}_{j}\big)\\
&\qquad+\alpha^{\mathrm{int}}_{j-\frac12}\delta^{\rho}_{j-\frac12}u^{\mathrm{int}}_{j-\frac12}-\alpha^{\mathrm{int}}_{j+\frac12}\delta^{\rho}_{j+\frac12}u^{\mathrm{int}}_{j+\frac12}\Big],
\end{aligned}\tag{2.36}$$

$$
\begin{aligned}
\overline{E}_j^{n+1} &= \frac{1}{\Delta x}\int\limits_{C_j} \widetilde{E}^{\,\mathrm{int}}(x)\,\mathrm{d}x = \overline{E}_j^{\,\mathrm{int}} + \frac{\Delta t^n}{\Delta x}\Big[a^+_{j-\frac12}\big(\overline{E}^{\,\mathrm{int,R}}_{j-\frac12} - \overline{E}_j^{\,\mathrm{int}}\big) - a^-_{j+\frac12}\big(\overline{E}^{\,\mathrm{int,L}}_{j+\frac12} - \overline{E}_j^{\,\mathrm{int}}\big) \\
&\qquad + \max(u^{\mathrm{int}}_{j-\frac12},0)\big(\overline{E}^{\,\mathrm{int,L}}_{j-\frac12} - \overline{E}^{\,\mathrm{int,R}}_{j-\frac12}\big) + \min(u^{\mathrm{int}}_{j+\frac12},0)\big(\overline{E}^{\,\mathrm{int,L}}_{j+\frac12} - \overline{E}^{\,\mathrm{int,R}}_{j+\frac12}\big)\Big] \\
&\overset{(2.34)}{=} \overline{E}_j^{\,\mathrm{int}} + \frac{\Delta t^n}{\Delta x}\Bigg[a^+_{j-\frac12}\big(\overline{E}^{\,\mathrm{int}}_{j-\frac12} - \overline{E}_j^{\,\mathrm{int}}\big) - a^-_{j+\frac12}\big(\overline{E}^{\,\mathrm{int}}_{j+\frac12} - \overline{E}_j^{\,\mathrm{int}}\big) \\
&\quad + \alpha^{\mathrm{int}}_{j-\frac12}\left\{\frac{\delta^{\rho}_{j-\frac12}\overline{\Gamma}^{\,\mathrm{int}}_{j-\frac12} - \delta^{\Gamma}_{j-\frac12}\overline{\rho}^{\,\mathrm{int}}_{j-\frac12}}{2\overline{\Gamma}^{\,\mathrm{int}}_{j-\frac12}}\big(u^{\mathrm{int}}_{j-\frac12}\big)^2 + \frac{\delta^{\Pi}_{j-\frac12}\overline{\Gamma}^{\,\mathrm{int}}_{j-\frac12} - \delta^{\Gamma}_{j-\frac12}\overline{\Pi}^{\,\mathrm{int}}_{j-\frac12}}{\overline{\Gamma}^{\,\mathrm{int}}_{j-\frac12}} + \frac{\delta^{\Gamma}_{j-\frac12}}{\overline{\Gamma}^{\,\mathrm{int}}_{j-\frac12}}\overline{E}^{\,\mathrm{int}}_{j-\frac12}\right\} \\
&\quad - \alpha^{\mathrm{int}}_{j+\frac12}\left\{\frac{\delta^{\rho}_{j+\frac12}\overline{\Gamma}^{\,\mathrm{int}}_{j+\frac12} - \delta^{\Gamma}_{j+\frac12}\overline{\rho}^{\,\mathrm{int}}_{j+\frac12}}{2\overline{\Gamma}^{\,\mathrm{int}}_{j+\frac12}}\big(u^{\mathrm{int}}_{j+\frac12}\big)^2 + \frac{\delta^{\Pi}_{j+\frac12}\overline{\Gamma}^{\,\mathrm{int}}_{j+\frac12} - \delta^{\Gamma}_{j+\frac12}\overline{\Pi}^{\,\mathrm{int}}_{j+\frac12}}{\overline{\Gamma}^{\,\mathrm{int}}_{j+\frac12}} + \frac{\delta^{\Gamma}_{j+\frac12}}{\overline{\Gamma}^{\,\mathrm{int}}_{j+\frac12}}\overline{E}^{\,\mathrm{int}}_{j+\frac12}\right\}\Bigg],
\end{aligned}
\tag{2.37}
$$

$$
\begin{aligned}
\overline{\Gamma}_j^{n+1} &= \frac{1}{\Delta x}\int\limits_{C_j} \widetilde{\Gamma}^{\,\mathrm{int}}(x)\,\mathrm{d}x = \overline{\Gamma}_j^{\,\mathrm{int}} + \frac{\Delta t^n}{\Delta x}\Big[a^+_{j-\frac12}\big(\overline{\Gamma}^{\,\mathrm{int,R}}_{j-\frac12} - \overline{\Gamma}_j^{\,\mathrm{int}}\big) - a^-_{j+\frac12}\big(\overline{\Gamma}^{\,\mathrm{int,L}}_{j+\frac12} - \overline{\Gamma}_j^{\,\mathrm{int}}\big) \\
&\qquad + \max(u^{\mathrm{int}}_{j-\frac12},0)\big(\overline{\Gamma}^{\,\mathrm{int,L}}_{j-\frac12} - \overline{\Gamma}^{\,\mathrm{int,R}}_{j-\frac12}\big) + \min(u^{\mathrm{int}}_{j+\frac12},0)\big(\overline{\Gamma}^{\,\mathrm{int,L}}_{j+\frac12} - \overline{\Gamma}^{\,\mathrm{int,R}}_{j+\frac12}\big)\Big] \\
&\overset{(2.34)}{=} \overline{\Gamma}_j^{\,\mathrm{int}} + \frac{\Delta t^n}{\Delta x}\Big[a^+_{j-\frac12}\big(\overline{\Gamma}^{\,\mathrm{int}}_{j-\frac12} - \overline{\Gamma}_j^{\,\mathrm{int}}\big) - a^-_{j+\frac12}\big(\overline{\Gamma}^{\,\mathrm{int}}_{j+\frac12} - \overline{\Gamma}_j^{\,\mathrm{int}}\big) + \alpha^{\mathrm{int}}_{j-\frac12}\delta^{\Gamma}_{j-\frac12} - \alpha^{\mathrm{int}}_{j+\frac12}\delta^{\Gamma}_{j+\frac12}\Big],
\end{aligned}
\tag{2.38}
$$

$$
\begin{aligned}
\overline{\Pi}_j^{n+1} &= \frac{1}{\Delta x}\int\limits_{C_j} \widetilde{\Pi}^{\,\mathrm{int}}(x)\,\mathrm{d}x = \overline{\Pi}_j^{\,\mathrm{int}} + \frac{\Delta t^n}{\Delta x}\Big[a^+_{j-\frac12}\big(\overline{\Pi}^{\,\mathrm{int,R}}_{j-\frac12} - \overline{\Pi}_j^{\,\mathrm{int}}\big) - a^-_{j+\frac12}\big(\overline{\Pi}^{\,\mathrm{int,L}}_{j+\frac12} - \overline{\Pi}_j^{\,\mathrm{int}}\big) \\
&\qquad + \max(u^{\mathrm{int}}_{j-\frac12},0)\big(\overline{\Pi}^{\,\mathrm{int,L}}_{j-\frac12} - \overline{\Pi}^{\,\mathrm{int,R}}_{j-\frac12}\big) + \min(u^{\mathrm{int}}_{j+\frac12},0)\big(\overline{\Pi}^{\,\mathrm{int,L}}_{j+\frac12} - \overline{\Pi}^{\,\mathrm{int,R}}_{j+\frac12}\big)\Big] \\
&\overset{(2.34)}{=} \overline{\Pi}_j^{\,\mathrm{int}} + \frac{\Delta t^n}{\Delta x}\Big[a^+_{j-\frac12}\big(\overline{\Pi}^{\,\mathrm{int}}_{j-\frac12} - \overline{\Pi}_j^{\,\mathrm{int}}\big) - a^-_{j+\frac12}\big(\overline{\Pi}^{\,\mathrm{int}}_{j+\frac12} - \overline{\Pi}_j^{\,\mathrm{int}}\big) + \alpha^{\mathrm{int}}_{j-\frac12}\delta^{\Pi}_{j-\frac12} - \alpha^{\mathrm{int}}_{j+\frac12}\delta^{\Pi}_{j+\frac12}\Big],
\end{aligned}
\tag{2.39}
$$

where

$$
\alpha^{\mathrm{int}}_{j+\frac12} = \begin{cases} \dfrac{a^+_{j+\frac12}}{a^+_{j+\frac12} - u^{\mathrm{int}}_{j+\frac12}} & \text{if } u^{\mathrm{int}}_{j+\frac12} < 0, \\[2ex] \dfrac{a^-_{j+\frac12}}{a^-_{j+\frac12} - u^{\mathrm{int}}_{j+\frac12}} & \text{otherwise.} \end{cases}
\tag{2.40}
$$

2.2.2. Semi-discrete scheme

Finally, we pass to the semi-discrete limit $\Delta t^n \to 0$ in (2.35)–(2.39) and proceed as in [14,32] to end up with the semi-discretization (2.2) with the modified (compared with (2.3)) numerical fluxes

$$
\boldsymbol{\mathcal{K}}_{j+\frac12} = \frac{a^+_{j+\frac12}\boldsymbol{K}^-_{j+\frac12} - a^-_{j+\frac12}\boldsymbol{K}^+_{j+\frac12}}{a^+_{j+\frac12} - a^-_{j+\frac12}} + \frac{a^+_{j+\frac12}a^-_{j+\frac12}}{a^+_{j+\frac12} - a^-_{j+\frac12}}\Big(\boldsymbol{U}^+_{j+\frac12} - \boldsymbol{U}^-_{j+\frac12}\Big) + \boldsymbol{q}_{j+\frac12},
\tag{2.41}
$$

where

$$
\boldsymbol{q}_{j+\frac12} = \alpha^*_{j+\frac12}\left\{q^{\rho}_{j+\frac12}\left(1, u^*_{j+\frac12}, \frac{\big(u^*_{j+\frac12}\big)^2}{2}, 0, 0\right)^{\top} + q^{\Gamma}_{j+\frac12}(0,0,p^*_{j+\frac12},1,0)^{\top} + q^{\Pi}_{j+\frac12}(0,0,1,0,1)^{\top}\right\}
\tag{2.42}
$$

is a built-in "anti-diffusion" term. In (2.42),

$$
\begin{aligned}
&\boldsymbol{U}^*_{j+\frac12}=\frac{a^+_{j+\frac12}\boldsymbol{U}^+_{j+\frac12}-a^-_{j+\frac12}\boldsymbol{U}^-_{j+\frac12}-\left(\boldsymbol{K}^+_{j+\frac12}-\boldsymbol{K}^-_{j+\frac12}\right)}{a^+_{j+\frac12}-a^-_{j+\frac12}},\quad u^*_{j+\frac12}=\frac{(\rho u)^*_{j+\frac12}}{\rho^*_{j+\frac12}},\\
&p^*_{j+\frac12}=\frac{1}{\Gamma^*_{j+\frac12}}\left[E^*_{j+\frac12}-\frac{\left((\rho u)^*_{j+\frac12}\right)^2}{2\rho^*_{j+\frac12}}-\Pi^*_{j+\frac12}\right],\\
&q^{\rho}_{j+\frac12}=\operatorname{minmod}\left(-a^{*,-}_{j+\frac12}\left(\rho^*_{j+\frac12}-\rho^-_{j+\frac12}\right),a^{*,+}_{j+\frac12}\left(\rho^+_{j+\frac12}-\rho^*_{j+\frac12}\right)\right),\\
&q^{\Gamma}_{j+\frac12}=\operatorname{minmod}\left(-a^{*,-}_{j+\frac12}\left(\Gamma^*_{j+\frac12}-\Gamma^-_{j+\frac12}\right),a^{*,+}_{j+\frac12}\left(\Gamma^+_{j+\frac12}-\Gamma^*_{j+\frac12}\right)\right),\\
&q^{\Pi}_{j+\frac12}=\operatorname{minmod}\left(-a^{*,-}_{j+\frac12}\left(\Pi^*_{j+\frac12}-\Pi^-_{j+\frac12}\right),a^{*,+}_{j+\frac12}\left(\Pi^+_{j+\frac12}-\Pi^*_{j+\frac12}\right)\right),\\
&a^{*,\pm}_{j+\frac12}=a^{\pm}_{j+\frac12}-u^*_{j+\frac12},\quad \alpha^*_{j+\frac12}=\begin{cases}\dfrac{a^+_{j+\frac12}}{a^{*,+}_{j+\frac12}} & \text{if } u^*_{j+\frac12}<0,\\[2ex] \dfrac{a^-_{j+\frac12}}{a^{*,-}_{j+\frac12}} & \text{otherwise.}\end{cases}
\end{aligned}
\tag{2.43}
$$

Remark 2.4. If we replace (2.26) with the following limited linear piece:

$$
\widetilde{\boldsymbol{U}}^{\,\mathrm{int}}_{j+\frac12}(x)=\overline{\boldsymbol{U}}^{\,\mathrm{int}}_{j+\frac12}+(\boldsymbol{U}_x)^{\mathrm{int}}_{j+\frac12}\left(x-\frac{x_{j+\frac12,r}+x_{j+\frac12,\ell}}{2}\right),
$$

where

$$
(\boldsymbol{U}_x)^{\mathrm{int}}_{j+\frac12}=\operatorname{minmod}\left(\frac{\boldsymbol{U}^{\mathrm{int}}_{j+\frac12,r}-\overline{\boldsymbol{U}}^{\,\mathrm{int}}_{j+\frac12}}{\delta},\frac{\overline{\boldsymbol{U}}^{\,\mathrm{int}}_{j+\frac12}-\boldsymbol{U}^{\mathrm{int}}_{j+\frac12,\ell}}{\delta}\right),\quad \delta:=\frac{\Delta t^n}{2}\left(a^+_{j+\frac12}-a^-_{j+\frac12}\right),
$$

we will end up with an alternative built-in "anti-diffusion" term

$$
\boldsymbol{q}_{j+\frac12}=-\frac{a^+_{j+\frac12}a^-_{j+\frac12}}{a^+_{j+\frac12}-a^-_{j+\frac12}}\operatorname{minmod}\left(\boldsymbol{U}^*_{j+\frac12}-\boldsymbol{U}^-_{j+\frac12},\boldsymbol{U}^+_{j+\frac12}-\boldsymbol{U}^*_{j+\frac12}\right),
$$

which was introduced in [28]. This will result in another flux globalization based PCCU scheme for the γ-based multifluid system. In the numerical results reported in §4, we will compare the behavior of this PCCU scheme with the proposed LD PCCU one.

Remark 2.5. We stress that the second-order semi-discrete LD PCCU scheme can be rewritten in the form without global fluxes. To this end, we substitute (2.4)–(2.6) into (2.2), (2.41) and end up with

$$
\frac{\mathrm{d}\overline{\boldsymbol{U}}_j}{\mathrm{d}t}=-\frac{\boldsymbol{\mathcal{F}}_{j+\frac12}-\boldsymbol{\mathcal{F}}_{j-\frac12}}{\Delta x}+\frac{1}{\Delta x}\left[\boldsymbol{B}_j-\frac{a^-_{j+\frac12}}{a^+_{j+\frac12}-a^-_{j+\frac12}}\boldsymbol{B}_{\boldsymbol{\Psi},j+\frac12}+\frac{a^+_{j-\frac12}}{a^+_{j-\frac12}-a^-_{j-\frac12}}\boldsymbol{B}_{\boldsymbol{\Psi},j-\frac12}\right],
$$

where

$$
\boldsymbol{\mathcal{F}}_{j+\frac12}=\frac{a^+_{j+\frac12}\boldsymbol{F}(\boldsymbol{U}^-_{j+\frac12})-a^-_{j+\frac12}\boldsymbol{F}(\boldsymbol{U}^+_{j+\frac12})}{a^+_{j+\frac12}-a^-_{j+\frac12}}+\frac{a^+_{j+\frac12}a^-_{j+\frac12}}{a^+_{j+\frac12}-a^-_{j+\frac12}}\left(\boldsymbol{U}^+_{j+\frac12}-\boldsymbol{U}^-_{j+\frac12}\right)+\boldsymbol{q}_{j+\frac12}.
$$

In addition, in (2.43) used to compute $\boldsymbol{q}_{j+\frac12}$, the formula for $\boldsymbol{U}^*_{j+\frac12}$ will become

$$
\boldsymbol{U}^*_{j+\frac12}=\frac{a^+_{j+\frac12}\boldsymbol{U}^+_{j+\frac12}-a^-_{j+\frac12}\boldsymbol{U}^-_{j+\frac12}-\left(\boldsymbol{F}(\boldsymbol{U}^+_{j+\frac12})-\boldsymbol{F}(\boldsymbol{U}^-_{j+\frac12})\right)+\boldsymbol{B}_{\boldsymbol{\Psi},j+\frac12}}{a^+_{j+\frac12}-a^-_{j+\frac12}}.
$$

2.2.3. Properties of the semi-discrete scheme

In this section, we establish two important properties the designed semi-discrete scheme satisfies:

1. When initially $\gamma \equiv \text{Const}$ and $\pi_\infty \equiv \text{Const}$, that is, if initially the system contains a single fluid, then γ and π_∞ will stay constant for all t;

2. At the isolated material interface at which initially $u \equiv \text{Const}$ and $p \equiv \text{Const}$, both u and p will stay constant for all t.

To this end, we prove the following theorem.

Theorem 2.6. *1. If* $\overline{\Gamma}_j \equiv \widehat{\Gamma} = \text{Const}$ *and* $\overline{\Pi}_j \equiv \widehat{\Pi} = \text{Const}$ *for all* j *at a certain time level* t*, then*

$$\frac{\mathrm{d}}{\mathrm{d}t}\overline{\Gamma}_j = \frac{\mathrm{d}}{\mathrm{d}t}\overline{\Pi}_j \equiv 0, \quad \forall j.$$

2. If at a certain time level $t = t^n$, $u_j^n \equiv \widehat{u} = \text{Const}$ *and* $p_j^n \equiv \widehat{p} = \text{Const}$ *for all* j*, then at the next time level* $t = t^{n+1}$,

$$u_j^{n+1} \equiv \widehat{u} \quad \text{and} \quad p_j^{n+1} \equiv \widehat{p}, \quad \forall j, \tag{2.44}$$

provided the ODE system (2.2), (2.41)–(2.43) is discretized using the forward Euler method.

Proof: 1. We only show that $\frac{\mathrm{d}}{\mathrm{d}t}\overline{\Gamma}_j \equiv 0$ as $\frac{\mathrm{d}}{\mathrm{d}t}\overline{\Pi}_j \equiv 0$ can be proved in a similar way. Since the point values of Γ at the cell interfaces are obtained using the piecewise linear reconstruction (2.16), we have $\Gamma^+_{j+\frac12} = \Gamma^-_{j+\frac12} = \Gamma^+_{j-\frac12} \equiv \widehat{\Gamma}$, which we substitute into (2.18), (2.19), and (2.21) to obtain

$$\left(F^{(4)}\right)^{\pm}_{j+\frac12} = \widehat{\Gamma} u^{\pm}_{j+\frac12}, \quad B_j^{(4)} = \widehat{\Gamma}\left(u^-_{j+\frac12} - u^+_{j-\frac12}\right), \quad B^{(4)}_{\boldsymbol{\Psi},j+\frac12} = \widehat{\Gamma}\left(u^+_{j+\frac12} - u^-_{j+\frac12}\right). \tag{2.45}$$

We then use (2.4)–(2.6) to compute the flux differences

$$\begin{aligned}
&\left(K^{(4)}\right)^+_{j+\frac12} - \left(K^{(4)}\right)^-_{j+\frac12} = \left(F^{(4)}\right)^+_{j+\frac12} - \left(F^{(4)}\right)^-_{j+\frac12} - B^{(4)}_{\boldsymbol{\Psi},j+\frac12} \overset{(2.45)}{=} 0,\\
&\left(K^{(4)}\right)^-_{j+\frac12} - \left(K^{(4)}\right)^+_{j-\frac12} = \left(F^{(4)}\right)^-_{j+\frac12} - \left(F^{(4)}\right)^+_{j-\frac12} - B_j^{(4)} \overset{(2.45)}{=} 0,
\end{aligned} \tag{2.46}$$

which we substitute into (2.43) to verify that

$$q^{\Gamma}_{j+\frac12} = 0. \tag{2.47}$$

Finally, we substitute (2.46)–(2.47) into (2.2), (2.41)–(2.42) to end up with $\frac{\mathrm{d}}{\mathrm{d}t}\overline{\Gamma}_j \equiv 0$. This completes the proof of the first part of the theorem.

2. Since the point values of u and p at the cell interfaces are computed using the piecewise linear reconstruction (2.16), we have $u^+_{j+\frac12} = u^-_{j+\frac12} = u^+_{j-\frac12} \equiv \widehat{u}$ and $p^+_{j+\frac12} = p^-_{j+\frac12} = p^+_{j-\frac12} \equiv \widehat{p}$ at the time level $t = t^n$. This results in

$$\begin{aligned}
&\boldsymbol{U}^{\pm}_{j+\frac12} = \left(\rho^{\pm}_{j+\frac12}, \rho^{\pm}_{j+\frac12}\widehat{u}, E^{\pm}_{j+\frac12}, \Gamma^{\pm}_{j+\frac12}, \Pi^{\pm}_{j+\frac12}\right)^{\top}, \quad E^{\pm}_{j+\frac12} = \widehat{p}\,\Gamma^{\pm}_{j+\frac12} + \frac{\widehat{u}^2}{2}\rho^{\pm}_{j+\frac12} + \Pi^{\pm}_{j+\frac12},\\
&\boldsymbol{F}^{\pm}_{j+\frac12} = \left(\rho^{\pm}_{j+\frac12}\widehat{u}, \rho^{\pm}_{j+\frac12}\widehat{u}^2 + \widehat{p}, \widehat{u}(E^{\pm}_{j+\frac12} + \widehat{p}), \Gamma^{\pm}_{j+\frac12}\widehat{u}, \Pi^{\pm}_{j+\frac12}\widehat{u}\right)^{\top},
\end{aligned} \tag{2.48}$$

and hence, after substituting $u^{\pm}_{j+\frac12}$ into (2.19) and (2.21), we obtain

$$\boldsymbol{B}_j = \boldsymbol{B}_{\boldsymbol{\Psi},j+\frac12} \equiv \boldsymbol{0}.$$

The latter equality implies $\boldsymbol{K}^{\pm}_{j+\frac12} = \boldsymbol{F}^{\pm}_{j+\frac12}$, which together with (2.48) results in

$$\boldsymbol{F}^+_{j+\frac12} - \boldsymbol{F}^-_{j+\frac12} = \widehat{u}(\boldsymbol{U}^+_{j+\frac12} - \boldsymbol{U}^+_{j+\frac12}),$$

so that the first line in (2.43) can be rewritten as

$$\boldsymbol{U}^*_{j+\frac12} = \frac{a^+_{j+\frac12}\boldsymbol{U}^+_{j+\frac12} - a^-_{j+\frac12}\boldsymbol{U}^-_{j+\frac12} - \widehat{u}\left(\boldsymbol{U}^+_{j+\frac12} - \boldsymbol{U}^-_{j+\frac12}\right)}{a^+_{j+\frac12} - a^-_{j+\frac12}}, \quad u^*_{j+\frac12} = \widehat{u}. \tag{2.49}$$

We then use (2.42), (2.43), (2.48), and (2.49) to compute the "anti-diffusion" term, which reduces to

$$\boldsymbol{q}_{j+\frac12} = \alpha^*_{j+\frac12}\left(q^{\rho}_{j+\frac12}, \widehat{u}\,q^{\rho}_{j+\frac12}, \widehat{p}\,q^{\Gamma}_{j+\frac12} + \frac{\widehat{u}^2}{2}q^{\rho}_{j+\frac12} + q^{\Pi}_{j+\frac12}, q^{\Gamma}_{j+\frac12}, q^{\Pi}_{j+\frac12}\right)^{\top}, \tag{2.50}$$

and then substitute (2.48) and (2.50) into (2.41) to obtain the numerical fluxes

$$\boldsymbol{\mathcal{K}}_{j+\frac{1}{2}}=\left(\mathcal{K}^{(1)}_{j+\frac{1}{2}},\widehat{u}\,\mathcal{K}^{(1)}_{j+\frac{1}{2}}+\widehat{p},\widehat{p}\,\mathcal{K}^{(4)}_{j+\frac{1}{2}}+\frac{\widehat{u}^2}{2}\mathcal{K}^{(1)}_{j+\frac{1}{2}}+\mathcal{K}^{(5)}_{j+\frac{1}{2}}+\widehat{u}\widehat{p},\mathcal{K}^{(4)}_{j+\frac{1}{2}},\mathcal{K}^{(5)}_{j+\frac{1}{2}}\right)^{\top},$$

which, in turn, are substituted into (2.2) to obtain the following semi-discrete relations:

$$\frac{\mathrm{d}}{\mathrm{d}t}(\overline{\rho u})^n_j=\widehat{u}\,\frac{\mathrm{d}}{\mathrm{d}t}\overline{\rho}^n_j,\quad \frac{\mathrm{d}}{\mathrm{d}t}\overline{E}^n_j=\widehat{p}\,\frac{\mathrm{d}}{\mathrm{d}t}\overline{\Gamma}^n_j+\frac{\widehat{u}^2}{2}\frac{\mathrm{d}}{\mathrm{d}t}\overline{\rho}^n_j+\frac{\mathrm{d}}{\mathrm{d}t}\overline{\Pi}^n_j.$$

These relations are discretized using the forward Euler method, which results in

$$\begin{aligned}&\frac{(\overline{\rho u})^{n+1}_j-(\overline{\rho u})^n_j}{\Delta t}=\widehat{u}\,\frac{\overline{\rho}^{n+1}_j-\overline{\rho}^n_j}{\Delta t},\\&\frac{\overline{E}^{n+1}_j-\overline{E}^n_j}{\Delta t}=\widehat{p}\,\frac{\overline{\Gamma}^{n+1}_j-\overline{\Gamma}^n_j}{\Delta t}+\frac{\widehat{u}^2}{2}\cdot\frac{\overline{\rho}^{n+1}_j-\overline{\rho}^n_j}{\Delta t}+\frac{\overline{\Pi}^{n+1}_j-\overline{\Pi}^n_j}{\Delta t}.\end{aligned}\tag{2.51}$$

Finally, we substitute (2.11) expressed at both time levels $t=t^n$ and $t=t^{n+1}$ into (2.51) to end up with (2.44). This completes the proof of the second part of the theorem. ■

Remark 2.7. The second part of Theorem 2.6 is still true if the forward Euler time discretization is replaced with another strong stability preserving (SSP) ODE solver; see, e.g., [19,20].

Remark 2.8. As in [32], the computation of numerical fluxes in (2.41) should be desingularized to avoid division by zero or very small numbers. If $a^+_{j+\frac{1}{2}}<\varepsilon_2$ and $a^-_{j+\frac{1}{2}}>-\varepsilon_2$ for a small positive ε_2, we replace the fluxes $\boldsymbol{\mathcal{K}}_{j+\frac{1}{2}}$ with

$$\boldsymbol{\mathcal{K}}_{j+\frac{1}{2}}=\frac{\boldsymbol{K}\left(\boldsymbol{U}^-_{j+\frac{1}{2}}\right)+\boldsymbol{K}\left(\boldsymbol{U}^+_{j+\frac{1}{2}}\right)}{2}.$$

In all of the numerical examples reported in §4, we have taken $\varepsilon_2=10^{-12}$.

2.3. Flux globalization based LD ai-WENO PCCU scheme

In this section, we extend the second-order flux globalization based LD PCCU schemes from §2.2 to the fifth order of accuracy within the A-WENO framework.

The semi-discrete fifth-order LD Ai-WENO PCCU scheme for the 1-D quasi-conservative system (2.1) reads as

$$\frac{\mathrm{d}}{\mathrm{d}t}\boldsymbol{U}_j=-\frac{\boldsymbol{\mathcal{H}}_{j+\frac{1}{2}}-\boldsymbol{\mathcal{H}}_{j-\frac{1}{2}}}{\Delta x},\tag{2.52}$$

where $\boldsymbol{U}_j:\approx\boldsymbol{U}(x_j,t)$ and the fifth-order numerical fluxes $\boldsymbol{\mathcal{H}}_{j+\frac{1}{2}}$ are defined by

$$\boldsymbol{\mathcal{H}}_{j+\frac{1}{2}}=\boldsymbol{\mathcal{K}}_{j+\frac{1}{2}}-\frac{(\Delta x)^2}{24}(\boldsymbol{K}_{xx})_{j+\frac{1}{2}}+\frac{7(\Delta x)^4}{5760}(\boldsymbol{K}_{xxxx})_{j+\frac{1}{2}}.\tag{2.53}$$

Here, $\boldsymbol{\mathcal{K}}_{j+\frac{1}{2}}$ are the finite-volume fluxes (2.41)–(2.43), and $(\boldsymbol{K}_{xx})_{j+\frac{1}{2}}$ and $(\boldsymbol{K}_{xxxx})_{j+\frac{1}{2}}$ are approximations of the second- and fourth-order spatial derivatives of $\boldsymbol{K}$ at $x=x_{j+\frac{1}{2}}$, which we compute using the finite-difference approximations recently proposed in [15]:

$$\begin{aligned}&(\boldsymbol{K}_{xx})_{j+\frac{1}{2}}=\frac{1}{12(\Delta x)^2}\left[-\boldsymbol{\mathcal{K}}_{j-\frac{3}{2}}+16\boldsymbol{\mathcal{K}}_{j-\frac{1}{2}}-30\boldsymbol{\mathcal{K}}_{j+\frac{1}{2}}+16\boldsymbol{\mathcal{K}}_{j+\frac{3}{2}}-\boldsymbol{\mathcal{K}}_{j+\frac{5}{2}}\right],\\&(\boldsymbol{K}_{xxxx})_{j+\frac{1}{2}}=\frac{1}{(\Delta x)^4}\left[\boldsymbol{\mathcal{K}}_{j-\frac{3}{2}}-4\boldsymbol{\mathcal{K}}_{j-\frac{1}{2}}+6\boldsymbol{\mathcal{K}}_{j+\frac{1}{2}}-4\boldsymbol{\mathcal{K}}_{j+\frac{3}{2}}+\boldsymbol{\mathcal{K}}_{j+\frac{5}{2}}\right].\end{aligned}\tag{2.54}$$

The resulting semi-discrete scheme (2.52)–(2.54) will be fifth-order accurate provided the point values $\boldsymbol{U}^{\pm}_{j+\frac{1}{2}}$ are calculated using a fifth-order interpolation. To this end, we apply the recently proposed fifth-order Ai-WENO-Z interpolation [17,34,50], which we briefly describe in Appendix A.

Remark 2.9. In order to ensure the designed LD Ai-WENO PCCU scheme is fifth-order accurate, the term $\boldsymbol{B}_j$ needs to be evaluated using at least a fifth-order quadrature. In this paper, we use the same Newton-Cotes quadrature introduced in [12]; see also [11].

Remark 2.10. We note that the fifth-order semi-discrete flux globalization based LD Ai-WENO PCCU scheme also satisfies the two properties specified in Theorem 2.5. The proof of this fact is a direct extension of the proof of Theorem 2.5 as both Γ and Π are

characteristic variables and when they are constants, the Ai-WENO-Z interpolation is exact for these components. We omit the details of the proof for the sake of brevity.

3. Two-dimensional algorithms

In this section, we extend the proposed 1-D flux globalization based LD A-WENO PCCU schemes to the 2-D γ-based multifluid system (1.1), (1.2), (1.4). This system can be written in the vector form

$$\boldsymbol{U}_t+\boldsymbol{F}(\boldsymbol{U})_x+\boldsymbol{G}(\boldsymbol{U})_y=B(\boldsymbol{U})\boldsymbol{U}_x+C(\boldsymbol{U})\boldsymbol{U}_y,$$

or, equivalently, in the quasi-conservative form

$$\boldsymbol{U}_t+\boldsymbol{K}(\boldsymbol{U})_x+\boldsymbol{L}(\boldsymbol{U})_y=\boldsymbol{0} \tag{3.1}$$

with

$$\begin{aligned}&\boldsymbol{K}(\boldsymbol{U})=\boldsymbol{F}(\boldsymbol{U})-\boldsymbol{R}(\boldsymbol{U}),\quad \boldsymbol{L}(\boldsymbol{U})=\boldsymbol{G}(\boldsymbol{U})-\boldsymbol{S}(\boldsymbol{U}),\\ &\boldsymbol{R}(\boldsymbol{U})=\int\limits_{\widehat{x}}^{x}B(\boldsymbol{U})\boldsymbol{U}_\xi\,\mathrm{d}\xi,\quad \boldsymbol{S}(\boldsymbol{U})=\int\limits_{\widehat{y}}^{y}C(\boldsymbol{U})\boldsymbol{U}_\eta\,\mathrm{d}\eta.\end{aligned} \tag{3.2}$$

Here,

$$\begin{aligned}&\boldsymbol{U}:=(\rho,\rho u,\rho v,E,\Gamma,\Pi)^\top,\\ &\boldsymbol{F}(\boldsymbol{U})=(\rho u,\rho u^2+p,\rho uv,u(E+p),u\Gamma,u\Pi)^\top,\quad B(\boldsymbol{U})\boldsymbol{U}_x=\big(0,0,0,0,\Gamma u_x,\Pi u_x\big)^\top,\\ &\boldsymbol{G}(\boldsymbol{U})=(\rho v,\rho uv,\rho v^2+p,v(E+p),v\Gamma,v\Pi)^\top,\quad C(\boldsymbol{U})\boldsymbol{U}_y=\big(0,0,0,0,\Gamma v_y,\Pi v_y\big)^\top.\end{aligned} \tag{3.3}$$

We first introduce a uniform mesh consisting of the finite-volume cells $C_{j,k}:=[x_{j-\frac12},x_{j+\frac12}]\times[y_{k-\frac12},y_{k+\frac12}]$ of the uniform size $\Delta x\Delta y$ with $x_{j+\frac12}-x_{j-\frac12}\equiv\Delta x$ and $y_{k+\frac12}-y_{k-\frac12}\equiv\Delta y$ centered at (x_j,y_k) with $x_j=(x_{j-\frac12}+x_{j+\frac12})/2$ and $(y_{k-\frac12}+y_{k+\frac12})/2$, $j=1,\ldots,N_x$, $k=1,\ldots,N_y$.

We assume that at certain time level t, an approximate solution, realized in terms of the cell averages $\overline{\boldsymbol{U}}_{j,k}:\approx\frac{1}{\Delta x\Delta y}\iint_{C_{j,k}}\boldsymbol{U}(x,y,t)\,\mathrm{d}x\,\mathrm{d}y$, is available. These cell averages are then evolved in time by solving the following system of ODEs:

$$\frac{\mathrm{d}}{\mathrm{d}t}\overline{\boldsymbol{U}}_{j,k}=-\frac{\boldsymbol{\mathcal{K}}_{j+\frac12,k}-\boldsymbol{\mathcal{K}}_{j-\frac12,k}}{\Delta x}-\frac{\boldsymbol{\mathcal{L}}_{j,k+\frac12}-\boldsymbol{\mathcal{L}}_{j,k-\frac12}}{\Delta y}, \tag{3.4}$$

where the x- and y-numerical fluxes are

$$\boldsymbol{\mathcal{K}}_{j+\frac12,k}=\frac{a^+_{j+\frac12,k}\boldsymbol{K}^-_{j+\frac12,k}-a^-_{j+\frac12,k}\boldsymbol{K}^+_{j+\frac12,k}}{a^+_{j+\frac12,k}-a^-_{j+\frac12,k}}+\frac{a^+_{j+\frac12,k}a^-_{j+\frac12,k}}{a^+_{j+\frac12,k}-a^-_{j+\frac12,k}}\Big(\boldsymbol{U}^+_{j+\frac12,k}-\boldsymbol{U}^-_{j+\frac12,k}\Big)+\boldsymbol{q}_{j+\frac12,k}, \tag{3.5}$$

$$\boldsymbol{\mathcal{L}}_{j,k+\frac12}=\frac{b^+_{j,k+\frac12}\boldsymbol{L}^-_{j,k+\frac12}-b^-_{j,k+\frac12}\boldsymbol{L}^+_{j,k+\frac12}}{b^+_{j,k+\frac12}-b^-_{j,k+\frac12}}+\frac{b^+_{j,k+\frac12}b^-_{j,k+\frac12}}{b^+_{j,k+\frac12}-b^-_{j,k+\frac12}}\Big(\boldsymbol{U}^+_{j,k+\frac12}-\boldsymbol{U}^-_{j,k+\frac12}\Big)+\boldsymbol{q}_{j,k+\frac12}. \tag{3.6}$$

The one-sided point values $\boldsymbol{U}^\pm_{j+\frac12,k}$ and $\boldsymbol{U}^\pm_{j,k+\frac12}$ at the cell interfaces $(x_{j+\frac12},y_k)$ and $(x_j,y_{k+\frac12})$, respectively, are obtained as follows. We first use the cell averages $\overline{\boldsymbol{U}}_{j,k}$ to compute the point values of u, v, and p at the cell centers:

$$u_{j,k}=\frac{(\overline{\rho u})_{j,k}}{\overline{\rho}_{j,k}},\quad v_{j,k}=\frac{(\overline{\rho v})_{j,k}}{\overline{\rho}_{j,k}},\quad p_{j,k}=\frac{1}{\overline{\Gamma}_{j,k}}\left[\overline{E}_{j,k}-\frac{\big((\overline{\rho u})_{j,k}\big)^2+\big((\overline{\rho v})_{j,k}\big)^2}{2\overline{\rho}_{j,k}}-\overline{\Pi}_{j,k}\right],$$

and then construct the linear pieces to approximate the primitive variables $\boldsymbol{V}=(\rho,u,v,p,\Gamma,\Pi)^\top$:

$$\widetilde{\boldsymbol{V}}_{j,k}(x,y)=\boldsymbol{V}_{j,k}+(\boldsymbol{V}_x)_{j,k}(x-x_j)+(\boldsymbol{V}_y)_{j,k}(y-y_k),\quad (x,y)\in C_{j,k}, \tag{3.7}$$

where $\boldsymbol{V}_{j,k}:=(\overline{\rho}_{j,k},u_{j,k},v_{j,k},p_{j,k},\overline{\Gamma}_{j,k},\overline{\Pi}_{j,k})^\top$ and $(\boldsymbol{V}_x)_{j,k}$ and $(\boldsymbol{V}_y)_{j,k}$ are the slopes, which are supposed to be computed using a nonlinear limiter.

As in the 1-D case, we use different limiters near and away from the material interfaces, which need to be detected. In the two-fluid case, we check whether

$$(\overline{\Gamma}_{j,k}-\widehat{\Gamma})(\overline{\Gamma}_{j+1,k}-\widehat{\Gamma})<0, \tag{3.8}$$

where, as before, $\widehat{\Gamma}=(\Gamma_{\rm I}+\Gamma_{\rm II})/2$. If (3.8) is satisfied, we then use the overcompressive SBM limiter,

$$(\boldsymbol{V}_x)_{\ell,k}=\phi^{\rm SBM}_{\theta,\tau}\left(\frac{\overline{\boldsymbol{V}}_{\ell+1,k}-\overline{\boldsymbol{V}}_{\ell,k}}{\overline{\boldsymbol{V}}_{\ell,k}-\overline{\boldsymbol{V}}_{\ell-1,k}}\right)\frac{\overline{\boldsymbol{V}}_{\ell+1,k}-\overline{\boldsymbol{V}}_{\ell,k}}{\Delta x},\tag{3.9}$$

for $\ell=j-1$, j, $j+1$, and $j+2$. In (3.9), the function $\phi^{\rm SBM}_{\theta,\tau}(r)$, given by (2.15), is applied in a componentwise manner with $\tau=-0.5$ and $\theta=1.3$. Otherwise, that is, away from the material interface, we use a dissipative generalized minmod limiter which is also given by the same formulae (3.9), (2.15), but with $\tau=0.5$ and $\theta=1.3$. We proceed similarly in the y-direction: we use

$$(\boldsymbol{V}_y)_{j,m}=\phi^{\rm SBM}_{\theta,\tau}\left(\frac{\overline{\boldsymbol{V}}_{j,m+1}-\overline{\boldsymbol{V}}_{j,m}}{\overline{\boldsymbol{V}}_{j,m}-\overline{\boldsymbol{V}}_{j,m-1}}\right)\frac{\overline{\boldsymbol{V}}_{j,m+1}-\overline{\boldsymbol{V}}_{j,m}}{\Delta y},\tag{3.10}$$

with $\tau=-0.5$ and $\theta=1.3$ for $m=k-1$, k, $k+1$, and $k+2$ if

$$(\overline{\Gamma}_{j,k}-\widehat{\Gamma})(\overline{\Gamma}_{j,k+1}-\widehat{\Gamma})<0,\tag{3.11}$$

is satisfied, and with $\tau=0.5$ and $\theta=1.3$ otherwise.

Equipped with $(\boldsymbol{V}_x)_{j,k}$ and $(\boldsymbol{V}_y)_{j,k}$, we use (3.7) to obtain

$$\begin{aligned}
&\boldsymbol{V}^-_{j+\frac12,k}=\overline{\boldsymbol{V}}_{j,k}+\frac{\Delta x}{2}(\boldsymbol{V}_x)_{j,k},\quad \boldsymbol{V}^+_{j+\frac12,k}=\overline{\boldsymbol{V}}_{j+1,k}-\frac{\Delta x}{2}(\boldsymbol{V}_x)_{j+1,k},\\
&\boldsymbol{V}^-_{j,k+\frac12}=\overline{\boldsymbol{V}}_{j,k}+\frac{\Delta y}{2}(\boldsymbol{V}_y)_{j,k},\quad \boldsymbol{V}^+_{j,k+\frac12}=\overline{\boldsymbol{V}}_{j,k+1}-\frac{\Delta y}{2}(\boldsymbol{V}_y)_{j,k+1},
\end{aligned}$$

and then the corresponding point values of the conservative variables $\boldsymbol{U}$ are

$$\boldsymbol{U}^\pm_{\ell,m}=\left(\rho^\pm_{\ell,m},\rho^\pm_{\ell,m}u^\pm_{\ell,m},\rho^\pm_{\ell,m}v^\pm_{\ell,m},E^\pm_{\ell,m},\Gamma^\pm_{\ell,m},\Pi^\pm_{\ell,m}\right)^\top,$$

for $(\ell,m)=(j+\frac12,k)$ and $(j,k+\frac12)$. Here, $E^\pm_{\ell,m}=\Gamma^\pm_{\ell,m}p^\pm_{\ell,m}+\rho^\pm_{\ell,m}((u^\pm_{\ell,m})^2+(v^\pm_{\ell,m})^2)/2+\Pi^\pm_{\ell,m}$.

The global fluxes $\boldsymbol{K}^\pm_{j+\frac12,k}$ and $\boldsymbol{\mathcal{L}}_{j,k+\frac12}$ in (3.5)–(3.6) are obtained using the relations in (3.2), namely, by

$$\boldsymbol{K}^\pm_{j+\frac12,k}=\boldsymbol{F}^\pm_{j+\frac12,k}-\boldsymbol{R}^\pm_{j+\frac12,k},\quad \boldsymbol{L}^\pm_{j,k+\frac12}=\boldsymbol{G}^\pm_{j,k+\frac12}-\boldsymbol{S}^\pm_{j,k+\frac12},$$

where $\boldsymbol{F}^\pm_{j+\frac12,k}:=\boldsymbol{F}(\boldsymbol{U}^\pm_{j+\frac12,k})$, $\boldsymbol{G}^\pm_{j,k+\frac12}:=\boldsymbol{G}(\boldsymbol{U}^\pm_{j,k+\frac12})$, and the point values of the global variables $\boldsymbol{R}$ and $\boldsymbol{S}$ are computed as follows. First, we set $\widehat{x}=x_{\frac12}$ and $\widehat{y}=y_{\frac12}$ so that $\boldsymbol{R}^-_{\frac12,k}:=\boldsymbol{0}$ and $\boldsymbol{S}^-_{j,\frac12}:=\boldsymbol{0}$. We then evaluate $\boldsymbol{R}^+_{\frac12,k}=\boldsymbol{B}_{\boldsymbol{\Psi},\frac12,k}$ and $\boldsymbol{S}^+_{j,\frac12}=\boldsymbol{B}_{\boldsymbol{\Psi},j,\frac12}$ and recursively compute the rest of the required point values:

$$\begin{aligned}
&\boldsymbol{R}^-_{j+\frac12,k}=\boldsymbol{R}^+_{j-\frac12,k}+\boldsymbol{B}^x_{j,k},\quad \boldsymbol{R}^+_{j+\frac12,k}=\boldsymbol{R}^-_{j+\frac12,k}+\boldsymbol{B}_{\boldsymbol{\Psi},j+\frac12,k},\quad j=1,\ldots,N_x,\\
&\boldsymbol{S}^-_{j,k+\frac12}=\boldsymbol{S}^+_{j,k-\frac12}+\boldsymbol{B}^y_{j,k},\quad \boldsymbol{S}^+_{j,k+\frac12}=\boldsymbol{S}^-_{j,k+\frac12}+\boldsymbol{B}_{\boldsymbol{\Psi},j,k+\frac12},\quad k=1,\ldots,N_y.
\end{aligned}$$

Here, $\boldsymbol{B}^x_{j,k}$, $\boldsymbol{B}_{\boldsymbol{\Psi},j+\frac12,k}$, $\boldsymbol{B}^y_{j,k}$, and $\boldsymbol{B}_{\boldsymbol{\Psi},j,k+\frac12,k}$ are evaluated precisely the same way as in §2.1.1:

$$\begin{aligned}
\boldsymbol{B}^x_{j,k}&=\left(0,0,0,0,\frac{\Gamma^-_{j+\frac12,k}+\Gamma^+_{j-\frac12,k}}{2}\left(u^-_{j+\frac12,k}-u^+_{j-\frac12,k}\right),\frac{\Pi^-_{j+\frac12,k}+\Pi^+_{j-\frac12,k}}{2}\left(u^-_{j+\frac12,k}-u^+_{j-\frac12,k}\right)\right)^\top,\\
\boldsymbol{B}_{\boldsymbol{\Psi},j+\frac12,k}&=\left(0,0,0,0,\frac{\Gamma^+_{j+\frac12,k}+\Gamma^-_{j+\frac12,k}}{2}\left(u^+_{j+\frac12,k}-u^-_{j+\frac12,k}\right),\frac{\Pi^+_{j+\frac12,k}+\Pi^-_{j+\frac12,k}}{2}\left(u^+_{j+\frac12,k}-u^-_{j+\frac12,k}\right)\right)^\top,\\
\boldsymbol{B}^y_{j,k}&=\left(0,0,0,0,\frac{\Gamma^-_{j,k+\frac12}+\Gamma^+_{j,k-\frac12}}{2}\left(v^-_{j,k+\frac12}-v^+_{j,k-\frac12}\right),\frac{\Pi^-_{j,k+\frac12}+\Pi^+_{j,k-\frac12}}{2}\left(v^-_{j,k+\frac12}-v^+_{j,k-\frac12}\right)\right)^\top,\\
\boldsymbol{B}_{\boldsymbol{\Psi},j,k+\frac12}&=\left(0,0,0,0,\frac{\Gamma^+_{j,k+\frac12}+\Gamma^-_{j,k+\frac12}}{2}\left(v^+_{j,k+\frac12}-v^-_{j,k+\frac12}\right),\frac{\Pi^+_{j,k+\frac12}+\Pi^-_{j,k+\frac12}}{2}\left(v^+_{j,k+\frac12}-v^-_{j,k+\frac12}\right)\right)^\top.
\end{aligned}$$

Finally, the one-sided local-speeds of propagation $a^{\pm}_{j+\frac{1}{2},k}$ and $b^{\pm}_{j,k+\frac{1}{2}}$ can be estimated by

$$
\begin{aligned}
a^{+}_{j+\frac{1}{2},k} &= \max\left\{u^{-}_{j+\frac{1}{2},k}+c^{-}_{j+\frac{1}{2},k}, u^{+}_{j+\frac{1}{2},k}+c^{+}_{j+\frac{1}{2},k}, 0\right\},\\
a^{-}_{j+\frac{1}{2},k} &= \min\left\{u^{-}_{j+\frac{1}{2},k}-c^{-}_{j+\frac{1}{2},k}, u^{+}_{j+\frac{1}{2},k}-c^{+}_{j+\frac{1}{2},k}, 0\right\},\\
b^{+}_{j,k+\frac{1}{2}} &= \max\left\{v^{-}_{j,k+\frac{1}{2}}+c^{-}_{j,k+\frac{1}{2}}, v^{+}_{j,k+\frac{1}{2}}+c^{+}_{j,k+\frac{1}{2}}, 0\right\},\\
b^{-}_{j,k+\frac{1}{2}} &= \min\left\{v^{-}_{j,k+\frac{1}{2}}-c^{-}_{j,k+\frac{1}{2}}, v^{+}_{j,k+\frac{1}{2}}-c^{+}_{j,k+\frac{1}{2}}, 0\right\}.
\end{aligned}
$$

3.1. "built-in" anti-diffusion

In this section, we discuss the derivation of the "built-in" anti-diffusion terms $\boldsymbol{q}_{j+\frac{1}{2},k}$ and $\boldsymbol{q}_{j,k+\frac{1}{2}}$ in (3.5)–(3.6) in a "dimension-by-dimension" manner following the idea introduced in [14,32].

In order to derive the formula for $\boldsymbol{q}_{j+\frac{1}{2},k}$, we consider the 1-D restriction of the system (3.1)–(3.3) along the lines $y=y_k$:

$$
\boldsymbol{U}_t(x,y_k,t)+\boldsymbol{K}\big(\boldsymbol{U}(x,y_k,t)\big)_x=\boldsymbol{0},\quad k=1,\ldots,N_y. \tag{3.12}
$$

We then can go through all of the steps in the derivation of the 1-D fully discrete scheme for the systems in (3.12) following §2.2.1 up to (2.26), which now reads as

$$
\widetilde{\boldsymbol{U}}^{\,\mathrm{int}}_{j+\frac{1}{2},k}(x,y_k)=\begin{cases}\overline{\boldsymbol{U}}^{\,\mathrm{int,L}}_{j+\frac{1}{2},k}, & x<\widetilde{x}_{j+\frac{1}{2}},\\ \overline{\boldsymbol{U}}^{\,\mathrm{int,R}}_{j+\frac{1}{2},k}, & x>\widetilde{x}_{j+\frac{1}{2}},\end{cases}
$$

where $\widetilde{x}_{j+\frac{1}{2}}=x_{j+\frac{1}{2}}+u^{\mathrm{int}}_{j+\frac{1}{2},k}\Delta t^n$, $u^{\mathrm{int}}_{j+\frac{1}{2},k}:=(\overline{\rho u})^{\mathrm{int}}_{j+\frac{1}{2},k}/\overline{\rho}^{\,\mathrm{int}}_{j+\frac{1}{2},k}$, and the corresponding local conservation requirements (2.27) become

$$
a^{\mathrm{int},+}_{j+\frac{1}{2},k}\,\overline{\boldsymbol{U}}^{\,\mathrm{int,R}}_{j+\frac{1}{2},k}-a^{\mathrm{int},-}_{j+\frac{1}{2},k}\,\overline{\boldsymbol{U}}^{\,\mathrm{int,L}}_{j+\frac{1}{2},k}=\big(a^{+}_{j+\frac{1}{2},k}-a^{-}_{j+\frac{1}{2},k}\big)\,\overline{\boldsymbol{U}}^{\,\mathrm{int}}_{j+\frac{1}{2},k}, \tag{3.13}
$$

where $a^{\mathrm{int},\pm}_{j+\frac{1}{2},k}:=a^{\pm}_{j+\frac{1}{2},k}-u^{\mathrm{int}}_{j+\frac{1}{2},k}$. In addition to the six conservation constraints given by (3.13), we have six degrees of freedom, which we use as in the 1-D case to enforce a sharp approximation of quasi 1-D isolated contact waves propagating in the x-direction. To this end, we enforce the continuity of u and p across the cell interfaces $x=x_{j+\frac{1}{2}}$ by setting

$$
\begin{aligned}
&\frac{(\overline{\rho u})^{\mathrm{int,L}}_{j+\frac{1}{2},k}}{\overline{\rho}^{\,\mathrm{int,L}}_{j+\frac{1}{2},k}}=\frac{(\overline{\rho u})^{\mathrm{int,R}}_{j+\frac{1}{2},k}}{\overline{\rho}^{\,\mathrm{int,R}}_{j+\frac{1}{2},k}},\qquad
\frac{1}{\overline{\Gamma}^{\mathrm{int,L}}_{j+\frac{1}{2},k}}\left(\overline{E}^{\mathrm{int,L}}_{j+\frac{1}{2},k}-\frac{\big((\overline{\rho u})^{\mathrm{int,L}}_{j+\frac{1}{2},k}\big)^2+\big((\overline{\rho v})^{\mathrm{int,L}}_{j+\frac{1}{2},k}\big)^2}{2\overline{\rho}^{\,\mathrm{int,L}}_{j+\frac{1}{2},k}}-\overline{\Pi}^{\mathrm{int,L}}_{j+\frac{1}{2},k}\right)\\
&\qquad=\frac{1}{\overline{\Gamma}^{\mathrm{int,R}}_{j+\frac{1}{2},k}}\left(\overline{E}^{\mathrm{int,R}}_{j+\frac{1}{2},k}-\frac{\big((\overline{\rho u})^{\mathrm{int,R}}_{j+\frac{1}{2},k}\big)^2+\big((\overline{\rho v})^{\mathrm{int,R}}_{j+\frac{1}{2},k}\big)^2}{2\overline{\rho}^{\,\mathrm{int,R}}_{j+\frac{1}{2},k}}-\overline{\Pi}^{\mathrm{int,R}}_{j+\frac{1}{2},k}\right),
\end{aligned}
$$

and then proceed as in §2.2.1 to enforce sharp (yet, non-oscillatory) jumps of the ρ-, ρv-, Γ-, and Π-components. This leads to the following formulae analogous to (2.31)–(2.32):

$$\overline{\rho}^{\,\mathrm{int,L}}_{j+\frac12,k}=\overline{\rho}^{\,\mathrm{int}}_{j+\frac12,k}+\frac{\delta^{\rho}_{j+\frac12,k}}{a^{\mathrm{int},-}_{j+\frac12,k}},\qquad \overline{\rho}^{\,\mathrm{int,R}}_{j+\frac12,k}=\overline{\rho}^{\,\mathrm{int}}_{j+\frac12,k}+\frac{\delta^{\rho}_{j+\frac12,k}}{a^{\mathrm{int},+}_{j+\frac12,k}},$$

$$(\overline{\rho v})^{\mathrm{int,L}}_{j+\frac12,k}=(\overline{\rho v})^{\mathrm{int}}_{j+\frac12,k}+\frac{\delta^{\rho v}_{j+\frac12,k}}{a^{\mathrm{int},-}_{j+\frac12,k}},\qquad (\overline{\rho v})^{\mathrm{int,R}}_{j+\frac12,k}=(\overline{\rho v})^{\mathrm{int}}_{j+\frac12,k}+\frac{\delta^{\rho v}_{j+\frac12,k}}{a^{\mathrm{int},+}_{j+\frac12,k}},$$

$$\overline{\Gamma}^{\mathrm{int,L}}_{j+\frac12,k}=\overline{\Gamma}^{\mathrm{int}}_{j+\frac12,k}+\frac{\delta^{\Gamma}_{j+\frac12,k}}{a^{\mathrm{int},-}_{j+\frac12,k}},\qquad \overline{\Gamma}^{\mathrm{int,R}}_{j+\frac12,k}=\overline{\Gamma}^{\mathrm{int}}_{j+\frac12,k}+\frac{\delta^{\Gamma}_{j+\frac12,k}}{a^{\mathrm{int},+}_{j+\frac12,k}},$$

$$\overline{\Pi}^{\mathrm{int,L}}_{j+\frac12,k}=\overline{\Pi}^{\mathrm{int}}_{j+\frac12,k}+\frac{\delta^{\Pi}_{j+\frac12,k}}{a^{\mathrm{int},-}_{j+\frac12,k}},\qquad \overline{\Pi}^{\mathrm{int,R}}_{j+\frac12,k}=\overline{\Pi}^{\mathrm{int}}_{j+\frac12,k}+\frac{\delta^{\Pi}_{j+\frac12,k}}{a^{\mathrm{int},+}_{j+\frac12,k}},$$

where

$$\delta^{\rho}_{j+\frac12,k}=\mathrm{minmod}\left(-a^{\mathrm{int},-}_{j+\frac12,k}\left[\overline{\rho}^{\mathrm{int}}_{j+\frac12,k}-\left(\rho^{\mathrm{int}}_{j+\frac12,k}\right)_{\ell}\right],\,a^{\mathrm{int},+}_{j+\frac12,k}\left[\left(\rho^{\mathrm{int}}_{j+\frac12,k}\right)_{r}-\overline{\rho}^{\mathrm{int}}_{j+\frac12,k}\right]\right),$$

$$\delta^{\rho v}_{j+\frac12,k}=\mathrm{minmod}\left(-a^{\mathrm{int},-}_{j+\frac12,k}\left[(\overline{\rho v})^{\mathrm{int}}_{j+\frac12,k}-\left((\rho v)^{\mathrm{int}}_{j+\frac12,k}\right)_{\ell}\right],\,a^{\mathrm{int},+}_{j+\frac12,k}\left[\left((\rho v)^{\mathrm{int}}_{j+\frac12,k}\right)_{r}-(\overline{\rho v})^{\mathrm{int}}_{j+\frac12,k}\right]\right),$$

$$\delta^{\Gamma}_{j+\frac12,k}=\mathrm{minmod}\left(-a^{\mathrm{int},-}_{j+\frac12,k}\left[\overline{\Gamma}^{\mathrm{int}}_{j+\frac12,k}-\left(\Gamma^{\mathrm{int}}_{j+\frac12,k}\right)_{\ell}\right],\,a^{\mathrm{int},+}_{j+\frac12,k}\left[\left(\Gamma^{\mathrm{int}}_{j+\frac12,k}\right)_{r}-\overline{\Gamma}^{\mathrm{int}}_{j+\frac12,k}\right]\right),$$

$$\delta^{\Pi}_{j+\frac12,k}=\mathrm{minmod}\left(-a^{\mathrm{int},-}_{j+\frac12,k}\left[\overline{\Pi}^{\mathrm{int}}_{j+\frac12,k}-\left(\Pi^{\mathrm{int}}_{j+\frac12,k}\right)_{\ell}\right],\,a^{\mathrm{int},+}_{j+\frac12,k}\left[\left(\Pi^{\mathrm{int}}_{j+\frac12,k}\right)_{r}-\overline{\Pi}^{\mathrm{int}}_{j+\frac12,k}\right]\right).$$

Here, the values $\left(\rho^{\mathrm{int}}_{j+\frac12,k}\right)_{\ell}$, $\left(\rho^{\mathrm{int}}_{j+\frac12,k}\right)_{r}$, $\left((\rho v)^{\mathrm{int}}_{j+\frac12,k}\right)_{\ell}$, $\left((\rho v)^{\mathrm{int}}_{j+\frac12,k}\right)_{r}$, $\left(\Gamma^{\mathrm{int}}_{j+\frac12,k}\right)_{\ell}$, $\left(\Gamma^{\mathrm{int}}_{j+\frac12,k}\right)_{r}$, $\left(\Pi^{\mathrm{int}}_{j+\frac12,k}\right)_{\ell}$, and $\left(\Pi^{\mathrm{int}}_{j+\frac12,k}\right)_{r}$, are obtained using the Taylor expansions as it was done in (2.33).

We then proceed as in the remaining part of §2.2.1 and complete the derivation of the fully discrete scheme (not shown here for the sake of brevity), and after this, we pass to the semi-discrete limit and end up with the LD PCCU flux (3.5) with the following "built-in" anti-diffusion term:

$$\boldsymbol{q}_{j+\frac12,k}=\alpha^{*}_{j+\frac12,k}\left(q^{\rho}_{j+\frac12,k},u^{*}_{j+\frac12,k}q^{\rho}_{j+\frac12,k},q^{\rho v}_{j+\frac12,k},q^{E}_{j+\frac12,k},q^{\Gamma}_{j+\frac12,k},q^{\Pi}_{j+\frac12,k}\right)^{\mathsf{T}}.$$

Here,

$$\boldsymbol{U}^{*}_{j+\frac12,k}=\frac{a^{+}_{j+\frac12,k}\boldsymbol{U}^{+}_{j+\frac12,k}-a^{-}_{j+\frac12,k}\boldsymbol{U}^{-}_{j+\frac12,k}-\left(\boldsymbol{K}^{+}_{j+\frac12,k}-\boldsymbol{K}^{-}_{j+\frac12,k}\right)}{a^{+}_{j+\frac12,k}-a^{-}_{j+\frac12,k}},\quad u^{*}_{j+\frac12,k}=\frac{(\rho u)^{*}_{j+\frac12,k}}{\rho^{*}_{j+\frac12,k}},$$

$$q^{\rho}_{j+\frac12,k}=\mathrm{minmod}\left(-a^{*,-}_{j+\frac12,k}\left(\rho^{*}_{j+\frac12,k}-\rho^{-}_{j+\frac12,k}\right),a^{*,+}_{j+\frac12,k}\left(\rho^{+}_{j+\frac12,k}-\rho^{*}_{j+\frac12,k}\right)\right),$$

$$q^{\rho v}_{j+\frac12,k}=\mathrm{minmod}\left(-a^{*,-}_{j+\frac12,k}\left((\rho v)^{*}_{j+\frac12,k}-(\rho v)^{-}_{j+\frac12,k}\right),a^{*,+}_{j+\frac12,k}\left((\rho v)^{+}_{j+\frac12,k}-(\rho v)^{*}_{j+\frac12,k}\right)\right),$$

$$q^{\Gamma}_{j+\frac12,k}=\mathrm{minmod}\left(-a^{*,-}_{j+\frac12,k}\left(\Gamma^{*}_{j+\frac12,k}-\Gamma^{-}_{j+\frac12,k}\right),a^{*,+}_{j+\frac12,k}\left(\Gamma^{+}_{j+\frac12,k}-\Gamma^{*}_{j+\frac12,k}\right)\right),$$

$$q^{\Pi}_{j+\frac12,k}=\mathrm{minmod}\left(-a^{*,-}_{j+\frac12,k}\left(\Pi^{*}_{j+\frac12,k}-\Pi^{-}_{j+\frac12,k}\right),a^{*,+}_{j+\frac12,k}\left(\Pi^{+}_{j+\frac12,k}-\Pi^{*}_{j+\frac12,k}\right)\right),$$

$$q^{E}_{j+\frac12,k}=-\frac{a^{*,+}_{j+\frac12,k}a^{*,-}_{j+\frac12,k}}{a^{+}_{j+\frac12,k}-a^{-}_{j+\frac12,k}}\left\{\frac{(d^{\Gamma})^{-}_{j+\frac12,k}\left((\rho v)^{*}_{j+\frac12,k}+\dfrac{q^{\rho v}_{j+\frac12,k}}{a^{*,+}_{j+\frac12,k}}\right)^{2}}{2\left(\rho^{*}_{j+\frac12,k}+\dfrac{q^{\rho}_{j+\frac12,k}}{a^{*,+}_{j+\frac12,k}}\right)}-\frac{(d^{\Gamma})^{+}_{j+\frac12,k}\left((\rho v)^{*}_{j+\frac12,k}+\dfrac{q^{\rho v}_{j+\frac12,k}}{a^{*,-}_{j+\frac12,k}}\right)^{2}}{2\left(\rho^{*}_{j+\frac12,k}+\dfrac{q^{\rho}_{j+\frac12,k}}{a^{*,-}_{j+\frac12,k}}\right)}\right\}$$

$$+\frac{\left(u^*_{j+\frac12,k}\right)^2}{2}q^\rho_{j+\frac12,k}+\frac{q^\Gamma_{j+\frac12,k}}{\Gamma^*_{j+\frac12,k}}\left[E^*_{j+\frac12,k}-\frac{\left((\rho u)^*_{j+\frac12,k}\right)^2}{2\rho^*_{j+\frac12,k}}-\Pi^*_{j+\frac12,k}\right]+q^\Pi_{j+\frac12,k},$$

$$a^{*,\pm}_{j+\frac12,k}=a^\pm_{j+\frac12,k}-u^*_{j+\frac12,k},\quad \alpha^*_{j+\frac12,k}=\begin{cases}\dfrac{a^+_{j+\frac12,k}}{a^{*,+}_{j+\frac12,k}} & \text{if } u^*_{j+\frac12,k}<0,\\ \dfrac{a^-_{j+\frac12,k}}{a^{*,-}_{j+\frac12,k}} & \text{otherwise,}\end{cases}$$

where

$$(d^\Gamma)^\pm_{j+\frac12,k}=1-\frac{q^\Gamma_{j+\frac12,k}}{a^{*,\pm}_{j+\frac12,k}\Gamma^*_{j+\frac12,k}}.$$

Similarly, the "built-in" anti-diffusion term in the LD PCCU flux (3.6) is

$$\boldsymbol{q}_{j,k+\frac12}=\alpha^*_{j,k+\frac12}\left(q^\rho_{j,k+\frac12},q^{\rho u}_{j,k+\frac12},v^*_{j,k+\frac12}q^\rho_{j,k+\frac12},q^E_{j,k+\frac12},q^\Gamma_{j,k+\frac12},q^\Pi_{j,k+\frac12}\right)^\top,$$

with

$$\boldsymbol{U}^*_{j,k+\frac12}=\frac{b^+_{j,k+\frac12}\boldsymbol{U}^+_{j,k+\frac12}-b^-_{j,k+\frac12}\boldsymbol{U}^-_{j,k+\frac12}-\left(\boldsymbol{L}^+_{j,k+\frac12}-\boldsymbol{L}^-_{j,k+\frac12}\right)}{b^+_{j,k+\frac12}-b^-_{j,k+\frac12}},\quad v^*_{j,k+\frac12}=\frac{(\rho v)^*_{j,k+\frac12}}{\rho^*_{j,k+\frac12}},$$

$$q^\rho_{j,k+\frac12}=\text{minmod}\left(-b^{*,-}_{j,k+\frac12}\left(\rho^*_{j,k+\frac12}-\rho^-_{j,k+\frac12}\right),b^{*,+}_{j,k+\frac12}\left(\rho^+_{j,k+\frac12}-\rho^*_{j,k+\frac12}\right)\right),$$

$$q^{\rho u}_{j,k+\frac12}=\text{minmod}\left(-b^{*,-}_{j,k+\frac12}\left((\rho u)^*_{j,k+\frac12}-(\rho u)^-_{j,k+\frac12}\right),b^{*,+}_{j,k+\frac12}\left((\rho u)^+_{j,k+\frac12}-(\rho u)^*_{j,k+\frac12}\right)\right),$$

$$q^\Gamma_{j,k+\frac12}=\text{minmod}\left(-b^{*,-}_{j,k+\frac12}\left(\Gamma^*_{j,k+\frac12}-\Gamma^-_{j,k+\frac12}\right),b^{*,+}_{j,k+\frac12}\left(\Gamma^+_{j,k+\frac12}-\Gamma^*_{j,k+\frac12}\right)\right),$$

$$q^\Pi_{j,k+\frac12}=\text{minmod}\left(-b^{*,-}_{j,k+\frac12}\left(\Pi^*_{j,k+\frac12}-\Pi^-_{j,k+\frac12}\right),b^{*,+}_{j,k+\frac12}\left(\Pi^+_{j,k+\frac12}-\Pi^*_{j,k+\frac12}\right)\right),$$

$$q^E_{j,k+\frac12}=-\frac{b^+_{j,k+\frac12}b^-_{j,k+\frac12}}{b^+_{j,k+\frac12}-b^-_{j,k+\frac12}}\left\{\frac{(d^\Gamma)^-_{j,k+\frac12}\left((\rho u)^*_{j,k+\frac12}+\dfrac{q^{\rho u}_{j,k+\frac12}}{b^{*,+}_{j,k+\frac12}}\right)^2}{2\left(\rho^*_{j,k+\frac12}+\dfrac{q^\rho_{j,k+\frac12}}{b^{*,+}_{j,k+\frac12}}\right)}-\frac{(d^\Gamma)^+_{j,k+\frac12}\left((\rho u)^*_{j,k+\frac12}+\dfrac{q^{\rho u}_{j,k+\frac12}}{b^{*,-}_{j,k+\frac12}}\right)^2}{2\left(\rho^*_{j,k+\frac12}+\dfrac{q^\rho_{j,k+\frac12}}{b^{*,-}_{j,k+\frac12}}\right)}\right\}$$

$$+\frac{\left(v^*_{j,k+\frac12}\right)^2}{2}q^\rho_{j,k+\frac12}+\frac{q^\Gamma_{j,k+\frac12}}{\Gamma^*_{j,k+\frac12}}\left[E^*_{j,k+\frac12}-\frac{\left((\rho v)^*_{j,k+\frac12}\right)^2}{2\rho^*_{j,k+\frac12}}-\Pi^*_{j,k+\frac12}\right]+q^\Pi_{j,k+\frac12},$$

$$b^{*,\pm}_{j,k+\frac12}=b^\pm_{j,k+\frac12}-v^*_{j,k+\frac12},\quad \alpha^*_{j,k+\frac12}=\begin{cases}\dfrac{b^+_{j,k+\frac12}}{b^{*,+}_{j,k+\frac12}} & \text{if } v^*_{j,k+\frac12}<0,\\ \dfrac{b^-_{j,k+\frac12}}{b^{*,-}_{j,k+\frac12}} & \text{otherwise,}\end{cases}$$

where

$$(d^\Gamma)^\pm_{j,k+\frac12}=1-\frac{q^\Gamma_{j,k+\frac12}}{b^{*,\pm}_{j,k+\frac12}\Gamma^*_{j,k+\frac12}}.$$

Remark 3.1. As in [14,32], the computation of numerical fluxes in (3.5) should be desingularized to avoid division by zero or very small numbers. First, if $a^+_{j+\frac12,k}<\varepsilon_0$ and $a^-_{j+\frac12,k}>-\varepsilon_0$ for a small positive ε_0, we replace the flux $\boldsymbol{\mathcal{K}}_{j+\frac12,k}$ with

$$\boldsymbol{\mathcal{K}}_{j+\frac12,k}=\frac{\boldsymbol{K}\big(\boldsymbol{U}^-_{j+\frac12,k}\big)+\boldsymbol{K}\big(\boldsymbol{U}^+_{j+\frac12,k}\big)}{2}.$$

Similarly, if $b^+_{j,k+\frac12}<\varepsilon_0$ and $b^-_{j,k+\frac12}>-\varepsilon_0$, we replace the flux $\boldsymbol{\mathcal{L}}_{j,k+\frac12}$ with

$$\boldsymbol{\mathcal{L}}_{j,k+\frac12}=\frac{\boldsymbol{L}\big(\boldsymbol{U}^-_{j,k+\frac12}\big)+\boldsymbol{L}\big(\boldsymbol{U}^+_{j,k+\frac12}\big)}{2}.$$

As in the 1-D case, we take $\varepsilon_0=10^{-12}$ in all of the numerical examples.

3.2. Flux globalization based LD ai-WENO PCCU scheme

In this section, we extend the 2-D second-order flux globalization based LD PCCU schemes from §3.1 to the fifth order of accuracy within the A-WENO framework.

The semi-discrete fifth-order LD Ai-WENO PCCU scheme for the 2-D quasi-conservative system (3.1)–(3.2) reads as

$$\frac{\mathrm{d}}{\mathrm{d}t}\boldsymbol{U}_{j,k}=-\frac{\boldsymbol{\mathcal{H}}^x_{j+\frac12,k}-\boldsymbol{\mathcal{H}}^x_{j-\frac12,k}}{\Delta x}-\frac{\boldsymbol{\mathcal{H}}^y_{j,k+\frac12}-\boldsymbol{\mathcal{H}}^y_{j,k-\frac12}}{\Delta y},\tag{3.14}$$

where the fifth-order numerical fluxes $\boldsymbol{\mathcal{H}}^x_{j+\frac12,k}$ and $\boldsymbol{\mathcal{H}}^y_{j,k+\frac12}$ are defined by

$$\begin{aligned}\boldsymbol{\mathcal{H}}^x_{j+\frac12,k}&=\boldsymbol{\mathcal{K}}_{j+\frac12,k}-\frac{(\Delta x)^2}{24}(\boldsymbol{K}_{xx})_{j+\frac12,k}+\frac{7(\Delta x)^4}{5760}(\boldsymbol{K}_{xxxx})_{j+\frac12,k},\\ \boldsymbol{\mathcal{H}}^y_{j,k+\frac12}&=\boldsymbol{\mathcal{L}}_{j,k+\frac12}-\frac{(\Delta y)^2}{24}(\boldsymbol{L}_{yy})_{j,k+\frac12}+\frac{7(\Delta y)^4}{5760}(\boldsymbol{L}_{yyyy})_{j,k+\frac12}.\end{aligned}\tag{3.15}$$

Here, $\boldsymbol{\mathcal{K}}_{j+\frac12,k}$ and $\boldsymbol{\mathcal{L}}_{j,k+\frac12}$ are the finite-volume fluxes (3.5), and $(\boldsymbol{K}_{xx})_{j+\frac12,k}$, $(\boldsymbol{K}_{xxxx})_{j+\frac12,k}$, $(\boldsymbol{L}_{yy})_{j,k+\frac12}$, and $(\boldsymbol{L}_{yyyy})_{j,k+\frac12}$ are approximations of the second- and fourth-order spatial derivatives of $\boldsymbol{K}$ at $(x,y)=(x_{j+\frac12},y_k)$ and $\boldsymbol{L}$ at $(x,y)=(x_j,y_{k+\frac12})$, respectively. We compute these quantities using the finite-difference approximations analogous to (2.54):

$$\begin{aligned}(\boldsymbol{K}_{xx})_{j+\frac12,k}&=\frac{1}{12(\Delta x)^2}\left[-\boldsymbol{\mathcal{K}}_{j-\frac32,k}+16\boldsymbol{\mathcal{K}}_{j-\frac12,k}-30\boldsymbol{\mathcal{K}}_{j+\frac12,k}+16\boldsymbol{\mathcal{K}}_{j+\frac32,k}-\boldsymbol{\mathcal{K}}_{j+\frac52,k}\right],\\ (\boldsymbol{K}_{xxxx})_{j+\frac12,k}&=\frac{1}{(\Delta x)^4}\left[\boldsymbol{\mathcal{K}}_{j-\frac32,k}-4\boldsymbol{\mathcal{K}}_{j-\frac12,k}+6\boldsymbol{\mathcal{K}}_{j+\frac12,k}-4\boldsymbol{\mathcal{K}}_{j+\frac32,k}+\boldsymbol{\mathcal{K}}_{j+\frac52,k}\right],\\ (\boldsymbol{L}_{yy})_{j,k+\frac12}&=\frac{1}{12(\Delta y)^2}\left[-\boldsymbol{\mathcal{L}}_{j,k-\frac32}+16\boldsymbol{\mathcal{L}}_{j,k-\frac12}-30\boldsymbol{\mathcal{L}}_{j,k+\frac12}+16\boldsymbol{\mathcal{L}}_{j,k+\frac32}-\boldsymbol{\mathcal{L}}_{j,k+\frac52}\right],\\ (\boldsymbol{L}_{yyyy})_{j,k+\frac12}&=\frac{1}{(\Delta y)^4}\left[\boldsymbol{\mathcal{L}}_{j,k-\frac32}-4\boldsymbol{\mathcal{L}}_{j,k-\frac12}+6\boldsymbol{\mathcal{L}}_{j,k+\frac12}-4\boldsymbol{\mathcal{L}}_{j,k+\frac32}+\boldsymbol{\mathcal{L}}_{j,k+\frac52}\right].\end{aligned}$$

As in the 1-D case, the resulting semi-discrete scheme (3.14)–(3.15) is fifth-order accurate provided the point values $\boldsymbol{U}^\pm_{j+\frac12,k}$ and $\boldsymbol{U}^\pm_{j,k+\frac12}$ are calculated using a fifth-order interpolation. To this end, we apply the recently proposed fifth-order Ai-WENO-Z interpolation [17,34,50], which can be performed in the x- and y-directions similarly to the 1-D case discussed in Appendix A; we omit the details for the sake of brevity.

Remark 3.2. As in the 1-D case, one needs to apply the Ai-WENO-Z interpolation procedure in the local characteristic variables to reduce the magnitude of the numerical oscillations. In Appendix B, we provide a detailed explanation on how to apply the LCD to the 2-D system (3.1)–(3.3).

4. Numerical examples

In this section, we apply the developed schemes to several 1-D and 2-D numerical examples and compare the performance of the second-order flux globalization based PCCU, the second-order flux globalization based LD PCCU, and the fifth-order flux globalization based LD Ai-WENO PCCU schemes, which will be referred to as the *PCCU*, *LD PCCU*, and *LD Ai-WENO* schemes, respectively.

In all of the numerical examples, we have solved the ODE systems (2.2), (2.52), (3.4), and (3.14) using the three-stage third-order strong stability preserving (SSP) Runge-Kutta method (see, e.g., [19,20]) and used the CFL number 0.45.

Table 4.1
Example 1: The L^1-errors and experimental convergence rates for the density ρ.

Δx	PCCU		LD PCCU		LD Ai-WENO	
	Error	Rate	Error	Rate	Error	Rate
1/40	9.13e-3	1.49	4.03e-3	1.80	7.77e-7	5.02
1/80	1.39e-3	1.99	8.19e-4	2.01	2.41e-8	5.02
1/160	2.92e-4	2.10	1.84e-4	2.07	7.52e-10	5.01
1/320	5.99e-5	2.18	4.12e-5	2.11	2.34e-11	5.01
1/640	1.26e-5	2.21	9.26e-6	2.13	7.30e-13	5.00

4.1. One-dimensional examples

Example 1—1-D accuracy test

In the first example taken from [49], we consider the following smooth initial data:

$$(\rho,u,p;\gamma,\pi_\infty)\Big|_{(x,0)}=\Big(1+\frac{2}{5}\cos(\pi x),1,1;\frac{25}{12}+\frac{1}{3}\sin(\pi x),10-8\sin(\pi x)\Big).$$

We implement the periodic boundary conditions on the computational domain $[-1,1]$ and compute the numerical solution until the final time $t=1$ using the PCCU, LD PCCU, and LD Ai-WENO schemes on a sequence of seven uniform meshes with $\Delta x=1/(10\cdot 2^{\ell})$, $\ell=0,\ldots,6$.

We compute the L^1-errors in density and estimate the experimental convergence rates using the following Runge formulae, which are based on the solutions computed on the three consecutive uniform grids with the mesh sizes Δx, $2\Delta x$, and $4\Delta x$ and denoted by $(\cdot)^{\Delta x}$, $(\cdot)^{2\Delta x}$, and $(\cdot)^{4\Delta x}$, respectively:

$$\text{Error}(\Delta x)\approx\frac{\delta_{12}^2}{|\delta_{12}-\delta_{24}|},\quad \text{Rate}(\Delta x)\approx\log_2\left(\frac{\delta_{24}}{\delta_{12}}\right).$$

Here, $\delta_{12}:=\|(\cdot)^{\Delta x}-(\cdot)^{2\Delta x}\|_{L^1}$ and $\delta_{24}:=\|(\cdot)^{2\Delta x}-(\cdot)^{4\Delta x}\|_{L^1}$. The obtained results for the density are reported in Table 4.1, where one can clearly see that the second order of accuracy is achieved for the PCCU and LD PCCU schemes, and the fifth order of accuracy is achieved for the LD Ai-WENO scheme. Note that in order to achieve the fifth order of accuracy, we had to use smaller time steps with $\Delta t\sim(\Delta x)^{\frac{5}{3}}$.

Example 2—"Shock-Bubble" interaction

In the first example, we consider the "shock-bubble" interaction problem, which is a two-fluid modification of a single-fluid example from [32]. The initial data are given by

$$(\rho,u,p;\gamma,\pi_\infty)\Big|_{(x,0)}=\begin{cases}(13.1538,0,1;5/3,0), & |x|<0.25,\\ (1.3333,-0.3535,1.5;1.4,0), & x>0.75,\\ (1,0,1;1.4,0), & \text{otherwise},\end{cases}$$

which correspond to a left-moving shock, initially located at $x=0.75$, and a resting "bubble" with a radius of 0.25, initially located at the origin. These inital data are considered in the computational domain $[-1,2]$ subject to the solid wall boundary conditions imposed at both $x=-1$ and $x=2$.

We apply the studied PCCU, LD PCCU, and LD Ai-WENO schemes to this initial-boundary value problem and compute its numerical solutions until the final time $t=3$ on a uniform mesh with $\Delta x=1/100$. The obtained ρ, u, Γ, and Π are presented in Figs. 4.1—4.3 together with the reference solution computed by the PCCU scheme on a much finer mesh with $\Delta x=1/2000$. As one can see, the LD PCCU scheme achieves sharper resolution than the PCCU one, and the use of a fifth-order LD Ai-WENO scheme further enhances the resolution. One can also observe small oscillations in the PCCU and LD PCCU solutions (see Fig. 4.1 (left)), while the LD Ai-WENO solution is oscillatory-free in this example.

We then perform a more thorough comparison between the PCCU, LD PCCU, and LD Ai-WENO schemes by taking into account additional computational cost of the higher-order LD Ai-WENO scheme. To this end, we measure the CPU time consumed by the LD Ai-WENO scheme and refine the meshes used by the corresponding PCCU and LD PCCU schemes so that exactly the same CPU times are consumed by these two schemes to compute the numerical solutions (the sizes of the corresponding uniform grids are $\Delta x=1/180$ and $1/190$ for the PCCU and LD PCCU schemes, respectively). The obtained ρ (zoom at $x\in[-0.55,-0.4]$) and u (zoom at $x\in[-0.2,0.9]$) are shown in Fig. 4.4, where one can clearly see that in this example, the LD PCCU scheme outperforms its PCCU and LD Ai-WENO counterparts.

Example 3—water-air "Shock-Bubble" interaction

In the second 1-D example, which is a 1-D modification of an example from [8], we consider a gas-liquid multifluid system, where the liquid component is modeled by the EOS (2.9) with $\pi_\infty\gg 1$. The initial conditions,

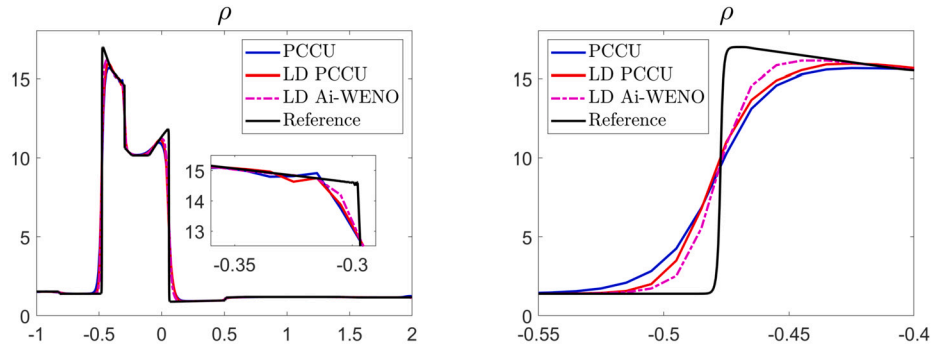

Fig. 4.1. Example 2: Density ρ (left) and zoom at $x \in [-0.55, -0.4]$ (right) . (For interpretation of the colors in the figure(s), the reader is referred to the web version of this article.)

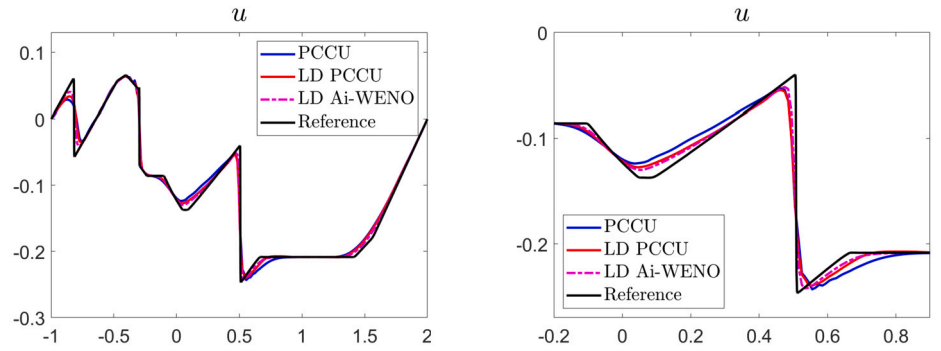

Fig. 4.2. Example 2: Velocity u (left) and zoom at $x \in [-0.2, 0.9]$ (right).

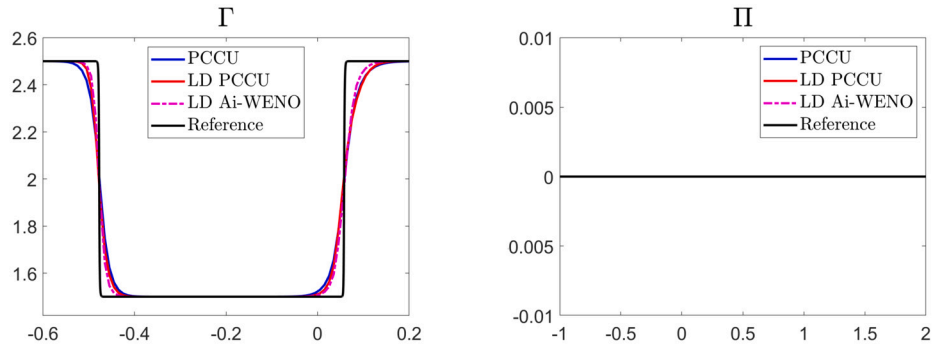

Fig. 4.3. Example 2: Γ zoomed at $x \in [-0.6, 0.2]$ (left) and Π (right).

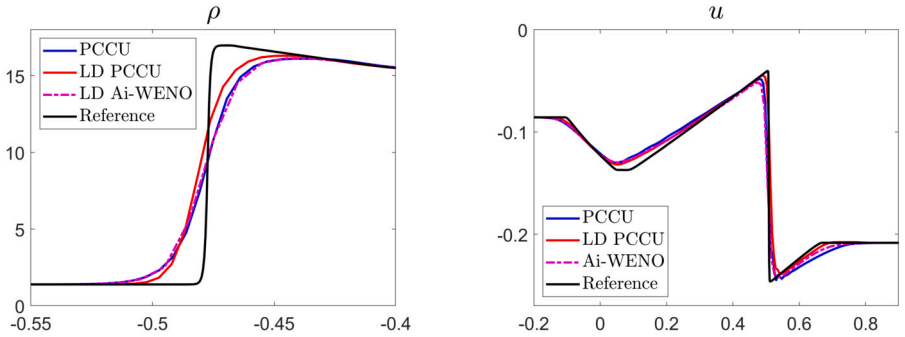

Fig. 4.4. Example 2: Density ρ zoom at $x \in [-0.55, -0.4]$ (left) and velocity u zoom at $x \in [-0.2, 0.9]$ (right) computed by the PCCU scheme with $\Delta x = 1/180$, LD PCCU scheme with $\Delta x = 1/190$, and LD Ai-WENO scheme with $\Delta x = 1/100$.

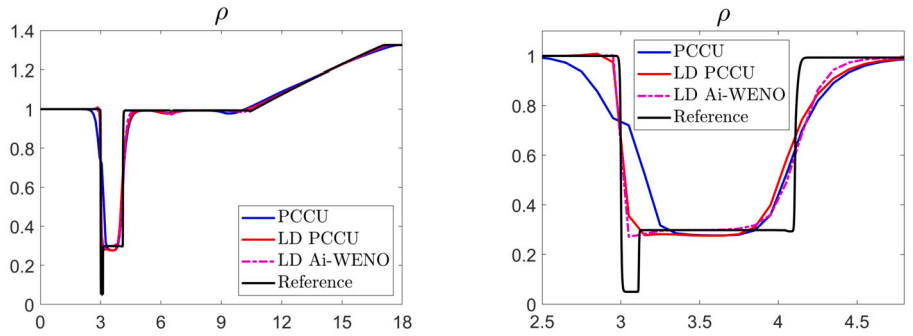

Fig. 4.5. Example 3: Density ρ (left) and zoom at $x \in [2.5, 4.8]$ (right).

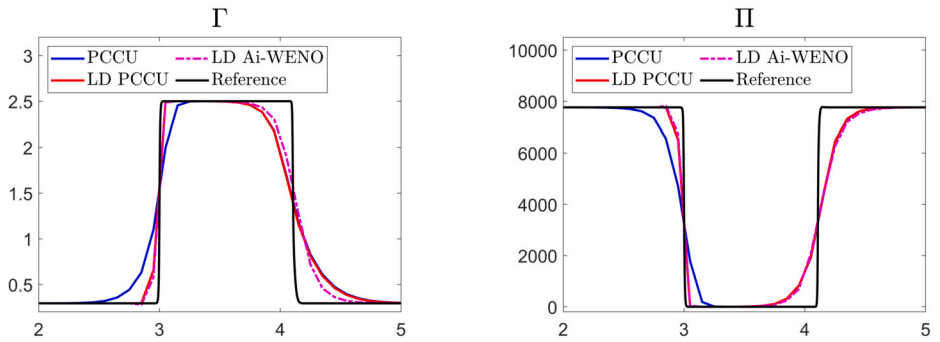

Fig. 4.6. Example 3: Γ (left) and Π (right) zoomed at $x \in [2, 5]$.

$$(\rho, u, p; \gamma, \pi_\infty)\big|_{(x,0)} = \begin{cases} (0.05, 0, 1; 1.4, 0), & |x-6| < 3, \\ (1.325, -68.525, 19153; 4.4, 6000), & x > 11.4, \\ (1, 0, 1; 4.4, 6000), & \text{otherwise}, \end{cases}$$

correspond to the left-moving shock, initially located at $x = 11.4$, and a resting air "bubble" with a radius 3, initially located at $x = 6$. The initial conditions are prescribed in the computational domain $[0, 18]$ subject to the free boundary conditions.

We compute the numerical solution until the final time $t = 0.045$ on a uniform mesh with $\Delta x = 1/10$ by the PCCU, LD PCCU, and LD Ai-WENO schemes and plot the obtained ρ, Γ, and Π in Figs. 4.5 and 4.6 together with the reference solution computed by the PCCU scheme on a much finer mesh with $\Delta x = 1/400$. As one can observe, the LD PCCU solution achieves sharper resolution (especially of the contact wave located at about $x = 3$) compared with its PCCU counterpart, and the LD Ai-WENO scheme achieves even higher resolution.

Example 4—water-air model with a very stiff equation of state

In the last 1-D example taken from [2,10], we consider another gas-liquid multifluid system with the water component modeled using even stiffer EOS than the one used in Example 2. The initial conditions that correspond to a severe water-air shock tube problem,

$$(\rho, u, p; \gamma, \pi_\infty)\big|_{(x,0)} = \begin{cases} (1000, 0, 10^9; 4.4, 6 \cdot 10^8), & x < 0.7, \\ (50, 0, 10^5; 1.4, 0), & x > 0.7, \end{cases}$$

are prescribed in the computational domain $[0, 1]$ subject to the free boundary conditions.

We compute the numerical solutions by the studied PCCU, LD PCCU, and LD Ai-WENO schemes until the final time $t = 0.00025$ on a uniform mesh with $\Delta x = 1/400$. The obtained ρ, Γ, and Π are shown in Figs. 4.7 and 4.8 along with the reference solution computed by the PCCU scheme on a much finer mesh with $\Delta x = 1/6400$. One can observe that all of the studied schemes produce non-oscillatory numerical solutions, and the LD Ai-WENO solution is slightly sharper than the solutions computed by the PCCU and LD PCCU schemes.

4.2. Two-dimensional examples

In this section, we present four 2-D numerical examples. In all of them, we plot the Schlieren images of the magnitude of the density gradient field, $|\nabla\rho|$. To this end, we have used the following shading function:

$$\exp\left(-\frac{80|\nabla\rho|}{\max(|\nabla\rho|)}\right),$$

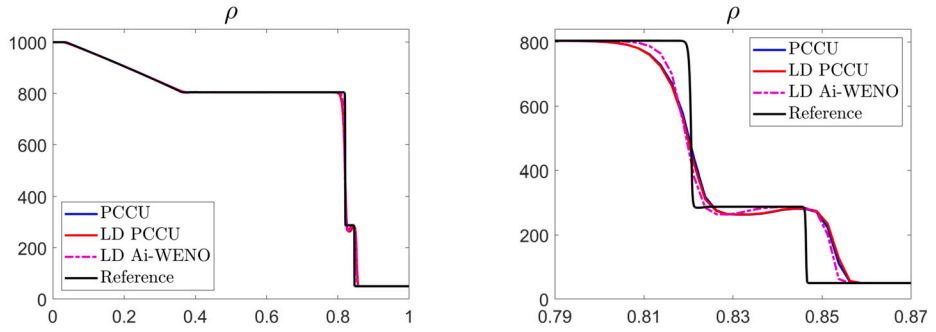

Fig. 4.7. Example 4: Density ρ (left) and zoom at $[0.79, 0.87]$ (right).

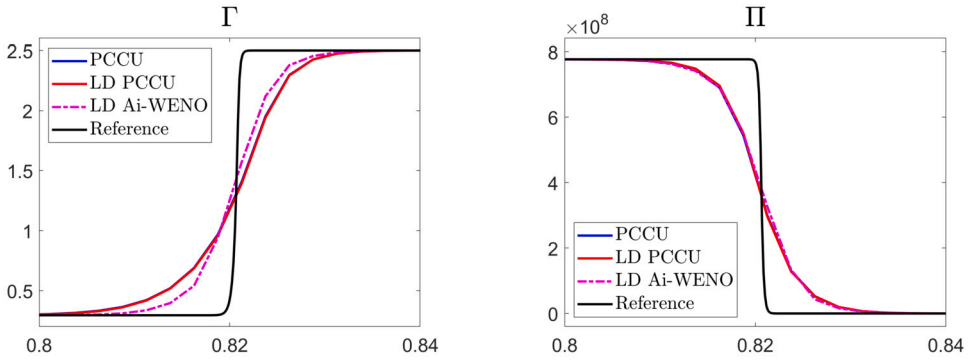

Fig. 4.8. Example 4: γ (left) and Π (right) zoomed at $x \in [0.8, 0.84]$.

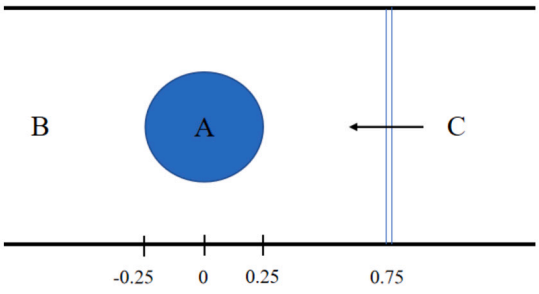

Fig. 4.9. Initial setting for the 2-D numerical examples.

where the numerical derivatives of the density are computed using standard central differencing.

Example 5—shock-helium bubble interaction

In the first 2-D example taken from [10,43], a shock wave in the air hits the light resting bubble which contains helium. We take the following initial conditions:

$$(\rho, u, v, p; \gamma, p_\infty)\Big|_{(x,y,0)} = \begin{cases} (4/29, 0, 0, 1; 5/3, 0), & \text{in region A,} \\ (1, 0, 0, 1; 1.4, 0), & \text{in region B,} \\ (4/3, -0.3535, 0, 1.5; 1.4, 0), & \text{in region C,} \end{cases}$$

where regions A, B, and C are outlined in Fig. 4.9, and the computational domain is $[-3, 1] \times [-0.5, 0.5]$. We impose the solid wall boundary conditions on the top and bottom and the free boundary conditions on the left and right edges of the computational domain.

We compute the numerical solutions until the final time $t = 3$ on a uniform mesh with $\Delta x = \Delta y = 1/500$. In Figs. 4.10 and 4.11, we present different stages of the shock-bubble interaction computed by the PCCU, LD PCCU, and LD Ai-WENO schemes. Notice that the bubble changes its shape and propagates to the left, but in order to focus on the details of the bubble structure, we only zoom at $[\sigma, \sigma + 1] \times [-0.5, 0.5]$ square area containing the bubble (σ is decreasing in time from -0.5 to -1.6). As one can observe from the numerical results, the bubble interface develops very complex structures after the bubble is hit by the shock, especially at large times.

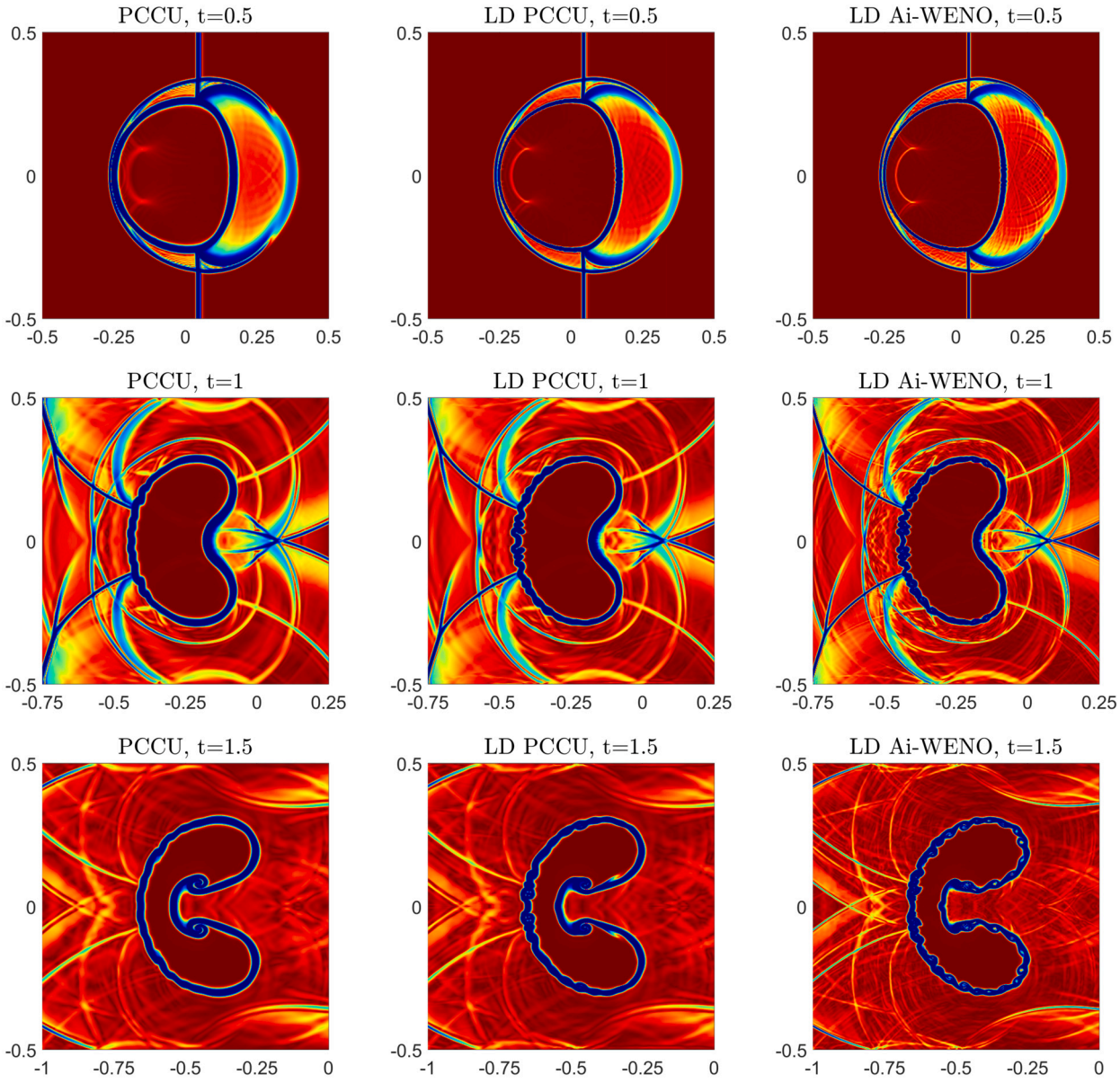

Fig. 4.10. Example 5: Shock-helium bubble interaction by the PCCU (left column), LD PCCU (middle column), and LD Ai-WENO (right column) schemes at times $t = 0.5$, 1, and 1.5.

The obtained results are in a good agreement with the experimental findings presented in [21] and the numerical results reported in [9,10,43]. At the same time, one can see that at a small time $t = 0.5$, the resolution of the bubble interface is significantly improved by the use of the LD PCCU and especially the LD Ai-WENO schemes. At larger times, the interface develops instabilities, which are smeared by a more dissipative PCCU scheme. The differences in the achieved resolution of the small solution structures become even more pronounced at the larger times $t = 2$, 2.5, and especially at $t = 3$. This clearly indicates that the LD PCCU scheme outperforms the PCCU one, and the further improvement in the LD Ai-WENO results is much more obvious than in the 1-D examples.

We also perform a more thorough comparison between the PCCU, LD PCCU, and LD Ai-WENO schemes by taking into account additional computational cost of the LD Ai-WENO scheme. As in Example 2, we measure the CPU time consumed by the LD Ai-WENO scheme and refine the meshes used by the PCCU and LD PCCU schemes so that exactly the same CPU times are consumed by these two schemes to compute the numerical solutions (the sizes of the corresponding uniform grids are $\Delta x = \Delta y = 1/600$ and $1/590$ for the PCCU and LD PCCU schemes, respectively). The obtained numerical results are shown in Figs. 4.12 and 4.13, where one can see that in this example (unlike the 1-D Example 2), the LD Ai-WENO scheme achieves higher resolution than the LD PCCU scheme, while they both clearly outperform the PCCU scheme.

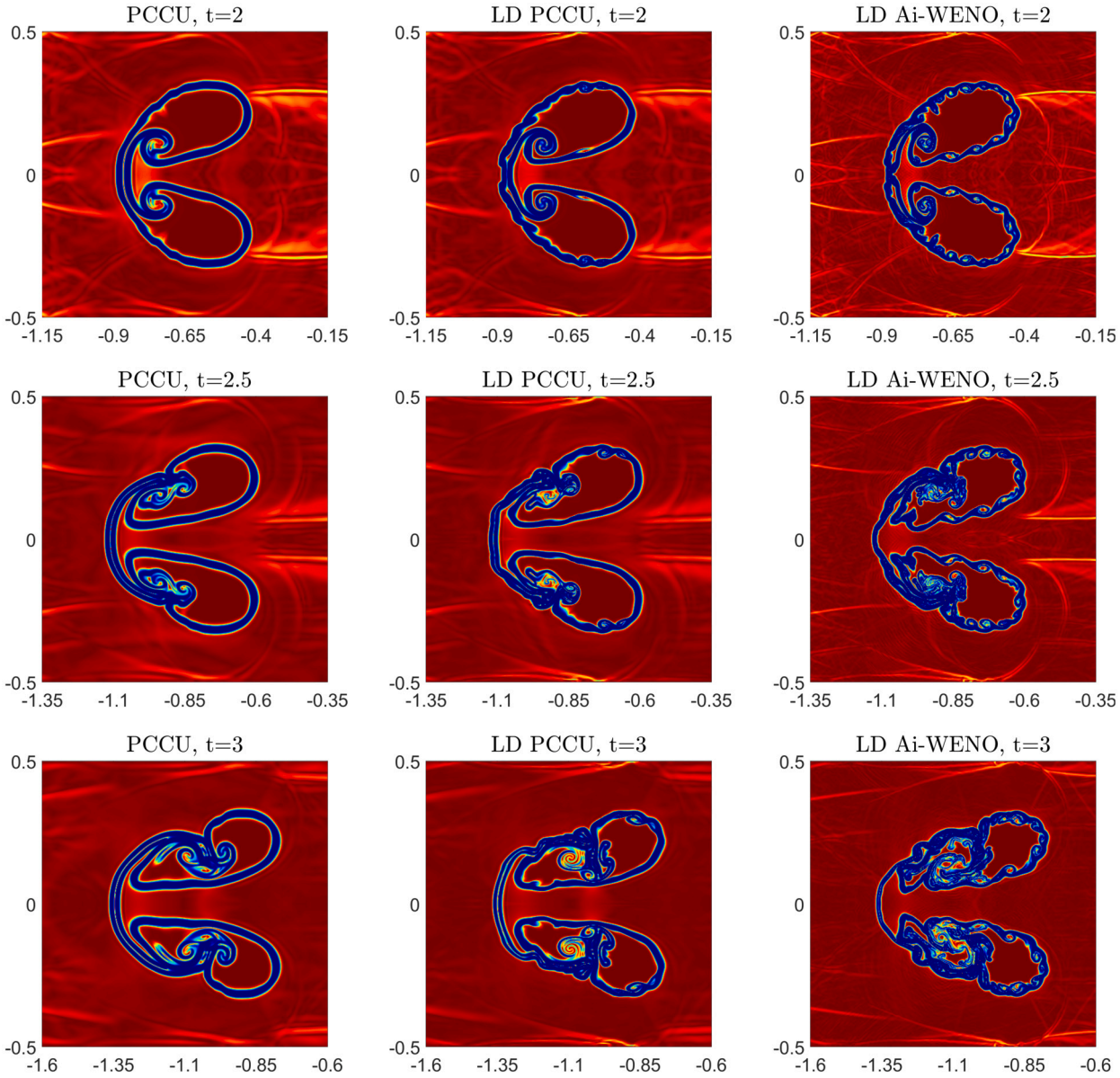

Fig. 4.11. Same as in Fig. 4.10, but at larger times $t = 2$, 2.5, and 3.

Example 6—shock-R22 bubble interaction

In the second 2-D example also taken from [10,43], a shock wave in the air hits the heavy resting bubble which contains R22. The initial conditions are

$$(\rho,u,v,p;\gamma,\pi_\infty)\Big|_{(x,y,0)}=\begin{cases}(3.1538,0,0,1;1.249,0), & \text{in region A},\\ (1,0,0,1;1.4,0), & \text{in region B},\\ (4/3,-0.3535,0,1.5;1.4,0), & \text{in region C}.\end{cases}$$

The regions A, B, and C are the same as in Example 5 and they are specified in Fig. 4.11. In this example, we impose the same boundary conditions and use the same computational domain as in Example 5.

We compute the numerical solutions until the final time $t = 3$ on a uniform mesh with $\Delta x = \Delta y = 1/500$. In Figs. 4.14 and 4.15, we present different stages of the shock-bubble interaction computed by the PCCU, LD PCCU, and LD Ai-WENO schemes. As one can see, the bubble changes its shape and propagates to the left, and in order to focus on the details of the bubble structure, we only zoom at $[\sigma,\sigma+1]\times[-0.5,0.5]$ square area containing the bubble (σ is decreasing in time from -0.5 to -1.15). Compared with Example 5, the bubble moves to the left a little slower and develops totally different structures as the R22 is heavier than the Helium. The obtained results are in a good agreement with the numerical results reported in [9,10,43]. Similar to Example 5, at a small time

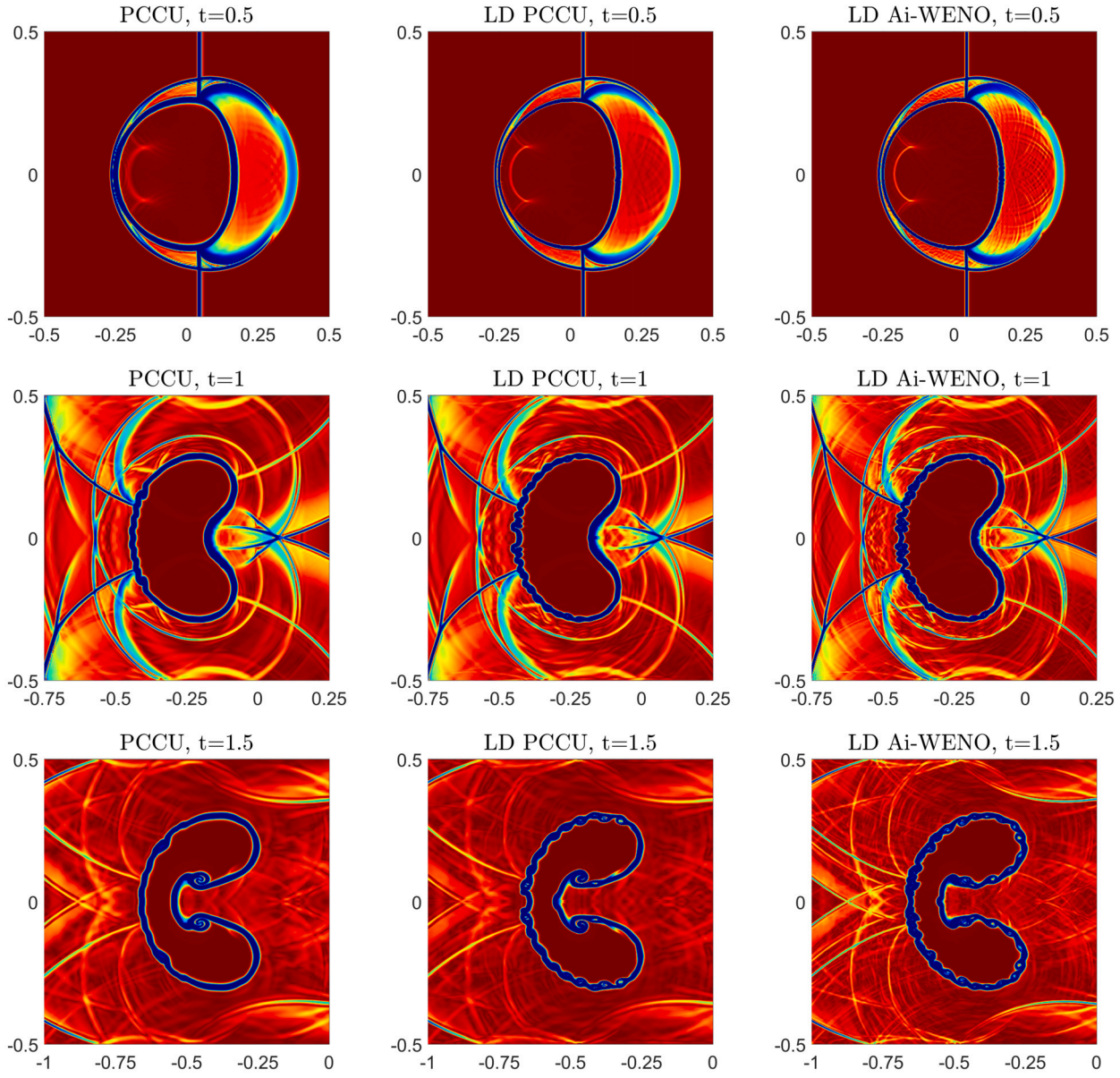

Fig. 4.12. Example 5: Shock-helium bubble interaction by the PCCU scheme with $\Delta x = \Delta y = 1/600$ (left column), LD PCCU scheme with $\Delta x = \Delta y = 1/590$ (middle column), and LD Ai-WENO scheme with $\Delta x = \Delta y = 1/500$ (right column) at times $t = 0.5$, 1, and 1.5.

$t = 0.5$, the resolution of the bubble interface is significantly improved by the use of either the LD PCCU or LD Ai-WENO schemes, and the improvement in this example is even more pronounced. By the time $t = 1$, the interface develop instabilities which are smeared by a more dissipative PCCU scheme. As time progresses, the solutions develop very complex small structures, which are better resolved by the schemes containing smaller amount of numerical dissipation, namely, by the LD PCCU and LD Ai-WENO schemes.

Example 7—a cylindrical explosion problem

In this 2-D example, which is a modification of an example from [56], we consider the case where a cylindrical explosive source is located between an air-water interface and an impermeable wall. The initial conditions are given by

$$(\rho, u, v, p; \gamma, \pi_\infty)\Big|_{(x,y,0)} = \begin{cases} (1.27, 0, 0, 8290; 2, 0), & (x-5)^2 + (y-2)^2 < 1, \\ (0.02, 0, 0, 1; 1.4, 0), & y > 4, \\ (1, 0, 0, 1; 7.15, 3309), & \text{otherwise}, \end{cases}$$

the solid wall boundary conditions are imposed at the bottom, and the free boundary conditions are prescribed on the other sides of the computational domain $[0, 10] \times [0, 6]$.

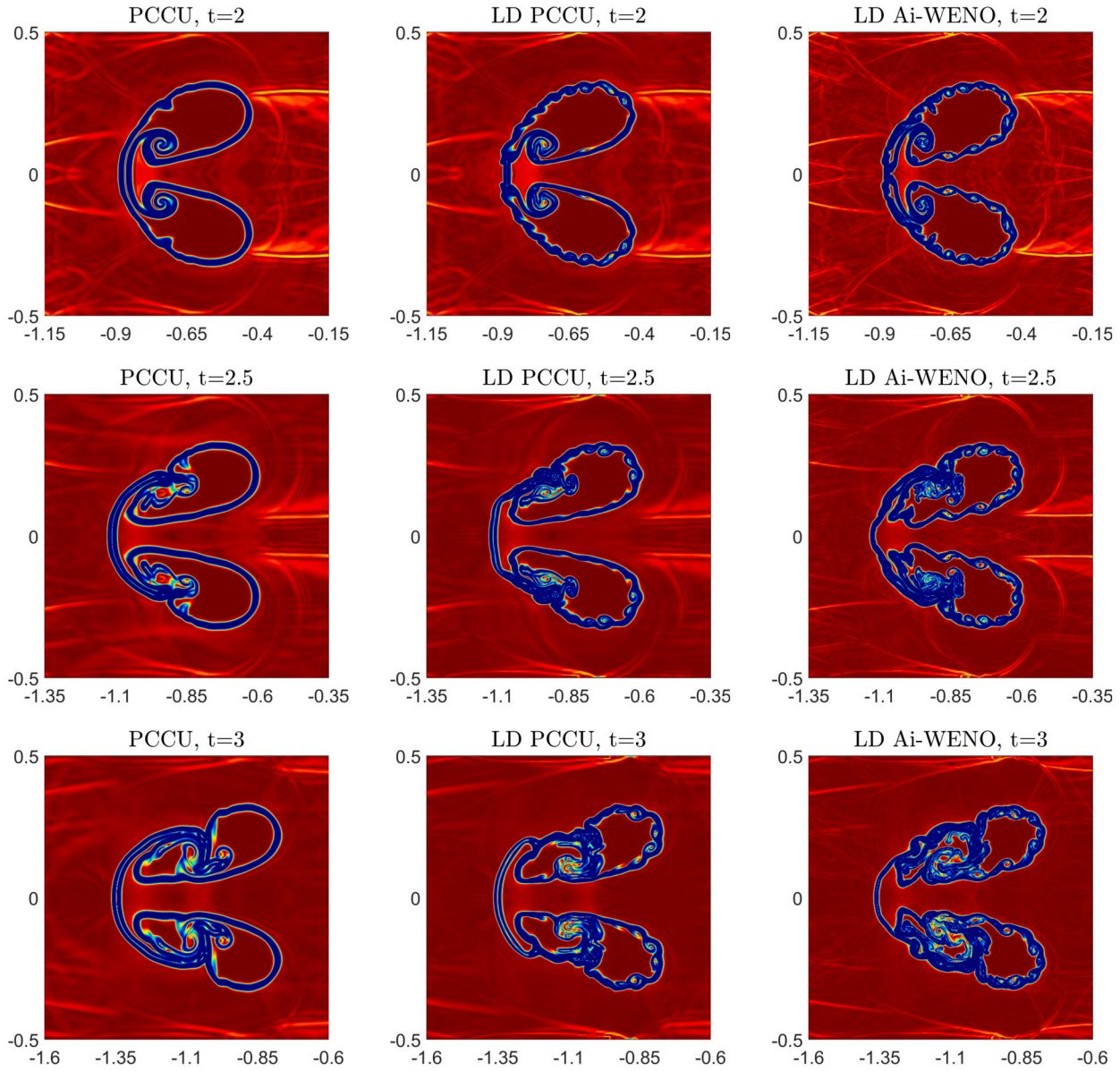

Fig. 4.13. Same as in Fig. 4.12, but at larger times $t = 2$, 2.5, and 3.

Notice that the initial conditions contain three—not two—different fluids, and therefore we need to modify the way the fluid interfaces are detected as the criteria (3.8) and (3.11) are applicable in the two-fluid case only. We first set $\Gamma_{\rm I} = 1/(\gamma_{\rm I} - 1)$, $\Gamma_{\rm II} = 1/(\gamma_{\rm II} - 1)$, and $\Gamma_{III} = 1/(\gamma_{\rm III} - 1)$, where $\gamma_{\rm I} = 2$, $\gamma_{\rm II} = 1.4$, and $\gamma_{\rm III} = 7.15$ are the specific heat ratios for the three fluids. We then introduce $\widehat{\Gamma}_1 := (\Gamma_{\rm I} + \Gamma_{\rm III})/2$, $\widehat{\Gamma}_2 := (\Gamma_{\rm II} + \Gamma_{\rm III})/2$, and replace the conditions (3.8) and (3.11) with

$$(\overline{\Gamma}_{j,k} - \widehat{\Gamma}_1)(\overline{\Gamma}_{j+1,k} - \widehat{\Gamma}_1) < 0 \quad \text{or} \quad (\overline{\Gamma}_{j,k} - \widehat{\Gamma}_2)(\overline{\Gamma}_{j+1,k} - \widehat{\Gamma}_2) < 0$$

and

$$(\overline{\Gamma}_{j,k} - \widehat{\Gamma}_1)(\overline{\Gamma}_{j,k+1} - \widehat{\Gamma}_1) < 0 \quad \text{or} \quad (\overline{\Gamma}_{j,k} - \widehat{\Gamma}_2)(\overline{\Gamma}_{j,k+1} - \widehat{\Gamma}_2) < 0$$

respectively.

We compute the numerical solutions until the final time $t = 0.02$ on a uniform mesh with $\Delta x = \Delta y = 1/80$ by the studied PCCU, LD PCCU, and LD Ai-WENO schemes. In Fig. 4.16, we present time snapshots of the obtained results, which qualitatively look very similar to the numerical results reported in [56]. As one can see, the LD PCCU scheme captures both the material interfaces and many of the developed wave structures substantially sharper than the PCCU scheme and the use of the LD Ai-WENO scheme further enhances the resolution. In particular, one can observe more pronounced small structures in the LD Ai-WENO solution (especially

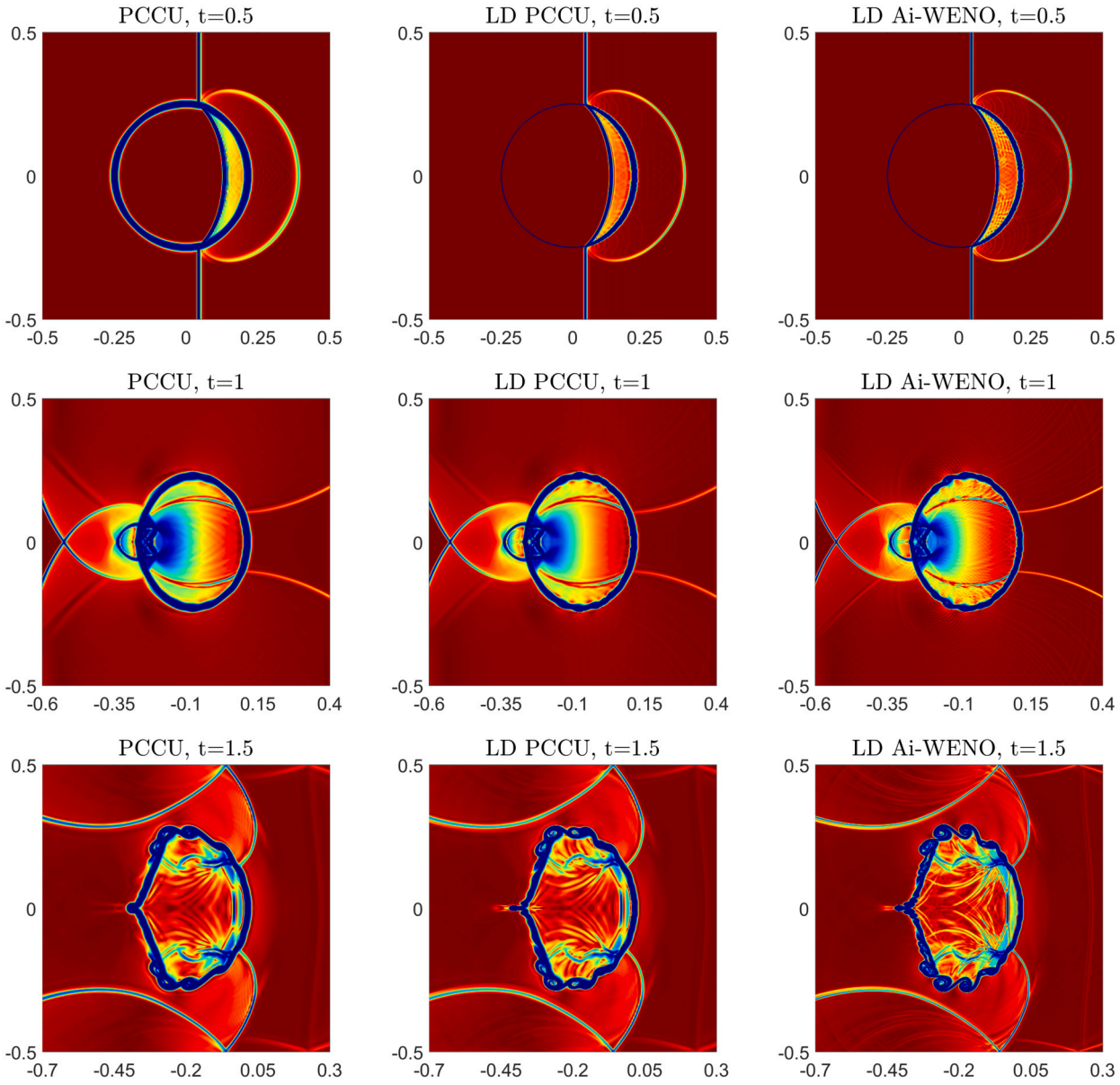

Fig. 4.14. Example 6: Shock-R22 bubble interaction by the PCCU (left column), LD PCCU (middle column), and LD Ai-WENO (right column) schemes at times $t = 0.5$, 1, and 1.5.

inside the bubble) at the large time $t = 0.02$; see Fig. 4.17, where we zoom at the bubble area. This example, once again, clearly indicates that the LD PCCU and LD Ai-WENO schemes outperform the PCCU one.

Example 8—water-air shock-bubble interaction

In the last 2-D example, which is taken from [8], we consider the interaction of a shock in water with a gas bubble. The initial conditions

$$(\rho,u,v,p;\gamma,\pi_\infty)\Big|_{(x,y,0)}=\begin{cases}(0.0012,0,0,1;1.4,0), & (x-6)^2+(y-6)^2<9,\\ (1.325,-68.525,0,19153;4.4,6000), & x>11.4,\\ (1,0,0,1;4.4,6000), & \text{otherwise},\end{cases}$$

correspond to a cylindrical air bubble impacted by a Mach 1.72 shock initiated in water. In this example, the initial data is prescribed in the computational domain $[0,12]\times[0,12]$ with the solid wall boundary conditions imposed on the top and bottom and the free boundary conditions on the left and right edges of the computational domain.

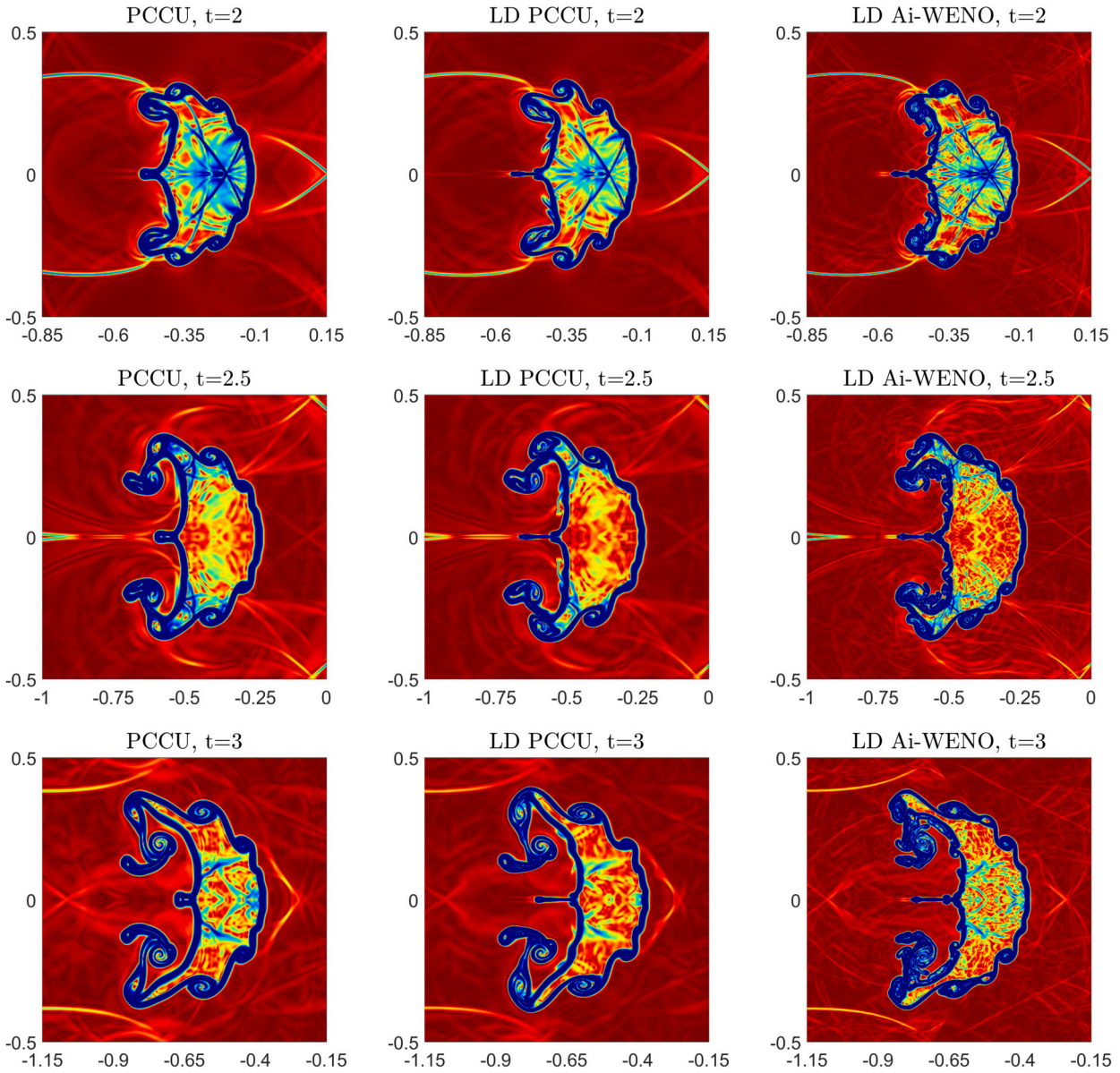

Fig. 4.15. Same as in Fig. 4.14, but at larger times $t = 2$, 2.5, and 3.

We compute the numerical solutions by the studied PCCU, LD PCCU, and LD Ai-WENO schemes until the final time $t = 0.045$ on a uniform mesh with $\Delta x = \Delta y = 3/200$. In Figs. 4.18 and 4.19, we present different stages of the interaction process. As one can see, the bubble containing air will be compressed by the water, propagates to the left, and changes its shape until losing its integrity and breaking up. The obtained results are in a good qualitative agreement with the numerical results reported in [8]. As in the previous examples, the resolution of the bubble interface is significantly improved by the use of the LD PCCU and LD Ai-WENO schemes, especially for the small times $t = 0.0204$, 0.0305, and 0.0368; see Fig. 4.18. At the same time, the differences near the bubble interfaces between the LD PCCU and LD Ai-WENO solutions are minor.

Remark 4.1. In order to preserve the positivity of the pressure computed by the LD Ai-WENO scheme, we have used the following algorithm. We first detect the material interfaces by (3.8) and (3.11) and then switch to the second-order LD PCCU scheme (with the one-sided point values computed by the SBM limiter (2.15), (3.7), (3.9), (3.10) in the overcompressive regime with $\theta = 1.3$ and $\tau = -0.5$) in the neighboring four cells at each side of the interface. This results in a hybrid "mixed-order" scheme, which still achieves higher resolution compared with the second-order LD PCCU scheme.

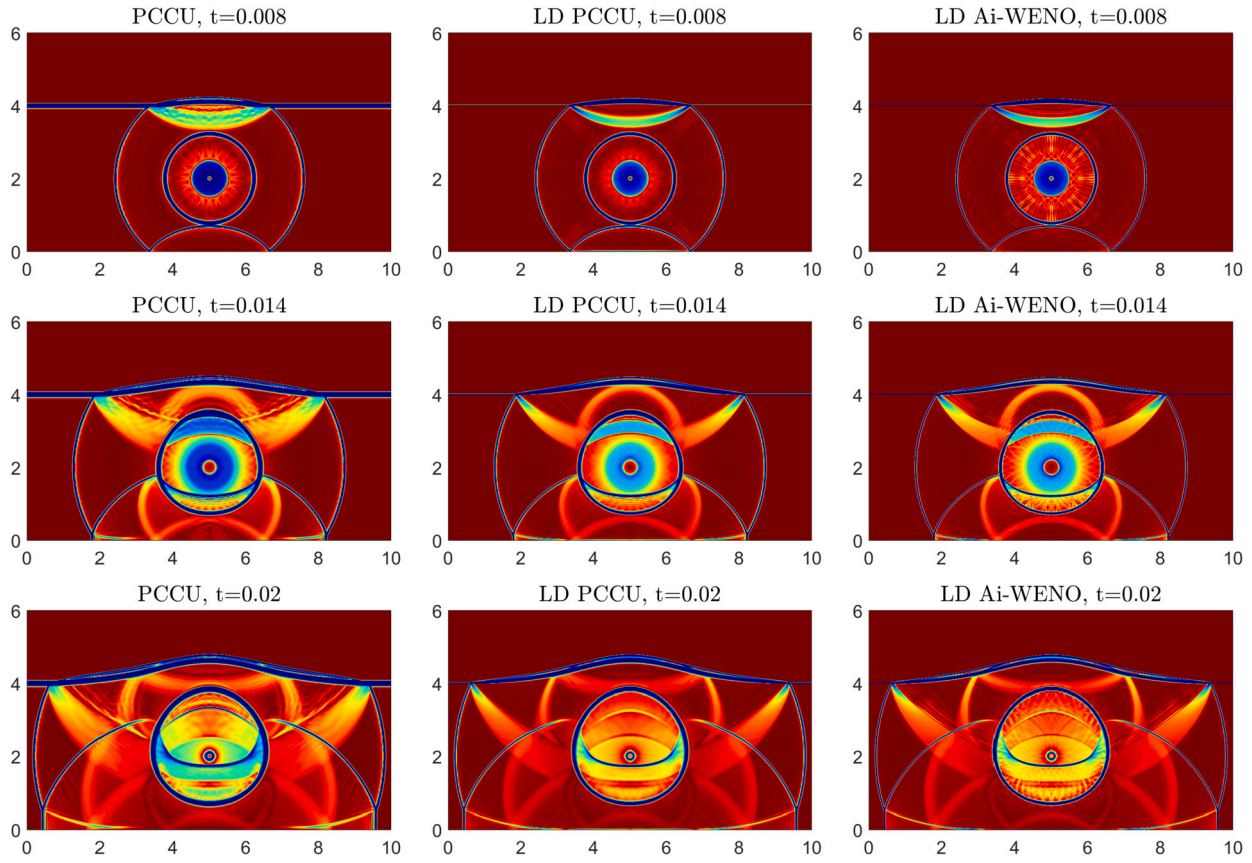

Fig. 4.16. Example 7: Solutions computed by the PCCU (left column), LD PCCU (middle column), and LD Ai-WENO (right column) schemes at times $t = 0.008$, 0.014, and 0.02.

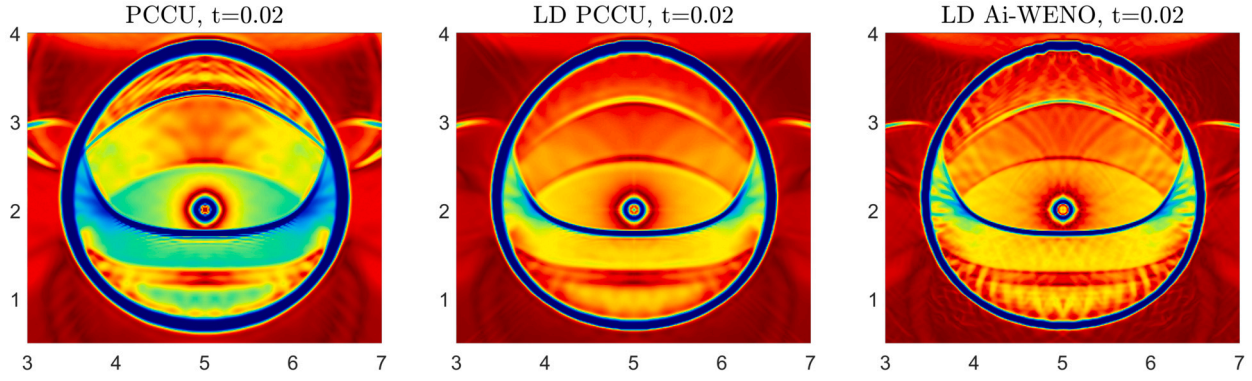

Fig. 4.17. Example 7: Solutions computed by the PCCU (left), LD PCCU (middle), and LD Ai-WENO (right) schemes at time $t = 0.02$; zoom at the bubble area.

5. Conclusion

In this paper, we have developed flux globalization based low-dissipation (LD) path-conservative central-upwind (PCCU) schemes for one- (1-D) and two-dimensional (2-D) compressible multifluids. The LD PCCU schemes are based on the flux globalization based PCCU schemes and employ the recently proposed LDCU fluxes to reduce the numerical dissipation present in the original PCCU schemes. In order to further enhance the resolution of material interfaces, we track their locations and use the overcompressive SBM limiter in their neighborhoods, while in the rest of the computational domain, a dissipative generalized minmod limiter is utilized. The new second-order finite-volume method is then extended to the fifth order of accuracy via the finite-difference A-WENO framework. We have applied the developed schemes to a number of 1-D and 2-D examples and the obtained numerical results clearly demonstrate that both of the LD PCCU and LD A-WENO schemes outperform the flux globalization based PCCU scheme that employs the original

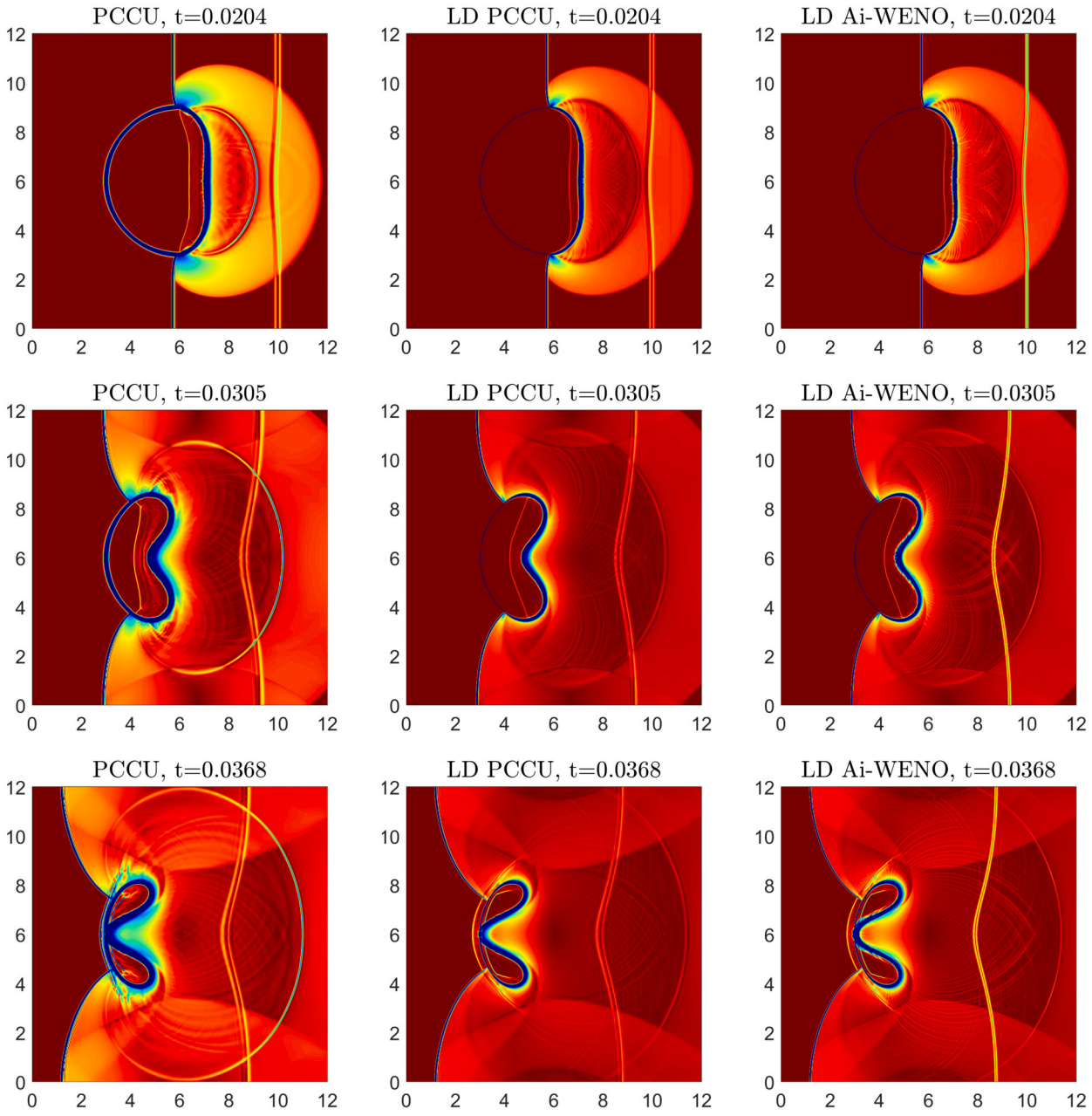

Fig. 4.18. Example 8: Shock-air bubble interaction computed by the PCCU (left column), LD PCCU (middle column), and LD Ai-WENO (right column) schemes at times $t = 0.0204$, 0.0305, and 0.0368.

central-upwind numerical flux from [28]. At the same time, these examples show that the fifth-order LD Ai-WENO scheme enhances the resolution achieved by the second-order LD PCCU scheme.

CRediT authorship contribution statement

Shaoshuai Chu: Writing – review & editing, Writing – original draft, Visualization, Validation, Software, Methodology, Investigation, Data curation, Conceptualization. **Alexander Kurganov:** Writing – review & editing, Writing – original draft, Validation, Supervision, Resources, Project administration, Methodology, Investigation, Funding acquisition, Formal analysis, Data curation, Conceptualization. **Ruixiao Xin:** Writing – review & editing, Writing – original draft, Visualization, Validation, Software, Methodology, Formal analysis, Data curation, Conceptualization.

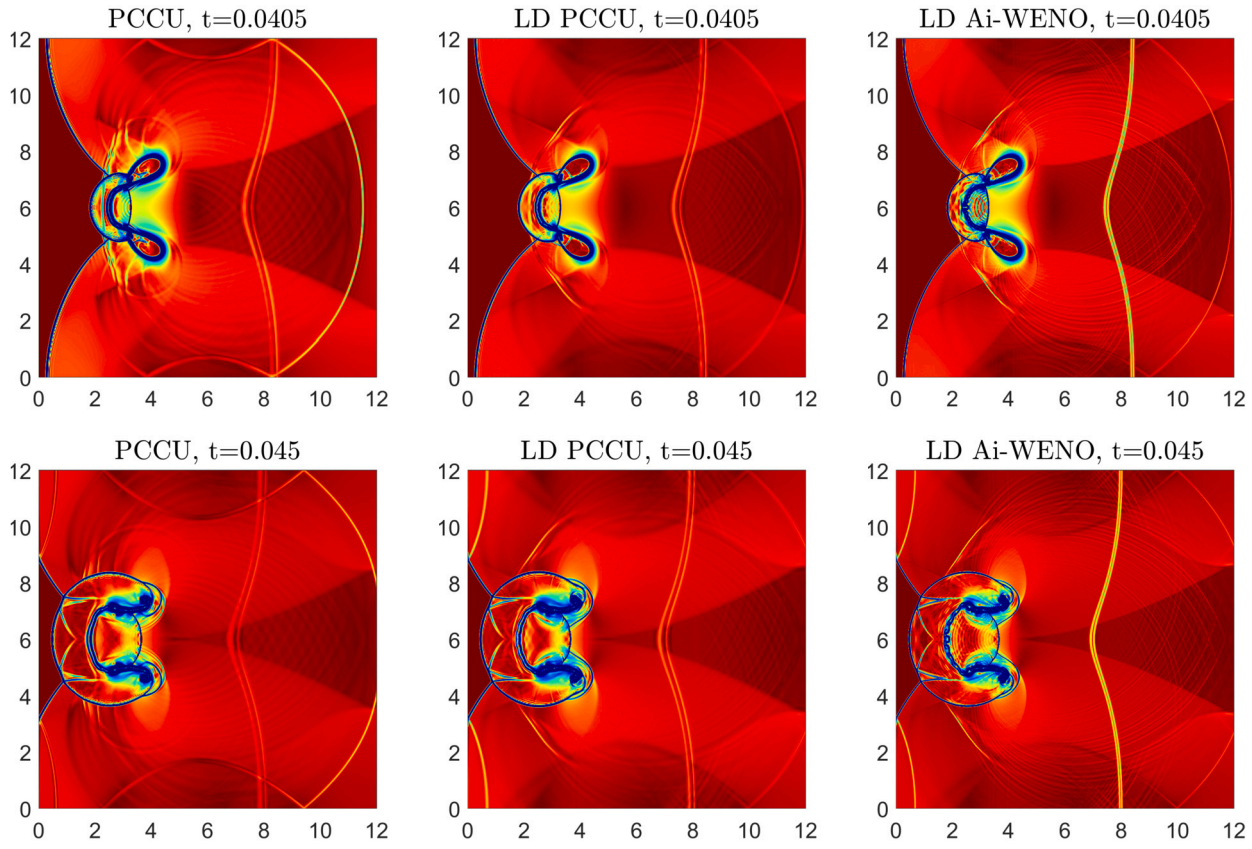

Fig. 4.19. Example 8: Same as in Fig. 4.18, but at larger times $t = 0.0405$ and 0.045.

Declaration of competing interest

The authors declare that they have no known competing financial interests or personal relationships that could have appeared to influence the work reported in this paper.

Data availability

Data will be made available on request.

Acknowledgement

The work of S. Chu was supported in part by the DFG (German Research Foundation) through HE5386/19-3, 27-1. The work of A. Kurganov was supported in part by NSFC grant 12171226 and by the fund of the Guangdong Provincial Key Laboratory Of Computational Science And Material Design (No. 2019B030301001).

Appendix A. 1-D fifth-order ai-WENO-Z interpolation

In this appendix, we briefly describe the fifth-order Ai-WENO-Z interpolation recently introduced in [17,34,50].

Assume that the point values $W_{j+\ell}$ of a certain quantity W at the uniform grid points $x = x_{j+\ell}$, $\ell = -2, \dots, 3$ are available. We now show how to obtain an interpolated left-sided value of W at $x = x_{j+\frac{1}{2}}$, denoted by $W^-_{j+\frac{1}{2}}$. The right-sided value $W^+_{j+\frac{1}{2}}$ can then be obtained in the mirror-symmetric way.

The value $W^-_{j+\frac{1}{2}}$ is calculated using a weighted average of the three parabolic interpolants $\mathcal{P}_0(x)$, $\mathcal{P}_1(x)$, and $\mathcal{P}_2(x)$ obtained using the stencils $[x_{j-2}, x_{j-1}, x_j]$, $[x_{j-1}, x_j, x_{j+1}]$, and $[x_j, x_{j+1}, x_{j+2}]$, respectively:

$$W^-_{j+\frac{1}{2}} = \sum_{k=0}^{2} \omega_k \mathcal{P}_k\left(x_{j+\frac{1}{2}}\right),$$

where

$$\mathcal{P}_0(x_{j+\frac{1}{2}}) = \frac{3}{8}W_{j-2} - \frac{5}{4}W_{j-1} + \frac{15}{8}W_j, \quad \mathcal{P}_1(x_{j+\frac{1}{2}}) = -\frac{1}{8}W_{j-1} + \frac{3}{4}W_j + \frac{3}{8}W_{j+1},$$
$$\mathcal{P}_2(x_{j+\frac{1}{2}}) = \frac{3}{8}W_j + \frac{3}{4}W_{j+1} - \frac{1}{8}W_{j+2},$$

and the Ai-weights ω_k are computed by

$$\omega_k = \frac{\alpha_k}{\alpha_0+\alpha_1+\alpha_2}, \quad \alpha_k = d_k\left[1+\left(\frac{\tau_5}{\beta_k+\varepsilon\mu_j^2}\right)^r\right], \quad k=0,1,2, \tag{A.1}$$

with $d_0=\frac{1}{16}$, $d_1=\frac{5}{8}$, and $d_2=\frac{5}{16}$. The smoothness indicators β_k for the corresponding parabolic interpolants $\mathcal{P}_k(x)$ are given by

$$\beta_0 = \frac{13}{12}\big(W_{j-2}-2W_{j-1}+W_j\big)^2 + \frac{1}{4}\big(W_{j-2}-4W_{j-1}+3W_j\big)^2,$$
$$\beta_1 = \frac{13}{12}\big(W_{j-1}-2W_j+W_{j+1}\big)^2 + \frac{1}{4}\big(W_{j-1}-W_{j+1}\big)^2,$$
$$\beta_2 = \frac{13}{12}\big(W_j-2W_{j+1}+W_{j+2}\big)^2 + \frac{1}{4}\big(3W_j-4W_{j+1}+W_{j+2}\big)^2.$$

Finally, in formula (A.1), $\tau_5=|\beta_2-\beta_0|$, $\mu_j=\frac{1}{5}\sum_{\ell=j-2}^{j+2}|W_\ell-\widehat{W}_j|+10^{-40}$ with $\widehat{W}_j:=\frac{1}{5}\sum_{\ell=j-2}^{j+2}W_\ell$, and in all of the numerical examples, we have chosen $r=2$ and $\varepsilon=10^{-12}$.

A.1. 1-D local characteristic decomposition

In §2.3, the Ai-WENO-Z interpolant is applied to the local characteristic variables, which are obtained using the LCD. To this end, we first rewrite the studied γ-based multifluid system in terms of the primitive variables $\boldsymbol{V}=(\rho,u,p,\Gamma,\Pi)^\top$:

$$\boldsymbol{V}_t+\mathcal{A}\boldsymbol{V}_x=\boldsymbol{0}, \quad \mathcal{A}:=\begin{pmatrix} u & \rho & 0 & 0 & 0\\ 0 & u & \frac{1}{\rho} & 0 & 0\\ 0 & \gamma(p+\pi_\infty) & u & 0 & 0\\ 0 & 0 & 0 & u & 0\\ 0 & 0 & 0 & 0 & u\end{pmatrix},$$

and introduce the locally averaged matrices

$$\widehat{\mathcal{A}}_{j+\frac{1}{2}}:=\begin{pmatrix} \hat{u} & \hat{\rho} & 0 & 0 & 0\\ 0 & \hat{u} & \frac{1}{\hat{\rho}} & 0 & 0\\ 0 & \hat{\gamma}(\hat{p}+\hat{\pi}_\infty) & \hat{u} & 0 & 0\\ 0 & 0 & 0 & \hat{u} & 0\\ 0 & 0 & 0 & 0 & \hat{u}\end{pmatrix}, \tag{A.2}$$

where $\widehat{(\cdot)}$ stands for the following averages (see [26]):

$$\hat{\rho}=\sqrt{\rho_j\rho_{j+1}}, \quad \hat{u}=\frac{\sqrt{\rho_j}u_j+\sqrt{\rho_{j+1}}u_{j+1}}{\sqrt{\rho_j}+\sqrt{\rho_{j+1}}}, \quad \hat{p}=\frac{\sqrt{\rho_j}p_j+\sqrt{\rho_{j+1}}p_{j+1}}{\sqrt{\rho_j}+\sqrt{\rho_{j+1}}},$$
$$\hat{\gamma}=\frac{\sqrt{\rho_j}\gamma_j+\sqrt{\rho_{j+1}}\gamma_{j+1}}{\sqrt{\rho_j}+\sqrt{\rho_{j+1}}}, \quad \hat{\pi}_\infty=\frac{\sqrt{\rho_j}(\pi_\infty)_j+\sqrt{\rho_{j+1}}(\pi_\infty)_{j+1}}{\sqrt{\rho_j}+\sqrt{\rho_{j+1}}},$$

where $\gamma_j=1+1/\Gamma_j$ and $(\pi_\infty)_j=\Pi_j/(1+\Gamma_j)$.

We then compute the matrix $R_{j+\frac{1}{2}}$ composed of the right eigenvectors of $\widehat{\mathcal{A}}_{j+\frac{1}{2}}$ and obtain

$$R_{j+\frac{1}{2}}=\begin{pmatrix} \frac{1}{\hat{c}^2} & 0 & 0 & 1 & \frac{1}{\hat{c}^2}\\ -\frac{1}{\hat{\rho}\hat{c}} & 0 & 0 & 0 & \frac{1}{\hat{\rho}\hat{c}}\\ 1 & 0 & 0 & 0 & 1\\ 0 & 0 & 1 & 0 & 0\\ 0 & 1 & 0 & 0 & 0\end{pmatrix} \quad \text{and} \quad R^{-1}_{j+\frac{1}{2}}=\begin{pmatrix} 0 & -\frac{\hat{\rho}\hat{c}}{2} & \frac{1}{2} & 0 & 0\\ 0 & 0 & 0 & 0 & 1\\ 0 & 0 & 0 & 1 & 0\\ 1 & 0 & -\frac{1}{\hat{c}^2} & 0 & 0\\ 0 & \frac{\hat{\rho}\hat{c}}{2} & \frac{1}{2} & 0 & 0\end{pmatrix}, \tag{A.3}$$

where $\hat{c}=\sqrt{\gamma(\hat{p}+\hat{\pi}_\infty)/\hat{\rho}}$. Notice that all of the $\widehat{(\cdot)}$ quantities in (A.2)–(A.3) have to have a subscript index, that is, $\widehat{(\cdot)}=\widehat{(\cdot)}_{j+\frac{1}{2}}$, but we have omitted it for the sake of brevity for all of the quantities except for $\widehat{\mathcal{A}}_{j+\frac{1}{2}}$.

Finally, we introduce the local characteristic variables in the neighborhood of $x = x_{j+\frac{1}{2}}$:

$$\boldsymbol{W}_{j+\ell} = R^{-1}_{j+\frac{1}{2}} \boldsymbol{V}_{j+\ell}, \quad \ell = -2, \dots, 3,$$

and apply the Ai-WENO-Z interpolation to every component of $\boldsymbol{W}$ to obtain $\boldsymbol{W}^{\pm}_{j+\frac{1}{2}}$, and then we end up with

$$\boldsymbol{V}^{\pm}_{j+\frac{1}{2}} = R_{j+\frac{1}{2}} \boldsymbol{W}^{\pm}_{j+\frac{1}{2}}.$$

Appendix B. 2-D local characteristic decomposition

In this appendix, we extend the 1-D LCD described in Appendix A.1 to the system (3.12), which can be rewritten in terms of the primitive variables $\boldsymbol{V} = (\rho, u, v, p, \Gamma, \Pi)^\top$ as

$$\boldsymbol{V}_t + \mathcal{A}\boldsymbol{V}_x = \boldsymbol{0}, \quad \mathcal{A} := \begin{pmatrix} u & \rho & 0 & 0 & 0 & 0 \\ 0 & u & 0 & \frac{1}{\rho} & 0 & 0 \\ 0 & 0 & u & 0 & 0 & 0 \\ 0 & \gamma(p+\pi_\infty) & 0 & u & 0 & 0 \\ 0 & 0 & 0 & 0 & u & 0 \\ 0 & 0 & 0 & 0 & 0 & u \end{pmatrix},$$

and introduce the locally averaged matrices

$$\widehat{\mathcal{A}}_{j+\frac{1}{2},k} = \begin{pmatrix} \hat{u} & \hat{\rho} & 0 & 0 & 0 & 0 \\ 0 & \hat{u} & 0 & \frac{1}{\hat{\rho}} & 0 & 0 \\ 0 & 0 & \hat{u} & 0 & 0 & 0 \\ 0 & \hat{\gamma}(\hat{p}+\hat{\pi}_\infty) & 0 & \hat{u} & 0 & 0 \\ 0 & 0 & 0 & 0 & \hat{u} & 0 \\ 0 & 0 & 0 & 0 & 0 & \hat{u} \end{pmatrix},$$

where $\widehat{(\cdot)}$ stands for the following averages:

$$\hat{\rho} = \sqrt{\rho_{j,k}\,\rho_{j+1,k}}, \quad \hat{u} = \frac{\sqrt{\rho_{j,k}}u_{j,k} + \sqrt{\rho_{j+1,k}}u_{j+1,k}}{\sqrt{\rho_{j,k}} + \sqrt{\rho_{j+1,k}}}, \quad \hat{p} = \frac{\sqrt{\rho_{j,k}}p_{j,k} + \sqrt{\rho_{j+1,k}}p_{j+1,k}}{\sqrt{\rho_{j,k}} + \sqrt{\rho_{j+1,k}}},$$

$$\hat{\gamma} = \frac{\sqrt{\rho_{j,k}}\gamma_{j,k} + \sqrt{\rho_{j+1,k}}\gamma_{j+1,k}}{\sqrt{\rho_{j,k}} + \sqrt{\rho_{j+1,k}}}, \quad \hat{\pi}_\infty = \frac{\sqrt{\rho_{j,k}}(\pi_\infty)_{j,k} + \sqrt{\rho_{j+1,k}}(\pi_\infty)_{j+1,k}}{\sqrt{\rho_{j,k}} + \sqrt{\rho_{j+1,k}}},$$

with $\gamma_{j,k} = 1 + 1/\Gamma_{j,k}$ and $(\pi_\infty)_{j,k} = \Pi_{j,k}/(1+\Gamma_{j,k})$.

We then compute the matrices $R_{j+\frac{1}{2},k}$ and $R^{-1}_{j+\frac{1}{2},k}$ such that the matrix $R^{-1}_{j+\frac{1}{2},k}\widehat{\mathcal{A}}_{j+\frac{1}{2},k}R_{j+\frac{1}{2},k}$ is diagonal and obtain

$$R_{j+\frac{1}{2},k} = \begin{pmatrix} \frac{1}{\hat{c}^2} & 0 & 0 & 0 & 1 & \frac{1}{\hat{c}^2} \\ -\frac{1}{\hat{\rho}\hat{c}} & 0 & 0 & 0 & 0 & \frac{1}{\hat{\rho}\hat{c}} \\ 0 & 0 & 0 & 1 & 0 & 0 \\ 1 & 0 & 0 & 0 & 0 & 1 \\ 0 & 0 & 1 & 0 & 0 & 0 \\ 0 & 1 & 0 & 0 & 0 & 0 \end{pmatrix} \quad \text{and} \quad R^{-1}_{j+\frac{1}{2},k} = \begin{pmatrix} 0 & -\frac{\hat{\rho}\hat{c}}{2} & 0 & \frac{1}{2} & 0 & 0 \\ 0 & 0 & 0 & 0 & 0 & 1 \\ 0 & 0 & 0 & 0 & 1 & 0 \\ 0 & 0 & 1 & 0 & 0 & 0 \\ 1 & 0 & 0 & -\frac{1}{\hat{c}^2} & 0 & 0 \\ 0 & \frac{\hat{\rho}\hat{c}}{2} & 0 & \frac{1}{2} & 0 & 0 \end{pmatrix}.$$

Appendix A.1, we have omitted the $(j+\frac{1}{2}, k)$ indices for all of the $\widehat{(\cdot)}$ quantities except for $\widehat{\mathcal{A}}_{j+\frac{1}{2},k}$.

Finally, given the matrices $R^{-1}_{j+\frac{1}{2},k}$ and $R_{j+\frac{1}{2},k}$, we introduce the local characteristic variablesnin the neighborhood of $(x, y) = (x_{j+\frac{1}{2}}, y_k)$:

$$\boldsymbol{W}_{j+\ell,k} = R^{-1}_{j+\frac{1}{2},k}\boldsymbol{V}_{j+\ell,k}, \quad \ell = -2, \dots, 3,$$

apply the Ai-WENO-Z interpolation to every component of $\boldsymbol{W}$ to obtain $\boldsymbol{W}^{\pm}_{j+\frac{1}{2},k}$, and end up with

$$\boldsymbol{V}^{\pm}_{j+\frac{1}{2},k} = R_{j+\frac{1}{2},k}\boldsymbol{W}^{\pm}_{j+\frac{1}{2},k}.$$

Notice that the point values $\boldsymbol{V}^{\pm}_{j,k+\frac{1}{2}}$ are obtained in a similar manner and we omit the details for the sake of brevity.

References

[1] R. Abgrall, How to prevent pressure oscillations in multicompoent flow calculations: a quasi conservative approach, J. Comput. Phys. 125 (1996) 150–160.
[2] R. Abgrall, S. Karni, Computations of compressible multifluids, J. Comput. Phys. 169 (2001) 594–623.
[3] R. Abgrall, S. Karni, Ghost-fluids for the poor: a single fluid algorithm for multifluids, in: Hyperbolic Problems: Theory, Numerics, Applications, Birkhäuser, Basel, 2001.
[4] Y. Cao, A. Kurganov, Y. Liu, R. Xin, Flux globalization based well-balanced path-conservative central-upwind schemes for shallow water models, J. Sci. Comput. 92 (2022).
[5] Y. Cao, A. Kurganov, Y. Liu, V. Zeitlin, Flux globalization based well-balanced path-conservative central-upwind scheme for two-layer thermal rotating shallow water equations, J. Comput. Phys. 474 (2023) 111790, 29 pp.
[6] M.J. Castro Díaz, A. Kurganov, T. Morales de Luna, Path-conservative central-upwind schemes for nonconservative hyperbolic systems, ESAIM: Math. Model. Numer. Anal. 53 (2019) 959–985.
[7] Y. Chen, A. Kurganov, M. Na, A flux globalization based well-balanced path-conservative central-upwind scheme for the shallow water flows in channels, ESAIM: Math. Model. Numer. Anal. 57 (2023) 1087–1110.
[8] J. Cheng, F. Zhang, T.G. Liu, A discontinuous Galerkin method for the simulation of compressible gas-gas and gas-water two-medium flows, J. Comput. Phys. 403 (2020) 109059, 29 pp.
[9] A. Chertock, S. Chu, A. Kurganov, Hybrid multifluid algorithms based on the path-conservative central-upwind scheme, J. Sci. Comput. 89 (2021) 48, 24 pp.
[10] A. Chertock, S. Karni, A. Kurganov, Interface tracking method for compressible multifluids, M2AN Math. Model. Numer. Anal. 42 (2008) 991–1019.
[11] S. Chu, A. Kurganov, S. Mohammadian, Z. Zheng, Fifth-order A-WENO path-conservative central-upwind scheme for behavioral non-equilibrium traffic models, Commun. Comput. Phys. 33 (2023) 692–732.
[12] S. Chu, A. Kurganov, M. Na, Fifth-order A-WENO schemes based on the path-conservative central-upwind method, J. Comput. Phys. 469 (2022) 111508, 22 pp.
[13] S. Chu, A. Kurganov, R. Xin, To appear in the A fifth-order A-WENO scheme based on the low-dissipation central-upwind fluxes, in: Proceedings of the XVIII International Conference on Hyperbolic Problems: Theory, Numerics, Applications,.
[14] S. Chu, A. Kurganov, R. Xin, New low-dissipation central-upwind schemes. Part II, Submitted, preprint is available at, https://sites.google.com/view/alexander-kurganov/publications.
[15] S. Chu, A. Kurganov, R. Xin, New more efficient A-WENO schemes, Submitted, preprint is available at, https://sites.google.com/view/alexander-kurganov/publications.
[16] W.S. Don, D.-M. Li, Z. Gao, B.-S. Wang, A characteristic-wise alternative WENO-Z finite difference scheme for solving the compressible multicomponent non-reactive flows in the overestimated quasi-conservative form, J. Sci. Comput. 82 (2020), Paper No. 27, 24 pp.
[17] W.S. Don, R. Li, B.-S. Wang, Y.H. Wang, A novel and robust scale-invariant WENO scheme for hyperbolic conservation laws, J. Comput. Phys. 448 (2022), Paper No. 110724, 23 pp.
[18] R.P. Fedkiw, T. Aslam, B. Merriman, S. Osher, A non-oscillatory Eulerian approach to interfaces in multimaterial flows (the ghost fluid method), J. Comput. Phys. 152 (1999) 457–492.
[19] S. Gottlieb, D. Ketcheson, C.-W. Shu, Strong Stability Preserving Runge-Kutta and Multistep Time Discretizations, World Scientific Publishing Co. Pte. Ltd., Hackensack, NJ, 2011.
[20] S. Gottlieb, C.-W. Shu, E. Tadmor, Strong stability-preserving high-order time discretization methods, SIAM Rev. 43 (2001) 89–112.
[21] J.-F. Haas, B. Sturtevant, Interaction of weak shock waves with cylindrical and spherical gas inhomogeneities, J. Fluid Mech. 181 (1987) 41–76.
[22] Z.W. He, L. Li, Y.S. Zhang, B.L. Tian, Consistent implementation of characteristic flux-split based finite difference method for compressible multi-material gas flows, Comput. Fluids 168 (2018) 190–200.
[23] J.S. Hesthaven, Numerical Methods for Conservation Laws: From Analysis to Algorithms, Comput. Sci. Eng., vol. 18, SIAM, Philadelphia, 2018.
[24] Y. Jiang, C.-W. Shu, M. Zhang, An alternative formulation of finite difference weighted ENO schemes with Lax-Wendroff time discretization for conservation laws, SIAM J. Sci. Comput. 35 (2013) A1137–A1160.
[25] E. Johnsen, T. Colonius, Implementation of WENO schemes in compressible multicomponent flow problems, J. Comput. Phys. 219 (2006) 715–732.
[26] S. Karni, Multicomponent flow calculations by a consistent primitive algorithm, J. Comput. Phys. 112 (1993) 31–43.
[27] S. Karni, Hybrid multifluid algorithms, SIAM J. Sci. Comput. 17 (1996) 1019–1039.
[28] A. Kurganov, C.-T. Lin, On the reduction of numerical dissipation in central-upwind schemes, Commun. Comput. Phys. 2 (2007) 141–163.
[29] A. Kurganov, Y. Liu, R. Xin, Well-balanced path-conservative central-upwind schemes based on flux globalization, J. Comput. Phys. 474 (2023) 111773, 32 pp.
[30] A. Kurganov, S. Noelle, G. Petrova, Semi-discrete central-upwind schemes for hyperbolic conservation laws and Hamilton-Jacobi equations, SIAM J. Sci. Comput. 23 (2001) 707–740.
[31] A. Kurganov, E. Tadmor, New high-resolution central schemes for nonlinear conservation laws and convection-diffusion equations, J. Comput. Phys. 160 (2000) 241–282.
[32] A. Kurganov, R. Xin, New low-dissipation central-upwind schemes, J. Sci. Comput. 96 (2023) 56, 33 pp.
[33] R.J. LeVeque, Finite Volume Methods for Hyperbolic Problems, Cambridge Texts in Applied Mathematics, Cambridge University Press, Cambridge, 2002.
[34] P. Li, T.T. Li, W.S. Don, B.-S. Wang, Scale-invariant multi-resolution alternative WENO scheme for the Euler equations, J. Sci. Comput. 94 (2023) 15, 32 pp.
[35] K.-A. Lie, S. Noelle, On the artificial compression method for second-order nonoscillatory central difference schemes for systems of conservation laws, SIAM J. Sci. Comput. 24 (2003) 1157–1174.
[36] J.-Y. Lin, Y. Shen, H. Ding, N.-S. Liu, X.-Y. Lu, Simulation of compressible two-phase flows with topologychange of fluid–fluid interface by a robust cut-cell method, J. Comput. Phys. 328 (2017) 140–159.
[37] H. Liu, A numerical study of the performance of alternative weighted ENO methods based on various numerical fluxes for conservation law, Appl. Math. Comput. 296 (2017) 182–197.
[38] H. Liu, J. Qiu, Finite difference Hermite WENO schemes for conservation laws, II: An alternative approach, J. Sci. Comput. 66 (2016) 598–624.
[39] W. Mulder, S. Osher, J.A. Sethian, Computing interface motion in compressible gas dynamics, J. Comput. Phys. 100 (1992) 209–228.
[40] H. Nessyahu, E. Tadmor, Nonoscillatory central differencing for hyperbolic conservation laws, J. Comput. Phys. 87 (1990) 408–463.
[41] T. Nonomura, K. Fujii, Characteristic finite-difference WENO scheme for multicomponent compressible fluid analysis: overestimated quasi-conservative formulation maintaining equilibriums of velocity, pressure, and temperature, J. Comput. Phys. 340 (2017) 358–388.
[42] T. Nonomura, S. Morizawa, H. Terashima, S. Obayashi, K. Fujii, Numerical (error) issues on compressible multicomponent flows using a high-order differencing scheme: weighted compact nonlinear scheme, J. Comput. Phys. 231 (2012) 3181–3210.
[43] J. Quirk, S. Karni, On the dynamics of a shock-bubble interaction, J. Fluid Mech. 318 (1996) 129–163.
[44] R. Saurel, R. Abgrall, A multiphase Godunov method for compressible multifluid and multiphase flows, J. Comput. Phys. 150 (1999) 425–467.
[45] R. Saurel, R. Abgrall, A simple method for compressible multifluid flows, SIAM J. Sci. Comput. 21 (1999) 1115–1145.
[46] K.-M. Shyue, An efficient shock-capturing algorithm for compressible multicomponent problems, J. Comput. Phys. 142 (1998) 208–242.

[47] P.K. Sweby, High resolution schemes using flux limiters for hyperbolic conservation laws, SIAM J. Numer. Anal. 21 (1984) 995–1011.
[48] E.F. Toro, Riemann Solvers and Numerical Methods for Fluid Dynamics: A Practical Introduction, third ed., Springer-Verlag, Berlin, Heidelberg, 2009.
[49] B.-S. Wang, W.S. Don, Fifth-order bound-, positivity-, and equilibrium-preserving affine-invariant AWENO scheme for two-medium γ-based model of stiffened gas, Submitted, preprint is available at, https://doi.org/10.13140/RG.2.2.18907.85288.
[50] B.-S. Wang, W.S. Don, Affine-invariant WENO weights and operator, Appl. Numer. Math. 181 (2022) 630–646.
[51] B.-S. Wang, W.S. Don, N.K. Garg, A. Kurganov, Fifth-order A-WENO finite-difference schemes based on a new adaptive diffusion central numerical flux, SIAM J. Sci. Comput. 42 (2020) A3932–A3956.
[52] B.-S. Wang, W.S. Don, A. Kurganov, Y. Liu, Fifth-order A-WENO schemes based on the adaptive diffusion central-upwind Rankine-Hugoniot fluxes, Commun. Appl. Math. Comput. 5 (2023) 295–314.
[53] B.-S. Wang, P. Li, Z. Gao, W.S. Don, An improved fifth order alternative WENO-Z finite difference scheme for hyperbolic conservation laws, J. Comput. Phys. 374 (2018) 469–477.
[54] C.W. Wang, T.G. Liu, C.-W. Shu, A real ghost fluid method for the simulation of multimedium compressible flow, SIAM J. Sci. Comput. 28 (2006) 278–302.
[55] C.W. Wang, C.-W. Shu, An interface treating technique for compressible multi-medium flow with Runge-Kutta discontinuous Galerkin method, J. Comput. Phys. 229 (2010) 8823–8843.
[56] L. Xu, T.G. Liu, Explicit interface treatments for compressible gas-liquid simulations, Comput. Fluids 153 (2017) 34–48.